Aalborg Universitet

AALBORG UNIVERSITY
DENMARK

Experimental and Computational Study of Mixing and Fast Chemical Reactions in Turbulent Liquid Flows

Hjertager, Lene Kristin

Publication date:
2004

Document Version
Accepted author manuscript, peer reviewed version

Link to publication from Aalborg University

Citation for published version (APA):
Hjertager, L. K. (2004). *Experimental and Computational Study of Mixing and Fast Chemical Reactions in Turbulent Liquid Flows*. Esbjerg Institute of Technology, Aalborg University.

General rights
Copyright and moral rights for the publications made accessible in the public portal are retained by the authors and/or other copyright owners and it is a condition of accessing publications that users recognise and abide by the legal requirements associated with these rights.

- Users may download and print one copy of any publication from the public portal for the purpose of private study or research.
- You may not further distribute the material or use it for any profit-making activity or commercial gain
- You may freely distribute the URL identifying the publication in the public portal -

Take down policy
If you believe that this document breaches copyright please contact us at vbn@aub.aau.dk providing details, and we will remove access to the work immediately and investigate your claim.

Downloaded from vbn.aau.dk on: April 23, 2024

Experimental and Computational Study of Mixing and Fast Chemical Reactions in Turbulent Liquid Flows

Ph.D. thesis

Submitted by

Lene Kristin Hjertager Osenbroch

to The Faculty of Engineering and Science, Aalborg University
for the degree of Doctor of Philosophy.

Group for Chemical Fluid Flow Processes
Esbjerg Institute of Engineering
Aalborg University Esbjerg
Niels Bohrs Vej 8
DK-6700 Esbjerg, Denmark

September 2004

Lene Kristin Hjertager Osenbroch
Experimental and Computational Study of Mixing and Fast Chemical Reactions in Turbulent Liquid Flows
Ph.D. thesis Aalborg University Esbjerg, 2004.

©L.K.H. Osenbroch, Esbjerg 2004
All rights reserved. No part of this work may be reproduced by print, photocopy or any other means without the permission in writing from the publisher.

ISBN 87-990102-0-8

Published by Aalborg University Esbjerg, Niels Bohrs Vej 8,
DK-6700 Esbjerg, Denmark.
http://www.aue.auc.dk/
Printed by Elbro tryk, Postbox 3072,
DK-6710 Esbjerg V, Denmark.
Cover design by Martin Helsing.
Typeset with Word

Abstract

Mixing and fast chemical reactions in turbulent liquid flows are studied experimentally and computationally. Experiments are carried out for both passive and reactive mixing in order to obtain local velocity and concentrations. The experimental findings are used to test the performance of numerical models for turbulence, mixing and chemical reactions.

The experiments are carried out in a mixing channel with two inlets separated by a block. For the passive mixing three different flow cases are studied. A combined PIV/PLIF technique is used to obtain instantaneous velocity and concentration fields. For the first flow case with a velocity ratio of 1:1, large scale fluctuations are observed and a wake is formed. For the second case with a velocity ratio of 0.5:1, the fluctuations are smaller and a weak backflow is observed along the left channel wall. For the third flow case with a velocity ratio of 0.25:1, the backflow observed along the left channel wall is much stronger and the flow seems to act almost as a backward facing step. Clearly, changing the velocity ratio makes a transition in the flow from a wake flow towards a backward facing step. For all three flow cases a recirculation zone is formed behind the block dividing the two inlet streams. The mixing in the recirculation zone is most effective in the first case and becomes less effective as the velocity ratio decreases.

For the reactive mixing two different flow cases are studied. A reactive-PLIF technique is used to measure the product concentration from an acid-base reaction. The amount of product formed is found to be strongly dependent on how well the two inlet streams are mixed.

Two dimensional numerical predictions of a tubular reactor are evaluated against predictions and experiments found from literature. The simple reaction model, the Eddy Dissipation Concept (EDC), developed for combustion reactions is found to be non suitable for liquid phase reactions. Modifying the model with a multiple-timescale turbulent mixer model (EDC-MTS) gives a substantial improvement.

Two dimensional numerical predictions of the mixing channel show that none of the k-ε turbulence models tested is suitable for the flow cases studied here. The turbulent Schmidt number is reduced to obtain a good agreement between measured and predicted mean and fluctuating concentrations. Two mixing models are tested, namely the multi-peak presumed PDF model and the multiple-timescale turbulent mixer model. The multi-peak presumed PDF model using a large scale dominated micro-mixing rate is found to give best agreement between measured and predicted concentration fluctuations. The predicted PDF's from the multi-peak presumed PDF model gives good overall agreement with experimental data.

The multi-peak presumed PDF model and the EDC-model are also tested against reactive mixing experiments. The multi-peak presumed PDF model is found to give the best agreement between measured and predicted product concentration. The modified version of the EDC model, the EDC-MTS model, gives results which are close to the multi-peak presumed PDF model.

Synopsis

Opblanding og kemiske reaktioner i turbulent væskestrømning er studeret eksperimentelt og numerisk. Det er udført eksperimenter for både passiv og reaktiv opblanding for at finde lokale hastigheder og koncentrationer. De eksperimentelle data bruges til at teste numeriske modeller for turbulens, opblanding og kemiske reaktioner.

Eksperimenterne er udført i en opblandingskanal med to indløb, der er adskilt med en blok. I de passive opblandingsforsøg er tre forskellige strømningstilstande studeret. En kombineret PIV/PLIF-teknik er brugt for at finde øjeblikkelige hastigheder og koncentrationer. I den første case, med hastighedsforhold 1:1, er der observeret stor-skala fluktuationer og en ”wake” dannes. I den anden case, med hastighedsforhold 0.5:1, er fluktuationerne mindre og en svag tilbagestrømning er identificeret langs venstre side af kanalen. I den tredje case, med hastighedsforhold 0.25:1, er tilbagestrømningen langs venstre side af kanalen meget stærkere og strømningen opfører sig som et tilbagestrømmende trin. Ændring af hastighedsforholdet fører til en overgang fra en ”wake”-strømning til et tilbagestrømmende trin. I alle de tre strømningscases, der er studeret, dannes der en recirkulationszone bag blokken, der skiller de to indløbsstrømme. Opblandingen i recirkulationszonen er mest effektiv i den første case og bliver mindre effektiv ved aftagende hastighedsforhold.

For reaktiv opblanding er der studeret to strømningstilstande. En reaktiv-PLIF-teknik er brugt for at måle produkt koncentrationen fra en syre-base reaktion. Der er fundet, at mængden produkt der dannes afhænger af hvor godt de to strømme er opblandet.

Todimensionale numeriske beregninger af en tubular reaktor er evalueret mod beregninger og eksperimenter fundet i litteraturen. Der er fundet at den simple reaktionsmodel, the Eddy Dissipation Concept (EDC), udviklet for forbrændings reaktioner, ikke er god for reaktioner i væskefase. Den modificerede model, EDC-MTS, giver signifikante forbedringer.

Todimensionale numeriske beregninger af opblandingskanalen viser at ingen af k-ε turbulensmodellerne er passende for strømningstilstandene der er studeret her. Det turbulente Schmidt-tal er reduceret for at opnå god sammenhæng mellem målt og beregnet middel- og fluktuerende koncentration. To modeller for opblanding er testet: 'the multi-peak presumed PDF model' og 'the multiple-timescale turbulent mixer model'. Det er fundet at 'the multi-peak presumed PDF model' med en stor-skala model for 'micro-mixing' giver bedst sammenhæng mellem målte og beregnede koncentrationsfluktuationer. De beregnede PDF'er fra 'the multi-peak presumed PDF model' passer godt sammen med de eksperimentelle data.

'The multi-peak presumed PDF model' og EDC-modellen er også testet imod de reaktive opblandingseksperimenter. 'The multi-peak presumed PDF model' giver bedst sammenhæng mellem målte og beregnede produktkoncentrationer. Den modificerede model, EDC-MTS-model giver resultater, der ligger tæt på 'the multi-peak presumed PDF model'.

Acknowledgements

This work has been carried out at Esbjerg Department of Engineering, Aalborg University Esbjerg.

I would like to thank my supervisors, professor Tron Solberg and professor Bjørn H. Hjertager, my colleagues during the work on the Ph.D.; Claus Ibsen, Niels Deen, Peter Naamansen, Jørgen Osenbroch, Kim G. Hansen, Stefano Bove, Jesper Madsen and Rolf Hansen.

For technical assistance I would like to thank Jens Jørgen Jensen and Henry Enevoldsen.

I would like to acknowledge Lida and Oscar Nielsens Fond, Fabrikant Mads Clausens Fond, Esbjerg Seminarie Fond, Direktør Ib Henriksens Fond, Fabrikant P.A. Fiskers Fond and DONG's Jubilæumslegat for their financial support to build up a laser-based laboratory. I would also like to thank Otto Mønsteds Fond and Familien Hede Nielsens Fond for their financial support to my conference travel to Quebec City, Canada.

Finally, a great thanks to my husband, Jørgen, and my children, Synne and Endre.

Contents

Nomenclature

C	mean concentration [-]
$\widetilde{C}$	instantaneous concentration [-]
$C_{A,b}$	bulk concentration in feed channel A [-]
$C_{B,b}$	bulk concentration in feed channel B [-]
C_i	concentrations at the given axial position [-]
$\widetilde{C}_i^*$	normalised instantaneous concentration in image number i [-]
$<C>_A$	cross-sectional average of concentration at a given axial position [-]
C_p	local instantaneous product concentration [-]
$C_{p,max}$	maximum value at threshold conditions [-]
c	instantaneous concentration fluctuations [-]
c_{rms}	root mean square of the concentration fluctuations [-]
$<c_{rms}>_A$	cross-sectional average of the root mean square of the concentration fluctuations [-]
CoV	coefficient of variation [-]
D	channel diameter [m]
d	block diameter [m]
d	decay function [-]
E	engulfment parameter [1/s]
f	mixure fraction [-]
G	molecular diffusion rate [1/s]
$G_n(p)$	probability exchange rate [1/s]
I	local fluorescence intensity [-]
I_{back}	intensity of the background noise [-]
I_{max}	maximal intensity at the fluorescence threshold conditions [-]
I_i	intensity in image number i [-]

I_{ref}	intensity of reference image [-]
$J_{\phi j}$	turbulent scalar fluxes [m/s]
k	turbulent kinetic energy [m^2 s^2]
M	magnification of camera [-]
$M_\phi^n(p,s)$	scalar flux between environments [1/s]
m	total number of scalars [-]
N	number of data points or images in the sample [-]
N_e	total number of environments [-]
n	environment number [-]
P	mean pressure [N/m^2]
P_k	production of turbulent kinetic energy [kg/m s^3]
p_n	probability/volume fraction of environment n [-]
R	ratio of the timescale for decay of velocity fluctuations to the timescale of concentration fluctuations [-]
R_A	time averaged reaction rate [kg/m^3 s]
$r_n(p)$	probability flux [-]
S	mean strain rate [1/s]
Sc	Schmidt number [-]
Sc_T	turbulent Schmidt number for scalar variables [-]
$\vec{S}_D$	displacement vector [-]
S_{ij}	mean rate of strain tensor [1/s]
s	stoichiometric coefficient [-]
$<s_\phi>_n$	volume weighted scalar variable in environment n [-]
t	time [s]
Δt	exposure time delay [s]
U	mean transverse velocity [m/s]
U_i	mean velocity in i-direction [m/s]
U_j	mean velocity in j-direction [m/s]
u	instantaneous transverse velocity fluctuations [m/s]
u_i	fluctuating velocity in i-direction [m/s]
u_j	fluctuating velocity in j-direction [m/s]
u_{rms}	root mean square of the transverse velocity fluctuations [m/s]
u_t	predicted turbulent velocity [m/s]
$<uc>$	transverse scalar Reynolds flux [m/s]
$<uv>$	Reynolds shear stress [m^2/s^2]
V	mean axial velocity [m/s]
$V_{A,b}$	bulk velocity in feed channel A [m/s]
$V_{B,b}$	bulk velocity in feed channel B [m/s]

v	instantaneous axial velocity fluctuations [m/s]
$\vec{v}$	velocity vector [m/s]
v_{rms}	root mean square of the axial velocity fluctuations [m/s]
$<vc>$	axial scalar Reynolds flux [m/s]
x	transverse direction [m]
x_i	i – direction [m]
x_j	j – direction [m]
Y_i	mass fraction of species I [-]
$\hat{Y}_i$	instantaneous mass fraction of species i [-]
y	axial direction [m]
Δz	thickness of the light sheet [m]

Greek letters

β	conserved combined variable [-]
γ	rate of micromixing [1/s]
η	timescale ratio between the turbulence and mean flow [-]
ν_T	turbulent kinematic viscosity [m^2/s]
Γ_ϕ	turbulent transport coefficient [kg/m s]
ε	dissipation of turbulent kinetic energy [m^2/s^3]
ε_ϕ	dissipation of a scalar variable ϕ [-]
ε_μ	error estimate for the mean [-]
ε_σ	error estimate for the standard deviation [-]
μ_T	turbulent viscosity [kg/m s]
ξ	mixture fraction [-]
$\hat{\xi}$	instantaneous mixture fraction [-]
ρ	density [kg/m^3]
σ	standard deviation [-]
σ_C^2	concentration variance [-]
σ_i^2	concentration variance in sub-range i [-]
σ_k	turbulent Schmidt number for k [-]
σ_ε	turbulent Schmidt number for ε [-]
σ_S^2	concentration variance [-]
σ_ϕ	turbulent Prandtl/Schmidt number [-]
τ_D	dissipation rate timescale [s]

τ_{ij}	Reynolds stress [kg/m s^2]
τ_m	characteristic timescale for micromixing [s]
τ_P	production-range timescale [s]
Φ	correlation coefficient [-]
ϕ	scalar variable [-]
ϕ'	fluctuating scalar variable [-]
$<\phi'^2>$	variance of the scalar variable [-]
$<\phi>_n(x,t)$	the value of scalar ϕ corresponding to environment n [-]

Subscripts

A	feed channel A
B	feed channel B
b	bulk
back	background
D	dissipation
eff	effective
k	turbulent kinetic energy
m	micromixing
n	environment
P	production
ref	reference
rms	root mean square
T	turbulent
max	maximum
min	minimum

Abbreviations

CFD	Computational Fluid Dynamics
EDC	Eddy Dissipation Concept
LES	Large Eddy Simulation
MMR	Micro mixing rate
MTS	Multiple Timescale Turbulent Mixer
PDF	Probability density function
PIV	Particle Image Velocimetry
PLIF	Planar Laser Induced Fluorescence
SDT	Scalar Dissipation Timescale

Chapter 1

Introduction

Mixing and fast chemical reactions in turbulent liquid flows are the main topic of this thesis. Mixing can be described as the process at which a non-uniform system is made uniform. The degree of mixing, or the uniformity, can be analysed by evaluating how well the flow is macro- or micro-mixed. Macro-mixing means that there is no mixing on molecular scale, but fluid elements are well mixed on a large scale. Micro-mixing is complete mixing of species even on a molecular scale. Turbulent mixing is involved in many processes in the chemical process industry. It has the ability to mix and transport species, momentum and energy much faster than is done by molecular diffusion and is therefore employed in e.g. chemical reactors to make them perform better. A chemical reaction is a molecular process where only mixing on molecular level can affect the reaction directly, so-called micro-mixing. Micro-mixing affects fast and instantaneous chemical reactions, which may lead to changes in conversion and selectivity. Turbulent mixing is an important problem when estimating the turbulent diffusion of contaminants in the environment and when designing industrial combustors and reactors. Turbulent mixing is also important in processes in the pharmaceutical industry.

It is of great importance to have a detailed understanding of the turbulent mixing process when developing and validating numerical models to describe this type of processes. Only experimental verification of turbulent mixing will be able to give this insight. The mixing process can be described as turbulent transport of mass by turbulent velocity fluctuations. Experimental study of turbulent mixing thereby requires simultaneous measurement of the instantaneous velocity and concentration fields. Laser visualization combined with image processing

is a powerful tool to study structures and mechanisms of mixing and chemical reactions in reactors. Combining Particle Image Velocimetry (PIV) and Planar Laser Induced Fluorescence (PLIF) makes this type of measurement possible.

One way to study the mechanism in a turbulent reacting flow is to solve numerically the mass transport and the Navier-Stokes equations without any assumptions. This is referred to as Direct Numerical Simulation (DNS). DNS is difficult to perform for a turbulent reacting liquid flow with high Reynolds and Schmidt numbers. This is because the minimum scale of the concentration fluctuations, the Batchelor scale, is small compared to the Kolmogorov scale. Because of the huge number of numerical grid points required for DNS, time averaged transport equations are used for engineering purposes (Komori et al., 1993).

Turbulence can be modelled by the use of different models, e.g. the widely used k-ε model. Modelling of chemical reactions in turbulent flows can be performed with the use of different type of reaction models; the Eddy dissipation concept (EDC) is a simple model which is used in several commercial codes. The EDC-model was developed for prediction of gaseous combustion reactions in turbulent flows. It is based on the assumption that the reaction time scales can be related to the dissipation of turbulent eddies which contains the reactants and products (Magnussen and Hjertager, 1976). There are two main differences between mixing of reactants in a gas phase and a liquid phase, which are of importance when reacting flows are to be modelled. The first difference is that the coefficient of molecular diffusion is much higher in gases than in liquids, meaning that the Schmidt number in the gas phase is much smaller (Sc~1) than in the liquid phase (Sc>>1). The second difference results from the density variation of the gas phase and the resulting sensitivity of the gas phase density to pressure and temperature variations (Baldyga and Bourne, 1999). The EDC model can be used as a measure for mixing-controlled reactions and since concentration fluctuations are not accounted for, empirical parameters are needed for reasonable predictions. For liquid flows with high Schmidt numbers it is difficult to have universal parameters that account for structure differences in concentration fluctuations due to the Schmidt number effects. The EDC model can be viewed as using a single delta function to represent the bulk reaction rates. Since only mean equations are solved rate-limiting

parameters must be introduced to represent the effect of turbulence (Tsai et al., 2002).

When simulating chemical reactions a quantitative description of the state of the fluid by a Probability Density Function (PDF) is needed. This is because knowledge about average concentrations is not sufficient. This can be done by full PDF-simulations or by a presumed PDF-simulation. The problem can be divided into to parts: predicting the shape of the PDF and predicting the micro-mixing timescale. Monte-Carlo PDF methods are considered the state-of-the-art and the advantage with these methods is that the interaction between micro-mixing and reaction terms are resolved exactly (Tsai et al., 2002).

The multi-peak presumed PDF method proposed by Fox (1998) is a simple presumed PDF method for subgrid-scale concentration fluctuations that cannot be resolved on the CFD grid. Each cell in the computational domain is divided into a finite number of environments. The multi-peak PDF model can also be viewed upon as a presumed PDF composed of a finite number of peaks. The number of environments used affects the models ability to approximate the real PDF and when the number is increased, the description becomes more accurate, but the computational cost increase.

The model proposed by Baldyga et al. (1989) consists of two parts. The first part, the multiple timescale turbulent mixer model, is a cascade model for the decay of mixture fraction variance that includes the effects of dissipation rate at different stages of the scalar spectrum. The model requires solving three stages of variance and the final variance is the sum of the three stages. The second part is a model for the mean reaction rates based on the PDF shape of the mixture fraction. A beta distribution is assumed for the mixture fraction PDF. By solving the mean and the three stage variance equations, a beta density function is assigned as the mixture fraction PDF and a linear relationship is assumed between reactants and mixture fraction (Tsai et al., 2002). The multi-peak presumed PDF model is much cruder than Baldyga's model (i.e discrete vs continuous), however the reactant concentrations are treated exactly and the multi-peak presumed PDF model is easier to implement in an existing CFD code. (Piton et al., 2000)

Models that demand only moderate computational times while still taking into account the in-homogeneity of the reactor are of practical interest (Kruis and Falk, 1996). These types of models will be able to give a better precision level in the analysis of chemical reactions in reactors.

1.1 Previous work

1.1.1 Experiments

Passive mixing

From literature it can be found that the combined PIV/PLIF technique has been successfully employed the last few years. Aanen et al. (1999) developed a combined measurement technique in which they use PIV and LIF simultaneously, without influencing each other. They have tested the reliability and precision of the technique by measuring the mixing of a point source placed in the centre of a fully developed turbulent pipe flow. The experimental results were compared against results of a direct numerical simulation (DNS) and against analytical results. The agreement was satisfactory.

Fukushima et al. (2000) have studied mixing of a passive scalar in a self-perserving axisymmetric jet at a Reynolds number of 2×10^3 by using the combined PIV/PLIF technique. The results agreed well with results from DNS and previous experimental data.

Law & Wang (2000) have developed a combined PIV and PLIF set-up and demonstrates that it can be used to successfully capture the mean and turbulent mass transport characteristics in a mixing process. The combined set-up was applied to a turbulent jet discharging into a stagnant environment. They compared the various mass transport quantities measured to already existing data and the comparisons were mostly satisfactory.

Tsai et al. (1999) have developed a simultaneous PIV/Reactive PLIF system. They have applied the system to measure velocity and reacting species concentration in a mixing layer. The measurement results are compared to CFD simulations and they found the CFD predictions of mean concentration to be satisfactory.

Borg et al. (2001) have developed a simultaneous PIV/PLIF technique and have applied the technique to measure concentration and velocity in the near inlet region of a turbulent jet. They have compared their measurements with large eddy simulations (LES) and earlier experimental data, and they found the general agreement to be good.

Meyer et al. (2000) have also performed measurement with PLIF combined with PIV. They considered the mixing of a jet in a fully developed cross-flow in a square duct. They compared their results with measurement in the same set-up by the use of point wise LIF and LDA. They reported that the two techniques in general gave results in good agreement. Meyer et al. (2000) have described their experimental technique in great detail and their method is adopted in the work presented in this thesis.

Reactive flows

Previous work on measuring reactant and/or product concentrations in a reactive flow using PLIF is listed in Table 1.1. The method applied in the work presented in this thesis is based on the work of Koochesfahani and Dimotakis (1986), Komori et al. (1993) and Neudeck (1999). They have all studied acid-base reactions and used Sodium Fluorescein as the fluorescent dye. Koochesfahani and Dimotakis (1986) used Sulfuric Acid and Sodium Hydroxide as reactants whereas Komori et al. (1993) and Neudeck (1999) used Acetic Acid and Ammonium Hydroxide. Koochesfahani and Dimotakis (1986) and Komori et al. (1993) both used an Ar+ laser (488nm) to excite the dye while Neudeck (1999) used a 532 nm pulsed laser.

Pohorecki and Baldyga (1983) have performed experiments in a tubular reactor where they found the conversion length for an acid-base neutralisation at different Reynolds numbers.

Valerio et al. (1994) have performed experiments with neutralisation of NaOH with HCl in a tubular reactor with coaxial feeds. A fiber optic spectrophotometer was used to measure the axial concentration profile of NaOH. The experimental results were used to test the quality of the prediction of the reaction rate from models based on the assumption of a single controlling stage for mixing.

Table 1.1: Summary of previous work on measuring concentration in a reactive flow.

	Acid	**Base**	**Dye**	**Technique**	**Laser**	**Filter**	**Measured quantity**
Koochesfahani and Dimotakis (1986)	Sulfuric Acid (H_2SO_4)	Sodium hydroxide (NaOH)	Sodium Fluorescein ($C_{20}H_{10}Na_2O_5$) added to the acid	LIF	(Ar^+) laser (488nm)		Reaction product concentration
Walker (1987)	Citric Acid (C_3H_4OH (COOH))	Sodium hydroxide (NaOH)	Sodium Fluorescein ($C_{20}H_{10}Na_2O_5$) added to the acid	LIF	(Ar^+) laser (488nm)		Reaction product concentration
Komori et al. (1991)	Acetic Acid (CH_3COOH) C_{A0}=10 mol/m^3	Ammonium hydroxide (NH_4OH) C_{B0}=10 mol/m^3	Sodium Fluorescein ($C_{20}H_{10}Na_2O_5$) 5×10^{-5} mol/m^3 added to both acid and base	Combined LIF and electrode-conductivity	(Ar^+) laser (488nm)		Acid concentration and reaction product concentration
Komori et al. (1993)	Acetic Acid (CH_3COOH) C_{A0}=10 mol/m^3	Ammonium hydroxide (NH_4OH) C_{B0}=10 mol/m^3	Sodium Fluorescein ($C_{20}H_{10}Na_2O_5$) 5×10^{-5} mol/m^3 added to both acid and base	Combined LDV and LIF	(Ar^+) laser (488nm)		Velocity and concentration of acid
Zipp and Patterson (1998)	Hydrochloric acid (HCl)	Sodium hydroxide (NaOH)	Fluorescein (uranine) 10^{-6} mol/l added to base	Fiberoptic probe (485 nm light)			Base concentration
Neudeck (1999)	Acetic Acid (CH_3COOH) C_{A0}=10 mol/m^3	Ammonium hydroxide (NH_4OH) C_{B0}= 4.29 mol/m^3	Sodium Fluorescein ($C_{20}H_{10}Na_2O_5$) 0.08 mol/m^3 added to both acid and base	Combined PIV and PLIF	532nm pulsed laser	550 nm	
Tsai et al. (1999)	Hydrogen-peroxid (H_2O_2)	Iron hydroxide Fe(II) = ($Fe(OH)_2$)	Rhodamine WT added to both acid and base	Combined PIV and PLIF	532nm pulsed laser	590 nm	

1.1.2 Simulations

Hannon et al. (1998) have tested two different models for chemical reactions; the EDC model and Baldyga's model (1989). The results from the numerical simulations were compared to the experimental results presented by Pohorecki and Baldyga (1983). Hannon et al. (1998) showed that the EDC model was not able to predict the conversion length, and argued that this was because the EDC model contains no information on mixing at scales where viscous/diffusive effects are important. They found that Baldyga's model could predict the length within a reasonable accuracy.

Valerio et al. (1994) have tested the quality of prediction of the reaction rate from models based on the assumption of a single controlling stage for mixing by comparison with experimental data concerning the neutralization of NaOH with HCl in a tubular reactor with coaxial feeds. The EDC model was able to give qualitative agreement with experimental data and permit good estimation of the length of the reaction zone. The model constant, C, was set to 1.

Tsai et al. (2002) have compared results from the EDC model, the multi-peak presumed PDF model and Baldyga's model for the reactive liquid mixing layer experiment of Komori et al. (1993). The EDC model required adjustment of the model constant, C, to fit the experimental data correctly. C=0.8 was found to give the best results. The multi-peak model using the timescale formulated by Corrsin (1964), which includes the high Schmidt number effect of liquids, matched reasonably well with the experimental data. Baldyga's model did not predict the experimental data well.

Marchisio et al. (2001) has compared multi-peak presumed PDF predictions and full PDF predictions with experimental data. The experimental data was obtained from a tubular reactor in which turbulent precipitation of barium sulfate was carried out from aqueous solutions of barium chloride and sodium sulfate. Full PDF predictions and multi-peak presumed PDF predictions gave similar results.

Kolhapure and Fox (1999) have used the multi-peak presumed PDF model to describe the small-scale mixing of chemical species inside a tubular low-density polyethylene (LDPE) reactor under different

operating conditions. The results have been compared to full PDF methods used in the literature for similar studies. They found that the multi-peak presumed model offers a computationally highly efficient description of the turbulent reacting flow inside the LDPE reactor.

Marchisio et al. (2000) have used barium sulphate precipitation from non–premixed aqueous solution of sodium sulphate and barium chloride to validate the multi-peak presumed PDF model applied to a semi-batch Taylor-Couette reactor. They found that the overall agreement with experimental data was satisfactory, but pointed out that a deeper investigation of the flow field is required to completely verify the effect of turbulence parameters on the degree of mixing at various scales in the reactor.

Piton et al. (2000) have also applied the multi-peak presumed PDF model to perform CFD simulations of barium sulphate precipitation. Fast kinetics at molecular scale is involved in this process and therefore micro-mixing affects precipitation reactions and requires suitable models when implemented in a CFD simulation. The results are compared to earlier studies based on Baldyga's model (Baldyga et al., 1997; Baldyga and Orciuch, 1999) and the results predicted from the multi-peak presumed PDF model and Baldyga's model are very similar.

Fissore et al. (2002) have compared three different PDF models, namely full PDF, multi-peak presumed PDF and beta-PDF (Baldyga's model). The comparison was carried out in an ideal perfectly mixed batch reactor. Competitive-consecutive and competitive-parallel reaction schemes were used to test model performances. The comparison showed that the agreement between the approaches is good. The multi-peak presumed PDF model and beta-PDF model (Baldyga's model) gave comparable results. The multi-peak presumed PDF model has the advantage of being simpler and faster.

Baldyga and Orciuch (2001) studied precipitation of barium sulphate in an un-premixed feed, two-dimensional tubular precipitator both experimentally and numerically by using Baldyga's model. The flow field was computed using the k-ε model. In general there was good agreement between the model predictions and the experimental data.

1.2 Objective

The objective of this thesis is to provide experimental data for passive and reactive mixing in a mixing channel. This will be done to be able to test the performance of different turbulence models, mixing models and reaction models.

An experimental set-up of a mixing channel is designed and experiments with mixing of two passive fluids and mixing of two reacting fluids is performed. The passive mixing is measured by the use of a combined PIV/PLIF laser measurement technique, which gives information about velocity and concentration fields. A reactive-PLIF method is used to measure product concentration in the reactive mixing case. This is done to get more knowledge about the mixing process and mechanisms and to se how this effects the chemical reaction. The experimental results are also used to verify the numerical models to see if they are able to predict the processes of interest.

The flow field of interest must be modelled as correct as possible for the effects of the flow field on the chemical reaction to be correct. In this work turbulence is modelled by using the widely used k-ε model. The RNG and Chen-Kim version of the model is also tested. The mixing and reaction is modelled by the EDC-model and different variations of that model. The double peak PDF model, the beta-PDF (Baldyga's) model and the multi-peak presumed PDF model are also used.

1.3 Outline of thesis

The rest of this thesis consists of an Experimental part and a Numerical part. The Experimental part starts in Chapter 2 with an introduction to the theoretical background of the laser based measurement techniques PIV and PLIF. In Chapter 3 the experimental findings in a mixing channel obtained by the combined PIV/PLIF system is presented. In Chapter 4 the experimental findings in a reactive mixing channel obtained by the reactive-PLIF method is presented. The Numerical part starts in Chapter 5 with an introduction to the numerical models used in the simulations. In Chapter 6 different reaction models are tested against experimental and numerical data available from the literature. In Chapter 7 and 8 numerical predictions are evaluated against the experimental findings presented in

Chapter 3 and 4, respectively. Chapter 9 presents conclusions and recommendations for further work.

Part I

Experiments

Chapter 2

Measurement techniques

2.1 Introduction

In order to validate the performance of CFD models, detailed experimental data is required. In the study of turbulent mixing there is a need for non-intrusive techniques that can provide a whole field of mean and fluctuating velocity and concentration. Particle Image Velocimetry (PIV) and Planar Laser Induced Fluorescence (PLIF) are techniques that can provide such information. In this chapter, the theory behind these two techniques will be briefly described.

2.2 Particle Image Velocimetry (PIV)

2.2.1 Theory

The Particle Image Velocimetry (PIV) technique can provide instantaneous velocities in a whole field. The principle of PIV is that the flow of interest is seeded with small tracer particles that ideally follow the flow. A cross-section of the flow field is illuminated with a laser-sheet and the scattered light from the particles is recorded with a digital camera. Two images are recorded with a short exposure time delay, Δt. The images are divided into a number of interrogation areas (IA's), and the corresponding IA's in the two images are correlated with each other, see Figure 2.1. If the IA's contains enough particles a distinct correlation peak can be detected which correspond to the displacement of the

particles, $\vec{S}_D(x,t)$, in the IA, see Figure 2.1. The displacement divided by the exposure time delay gives the velocity vectors in each IA

$$\vec{v}(x,t) = \frac{\vec{S}_D(x,t)}{M\Delta t} \tag{2.1}$$

Here M is the magnification of the camera. The correlation between the two images can be performed using different cross-correlation techniques.

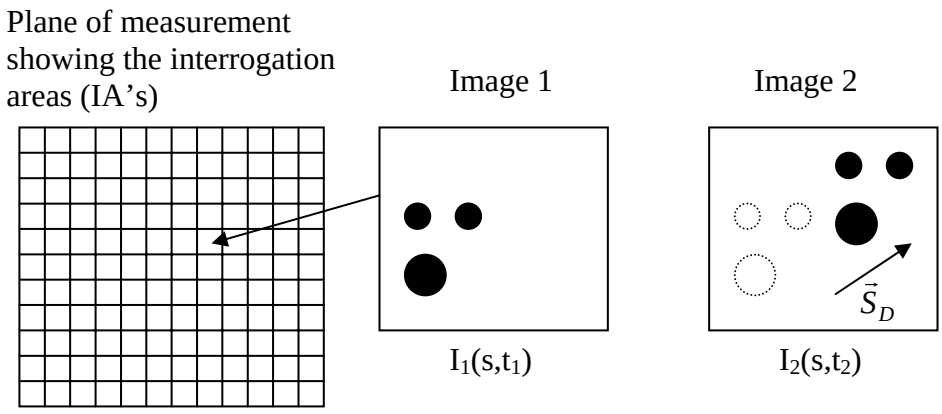

Figure 2.1: A Schematic overview of an image pair. The displacement vector, $\vec{S}_D$, is shown.

2.2.2 Adaptive correlation

In ordinary PIV cross-correlation techniques the corresponding IA's in the two images are correlated with each other and from the correlation function the final displacement ($\vec{S}_D$) is found. This is the first step in the adaptive correlation technique, where a guessed offset is introduced from the first IA to the second IA. The obtained vector is validated and used as a new estimate for the offset. A new run is then made but with a smaller IA. By using smaller IA's, more vectors are obtained. One could also use the same IA size in the second run and thereby improve the signal-to-noise ratio instead of increasing the number of vectors. The advantage of using the shifted IA's is that particles that have left the IA during the time

between pulses can be captured, and thereby the signal strength is raised. The dynamic range is also increased because the time between the two pulses can be increased. Figure 2.2 shows a schematic overview of the adaptive correlation technique. (Dantec Measurement Technology, 2001)

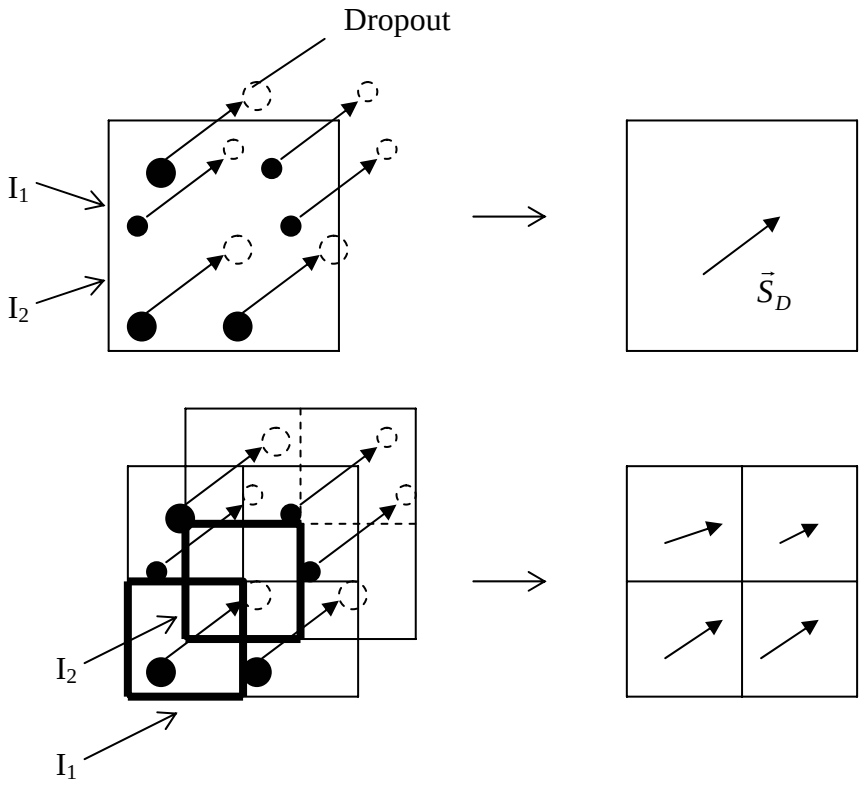

Figure 2.2: A schematic overview of the adaptive correlation technique.

2.3 Planar Laser Induced Fluorescence (PLIF)

2.3.1 Theory

The principle of the laser induced fluorescence technique is that molecules are excited to higher levels of energy via laser absorption. The decay to the fundamental state causes light emission, and the intensity of this fluorescence is a function of the concentration. Emission occurs at larger wavelength than the exciting laser radiation. This is useful to

distinguish between the fluorescence signal and the incident laser radiation. The relationship between the local fluorescence intensity and the local concentration, when taking absorption effect into consideration, can be expressed by the following equation (Guillard, 1999)

$$I = \alpha \cdot C \cdot e^{-\beta \cdot C} \tag{2.2}$$

Here α and β are two local coefficients related to experimental parameters (including quantum efficiency, radiation power, extinction coefficient, optical path, etc.). The parameters α and β can be determined from calibration experiments. If the dye concentration is kept sufficiently low (the exponential term tends to 1), such that the absorption due to dye is negligible, a linear relationship can be assumed (Law and Wang, 2000)

$$I = \Phi \cdot C \tag{2.3}$$

The parameter Φ can be determined by careful calibration before or during the actual measurement.

2.3.2 Calibration of the measurement system

The fluorescent dye, Rhodamine 6G, with maximum absorption at 530 nm is used in combination with a pulsed Nd:YAG laser with a wavelength of 532 nm. Since the laser wavelength is close to the maximum absorption of the dye, this combination will give a signal that is close to the maximum obtainable with this dye.

To check for the validity of Equation (2.3), a linearity test at static conditions can be performed (Ullum, 1999). The signal is monitored at positions of different intensity levels in the laser sheet, and with different known concentration levels. The test points are placed in three different intensity regions: A high intensity region (P1), an intermediate intensity region (P2) and a low intensity region (P3).

The measurement of the signal in a test point is based on an area average of 64×64 px^2 from the ensemble average of 20 frames. Figure 2.3 shows the results of the static test in all three test points. The results are fitted with a linear regression, and the data from the regression analysis is shown in Table 2.1.

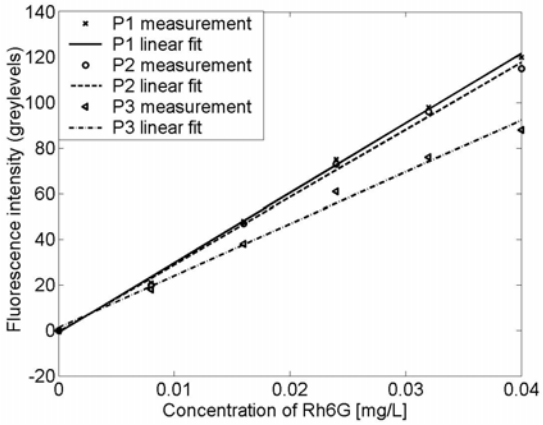

Figure 2.3: Fluorescence intensity versus concentration of Rhodamine 6G, in the test points P1-P3.

Table 2.1: Results of linear regression fit of fluorescence intensity versus concentration of Rh6G.

Point	**r_{reg}**
P1	0.998
P2	0.997
P3	0.991

From Figure 2.3, Rhodamine 6G concentrations equal to or less than 0.04 mg/L are seen to ensure a linear correlation. This has also been shown by Ullum (1999). The regression coefficient, r_{reg}, can be used to quantify the degree of correlation between two variables, $r_{reg}=1$ represents a perfect correlation. According to Guillard (1999) a linear regression coefficient greater than or equal to 0.990 represents a good estimate.

In Figure 2.4, a typical point calibration curve for the mean fluorescence signal including the statistical 95% limits (+/- 2 standard deviations) is shown. The mean deviation is 1.55 greyscales and the 95% limit is 4 greyscales.

Since the laser energy is not measured there is an error introduced in the instantaneous concentration data processing due to pulse-to-pulse variation. This error was examined by sampling continuously 20 images from a uniform dye solution with a concentration of 0.04 mg/L at the three test points. Figure 2.5 shows the pulse-to-pulse variation in laser

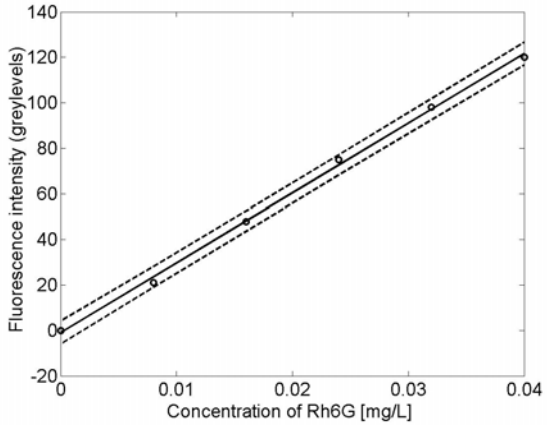

Figure 2.4: A typical calibration curve for Rhodamine 6G.

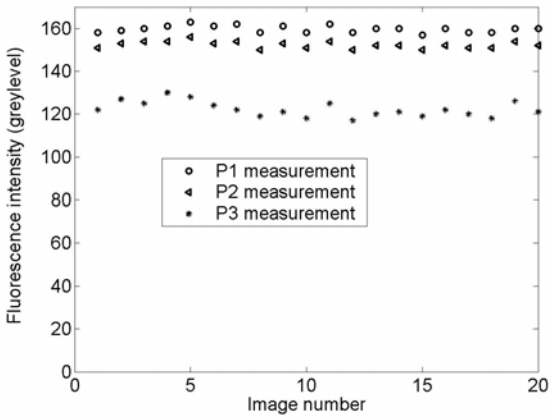

Figure 2.5: Pulse-to-pulse variation in laser energy.

energy. The standard deviation from mean in P1 and P2 was less than 2 greyscales, in P3 the deviation from mean was less than 4 greyscales.

2.3.3 Processing of the data

The background emission is recorded when C=0 mg/L, and an average of 20 images corresponds to the intensity of the mean background noise, I_{back}. The optical system imperfections are mapped in a reference image, I_{ref}, where the concentration is homogeneous. The average of 20 images with maximum concentration, C=0.04 mg/L, was used as reference, I_{ref}.

The instantaneous concentration can then be found from

$$\tilde{C}_i^* = \frac{\tilde{C}_i}{C_{max}} = \frac{I_i - I_{back}}{I_{ref} - I_{back}} \tag{2.4}$$

The images are subdivided and concentrations are extracted in interrogation areas as local spatial averages. The concentration $\tilde{C}$ is decomposed into a mean value, *C*, and a fluctuating value *c*.

The mean concentration is found from

$$C = \frac{1}{N} \cdot \sum_{i=1}^{i=N} \tilde{C}_i^* \tag{2.5}$$

the variance is found from

$$\sigma_C^2 = \frac{1}{N} \cdot \sum_{i=1}^{i=N} \left(\tilde{C}_i^* - C \right)^2 \tag{2.6}$$

and the standard deviation can be found from

$$c_{rms} = \sqrt{\sigma_C^2} \tag{2.7}$$

Here, N is the number of images.

2.4 Reactive-PLIF

2.4.1 Theory

The PLIF technique for measuring concentration in non-reactive flows can be extended to measure concentration in reactive flows. The fluorescent dye, Rhodamine 6G, which is often used for non-reactive flows is not sensitive to pH of liquid. The Sodium Fluorescein dye on the other hand is sensitive to pH of liquid and is therefore used as the fluorescent dye for reactive PLIF measurements. The concentration of a reacting species in a reactive liquid flow is then measured using the

dependence of the fluorescence on pH. To make quantitative measurements in the reacting case, the pH dependence of the dye and the pH of the reactants must be known. (Komori, 1993; Zipp and Patterson, 1998)

Sodium Fluorescein absorbs blue light, with peak absorption (excitation) occurring at wavelengths around 490 nm. Fluorescence (emission) occurs at the yellow/green wavelengths of around 520 nm. This means that an Ar+ laser is best suited for excitation of this dye. The exitation wavelength indicates only the wavelength at which maximum absorption occurs, this is the high point of a fairly broad absorption envelope, so absorption can occur up to 50 nm to either side. This means that an 532 nm pulsed laser also can be used to excite this dye, but the concentration of the dye must be higher to get the same emission levels as by using an Ar+ laser.

Sodium Fluorescein is sensitive to pH and fluoresces when the pH reaches a certain threshold value. Typically, the fluorescence is off when the pH<4 and maximum fluorescence is reached at pH=7, at pH≥7 the fluorescence is constant. The intensity is strongly dependent of the pH of the solution in the region pH<7. (Komori, 1993; Koochesfahani and Dimotakis, 1986)

The dye can be added to one of the reactants (Walker, 1987):

1) A jet containing acid and dye is injected into a base:
In this case the dye is ”turned on” by the increased pH produced by the acid-base reaction and the concentration of the reaction product can be measured

2) A basic jet with dye is injected into an acid:
In this case the reaction ”turns off” the dye and measurements of the reactant concentration can be made

In the first case the fluorescence intensity is directly proportional to the product concentration, where chemical product is defined as molecularly (dye-bearing) mixed fluid whose local pH is above the threshold. The local instantaneous product concentration, C_p, normalized with its

maximum possible value $C_{p,max}$, which is reached at the threshold conditions for fluorescence ”turn on” is given by

$$\frac{C_p}{C_{p.max}} = \frac{I}{I_{max}} \tag{2.8}$$

Here I is the measured fluorescence intensity and I_{max} is the maximal possible value reached at the fluorescence threshold condition.
(Koochesfahani and Dimotakis, 1986)

2.5 Error estimates

The theoretical standard error estimates can be found for the mean (M) and standard deviation (σ) of a population if one can assume a normal distribution of the samples and that they are sampled randomly and are independent. When the standard deviation is known, the formula

$$M - z \cdot \sigma_M < \mu < M + z \cdot \sigma_M \tag{2.9}$$

is used as a confidence interval of μ. Here

$$\sigma_M = \frac{\sigma}{\sqrt{N}} \tag{2.10}$$

and N is the sample size. For a 95% confidence interval z=1.96 and for a 99% confidence interval z=2.58, when a normal distribution is assumed. (Lane, 2004) This gives the following error estimates for the mean and standard deviation:

$$\varepsilon_\mu = z \cdot \frac{\sigma}{\sqrt{N}} \tag{2.11}$$

$$\varepsilon_\sigma = z \cdot \frac{\sigma}{\sqrt{2 \cdot N}} \tag{2.12}$$

Chapter 3

Measurement of turbulent mixing*

3.1 Introduction

In this chapter experimental data obtained by using the combined PIV and PLIF technique to measure turbulent mixing in a mixing channel for three different flow cases will be presented. Measurements are performed in the initial mixing zone and also further out in the channel. The objective is to provide measurement data that can be used to validate Computational Fluid Dynamic (CFD) simulations.

3.2 Experimental details

The combined PIV and PLIF technique was used for the measurements. PIV was used to measure the instantaneous velocity field and PLIF was used to measure the instantaneous concentrations. Figure 3.1 shows a schematic drawing of the experimental setup and the PIV/PLIF system. A pair of 15 Hz New Wave MiniLase pulsed Nd:YAG lasers with a beam expanding lens was used as light source giving a lightsheet thickness of Δz=3 mm. Two 8 bit cross-correlation cameras are used, both 30 Hz Kodak Megaplus ES 1.0, the PLIF camera is type 10 with a spatial resolution of 1008×1018 px^2 and the PIV camera is type 16 with a spatial resolution of 1008×1016 px^2.

*Partly based on: Hjertager, L.K., B.H. Hjertager, N.G. Deen and T. Solberg (2003). 'Measurement of turbulent mixing in a confined wake flow using combined PIV and PLIF'. *Canadian Journal of Chemical Engineering* **81**, 6, 1149-1158.

The PLIF camera was set to single frame mode and the PIV camera to double frame mode. 5 μm polyamide seeding particles were used for the PIV measurements and the fluorescent dye; Rhodamine 6G (Rh6G) was used for the PLIF measurements. The PIV camera was fitted with a 532 nm narrow band green filter to make sure that only the light scattered from the tracer particles were captured. The PLIF camera was fitted with a 570 nm cut-off filter ensuring that the fluorescent light was captured and at the same time blocking out the 532 nm green light.

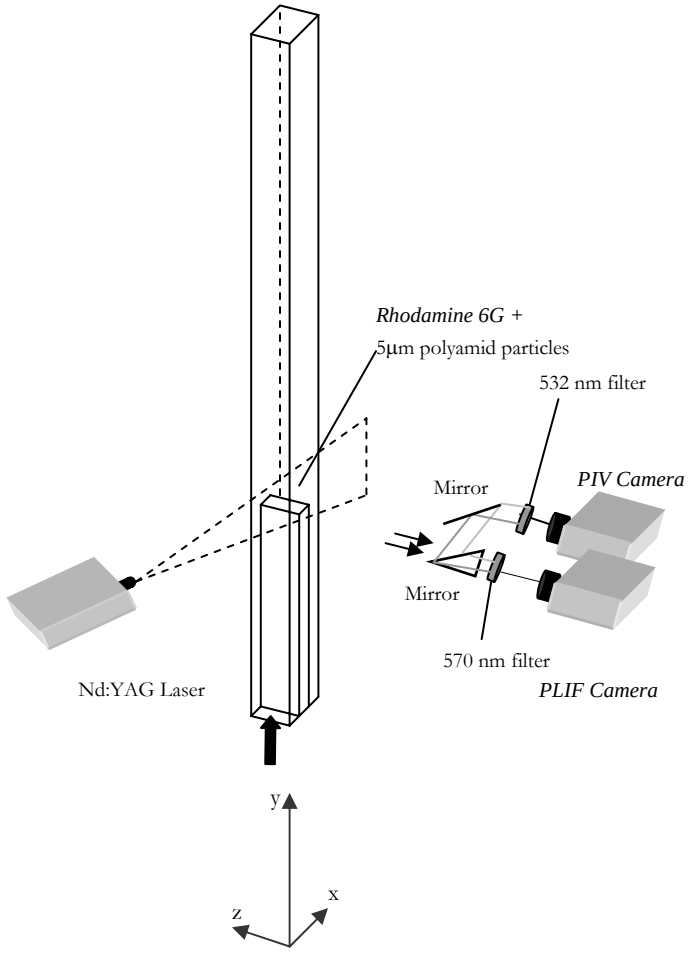

Figure 3.1: Schematic drawing of the experimental set-up and the PIV/PLIF system.

3.3 Experimental setup

The measurements were performed in a mixing channel with a cross section of 60×60 mm^2, a schematic drawing of the setup is shown in Figure 3.1. The first part of the channel was divided into two smaller feed channels with a cross section of 20×60 mm^2 by an obstruction of size 20×60×330 mm^3. This was done to allow mixing of two streams in the main channel. The fluid in the channel was tap water at room temperature.

The flow entered the feed channels from a feed chamber, which was divided by an obstruction with the same thickness as the obstruction in the feed channels. To get a smooth transition of the flow from the feed chambers it was fitted with a contraction. Preliminary measurements showed that this was not enough to straighten out the flow, therefore flow straightners were put into the first part of the feed channels. The channel has a total length of 970 mm, and the length available for mixing is 640 mm. The feed solutions were pumped from two large storage tanks each with a volume of 250 L. Both tanks contain water added with 5 μm polyamide seeding particles. In one of the tanks, 5 mL of the fluorescent dye in a solution of 2 g/L, was also added giving a concentration of 40 μg/mL Rh6G. The flow was pumped from the storage tanks via one flowmeter for each tank to control the flowrate in the mixing channel.

Figure 3.2 shows the three measurement positions. The initial mixing zone (Position 1 & Position 2) has been investigated and also an area further out in the channel (Position 3) was investigated to see the degree of mixing at this point. The measurements are made in the x-y-plane, yielding the U and V velocity components in x and y direction, respectively. Measurements were performed for three different flow cases, given in Table 3.1. For case 1, the bulk velocities in the feed channels were 0.17 m/s, which gave a Re number based on feed channel hydraulic diameter of 5100. The bulk velocity in the main channel was 0.11 m/s, which gave a Re number based on main channel hydraulic diameter of 6600. The bulk concentration in feed channel A, $C_{A,b}$ was normalized to 1.0 and the bulk concentration in feed channel B, $C_{B,b}$ was 0 for all three flow cases.

Table 3.1: Inlet bulk velocities for the different flow cases.

	Velocity (m/s)		Velocity ratio
Case	**Inlet A($V_{A,b}$)**	**Inlet B($V_{B,b}$)**	**($V_{A,b}/V_{B,b}$)**
1	0.17	0.17	1
2	0.085	0.17	0.5
3	0.0425	0.17	0.25

3.4 Data analysis

The response of the fluorescent light was monitored with 6 different dye concentrations in the system. This was done to ensure linear response to the dye concentration. In Figure 3.3, a typical point calibration curve for the mean fluorescence signal including the statistical 95% limits (+/- 2 standard deviations) is shown. More details about the calibration of the measurement system were given in Chapter 2.3.2.

Before recording the actual measurements the background emission was recorded by taking a series of 20 background images at each measurement position with no dye present in the water, i.e. a concentration, C_0=0 mg/L. An average of 20 images corresponds to the intensity of the mean background noise, I_{back} and this was used to set the zero value for the cameras response on variation in dye concentration. The optical system imperfections were mapped in a reference image where the concentration was homogeneous. The average of 20 images with maximum concentration, C_{max}=0.04 mg/L, was used as reference, I_{ref}, at each measurement position. This was done to be able to compensate for variable light distribution in the laser-sheet. The processing of the data was performed as described in Chapter 2.3.3. To find the grey-levels representing maximum and minimum concentration, positions in the images with known concentrations are used as reference values.

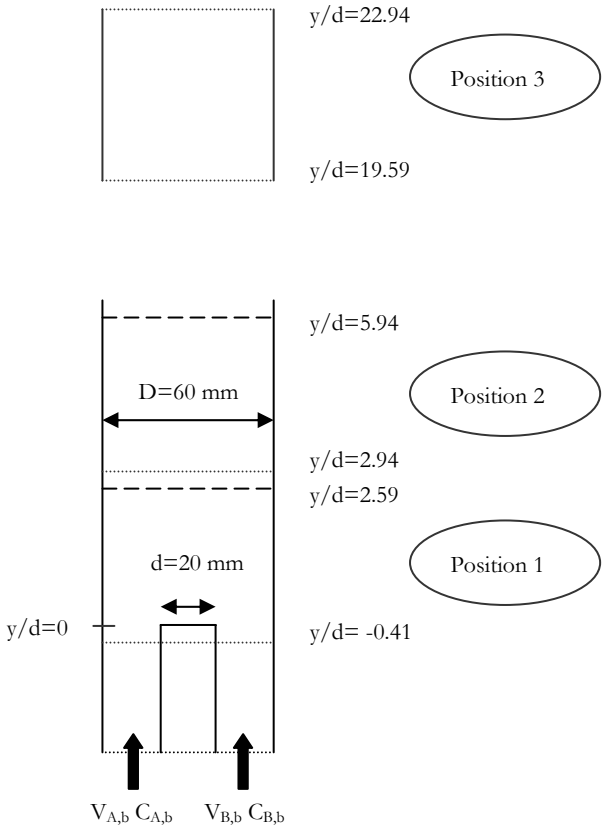

Figure 3.2: Sketch of the three measurement positions.

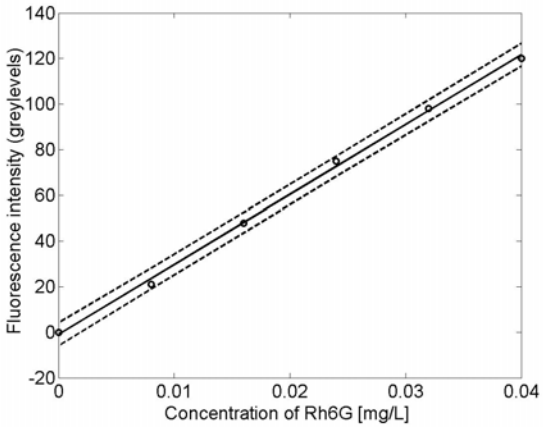

Figure 3.3: Fluorescence intensity versus concentration of Rh6G.

In the initial mixing zone, such areas were easy to find since the streams were not yet mixed. At the far end of the channel it was more difficult, and an image from the initial zone had to be used as reference for this position as well. The images were scaled based on the maximum and minimum concentrations.

For the PIV recordings an exposure time delay between the two images of Δt=5 ms was used, the measurement area was approximately 67×67 mm^2 at the three different measurement locations.

An adaptive correlation algorithm was used to capture both small and large velocities in the flow. The initial interrogation area for position 1 was 64×128 px^2 and final interrogation area was 32×64 px^2, which corresponds to an area of 2.1×4.2 mm^2. 50 % horizontal and 75 % vertical overlap between the interrogation areas was used. For position 2 and 3, the initial interrogation area was 64×64 px^2 and final interrogation area was 32×32 px^2, which corresponds to an area of 2.1×2.1 mm^2. 50% overlap between the interrogation areas was chosen in these cases. The size of the interrogation area was optimised for the velocities.

When the experiments were performed no cross-correlation between the two cameras was possible because of the equipment available. Instead the two cameras were carefully adjusted to have the same view. An error is introduced due to the fact that the PIV and PLIF camera image do not overlap 100%. There is a displacement of up to 5 px, which corresponds to 0.35 mm. The PLIF-coordinates is set equal to the PIV-coordinates, this gives less precise results than what would have been obtained if the cameras where cross-correlated and the exact displacement between the two images could be used to find the exact PLIF-coordinates according to the PIV-coordinates.

For the determination of ensemble-averaged velocity fields and turbulence statistics 200 image pair were used. At y/d=1 for the axial velocity (V) and the mean concentration (C), with a 95% confidence interval, the error is about 3.5 % for the mean and about 10% for the standard deviation. The mean velocity and the velocity fluctuation were found from 100, 200, 300 and 400 images and the difference in the results for 200 and 400 images was minimal, therefore a number of 200 samples were chosen to reduce the amount of data to be stored.

3.5 Results for case 1, velocity ratio 1:1

Figure 3.4 shows the instantaneous concentration field in the initial mixing zone (position 1 & 2), and at the position further out in the channel (position 3). Except for an area right behind the block, the concentration is seen to be in-homogeneously distributed in the two images that represent the initial mixing zone. Further out in the channel, the concentration distribution is more homogeneous.

3.5.1 Mean and fluctuating velocities

The mean axial velocity (V) along the centreline is shown in Figure 3.5. Backflow is observed in the separating flow behind the block. The mean recirculation region extends to y/d=1.5, which compares to a recirculation length of 1.4 measured by Lyn et al. (1995) for the flow past a square cylinder at a Reynolds number based on the average cross-sectional velocity and the cylinder diameter of 21400, a blockage ratio of 7% and an aspect ratio of 9.75.

Profiles of the mean axial velocity (V) and the mean transverse velocity (U) at three different axial positions are shown in Figures 3.6 and 3.7, respectively. Evident from the figures are the velocity profile in the feeding channels, the separating flow behind the block dividing the feeding channels, the recovery of the velocity defect in the wake flow and finally the approach to a fully developed channel flow.

The axial velocity fluctuations (v_{rms}) and the transverse velocity fluctuations (u_{rms}) are shown in Figures 3.8 and 3.9, respectively. The velocity fluctuations appear to be highest in the shear layers of the near wake were the mean velocity gradients are largest. Normalised peak values of about 0.3 for the axial velocity fluctuations and 0.25 for the transverse velocity fluctuations are observed at y/d=1. These velocity fluctuations are significantly smaller than those measured by Lyn et al. (1995) for the flow past a square cylinder. They measured normalised peak values of about 0.4 at y/d=1.5 for the axial velocity fluctuations and 0.9 at y/d=1.75 for the transverse velocity fluctuations. In their LDV measurement, they were able to separate the periodic and the random fluctuations.

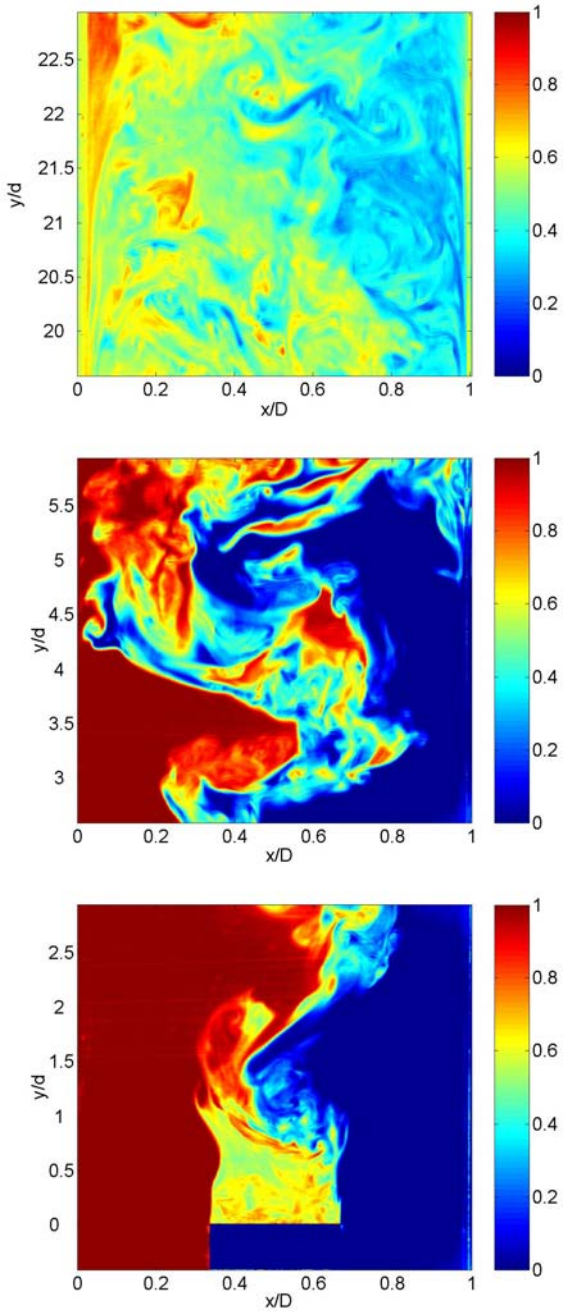

Figure 3.4: Instantaneous concentration fields at the different measurement positions along the channel (case 1).

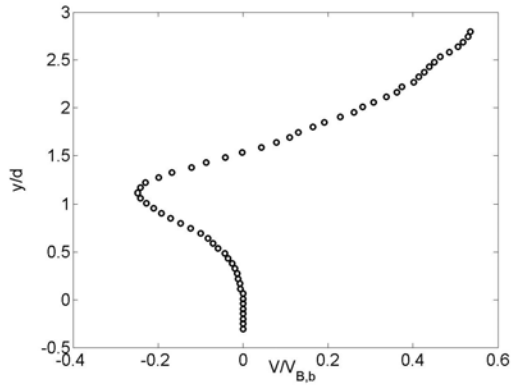

Figure 3.5: Axial velocity (V) along the centreline (case 1).

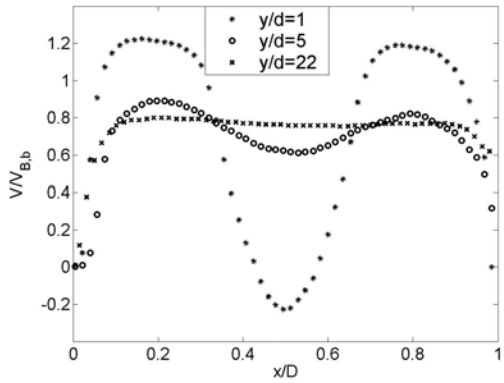

Figure 3.6: Axial velocity (V) at different axial positions (case 1).

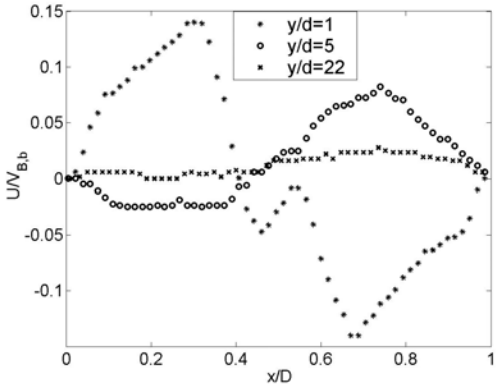

Figure 3.7: Transverse velocity (U) at different axial positions (case 1).

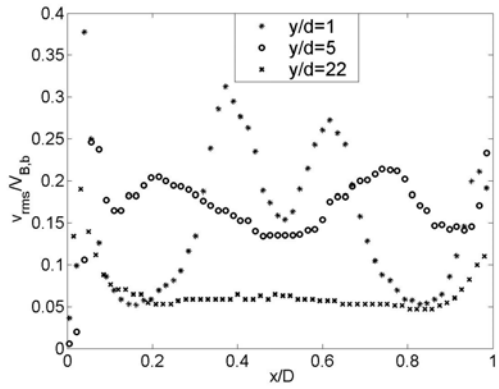

Figure 3.8: Axial velocity fluctuations (v_{rms}) at different axial positions (case 1).

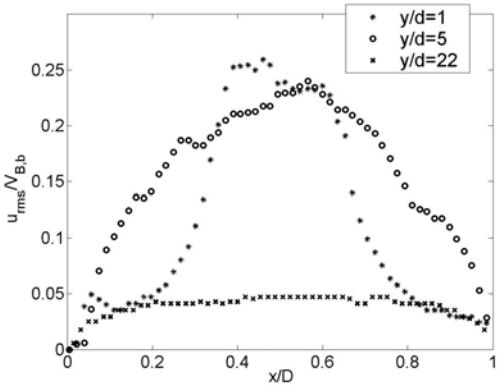

Figure 3.9: Transverse velocity fluctuations (u_{rms}) at different axial positions (case 1).

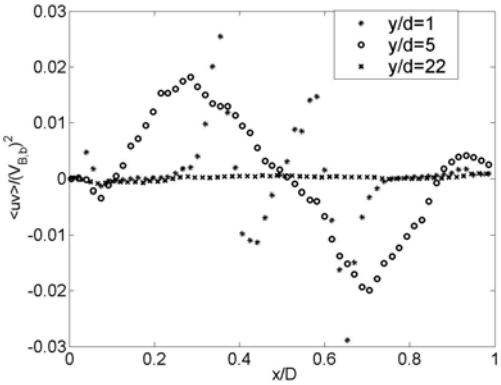

Figure 3.10: Reynolds shear stress (<uv>) at different axial positions (case 1).

The corresponding random velocity fluctuations showed normalised peak values of about 0.175 at y/d=1 for the axial velocity fluctuations and 0.3 at y/d=1.5 for the transverse velocity fluctuations, which are in better agreement with the measured velocity fluctuations in the present measurements. Apparently, the more confined wake flow in the present experiment (blockage ratio of 33% and aspect ratio of 3) gives less large-scale periodic motion than in the more unconfined wake flow behind the square cylinder.

A slight dissymmetry is noticed in the axial velocity profiles shown in Figure 3.6, which is also evident in the velocity fluctuations in Figures 3.8 and 3.9. Apparently, the flow in the two inlet channels has developed differently. Since the boundary layers along the outer channel walls appear to be mostly affected, the influence of the dissymmetry on the mixing in the wake behind the block dividing the inlet channels is considered to be small.

3.5.2 Reynolds shear stress

Figure 3.10 shows profiles of Reynolds shear stress (<uv>) at three different axial positions. As expected, the profiles are anti-symmetric around the centreline. At y/d=1 the normalised peak value of the shear stress is seen to be 0.025. This turbulent shear stress is significantly smaller than the one measured by Lyn et al. (1995) for the flow past a square cylinder. They measured a normalised peak value at y/d=1 of about 0.1 for the total shear stress comprising both periodic and random velocity fluctuations. The corresponding random velocity fluctuations showed normalised peak value of about 0.06 which is still larger than the one measured in the present measurement. The shear stress profiles at $y/d \geq 5$ seem to be closely related to the velocity gradient ($\partial V/\partial x$) which is expected to be the primary strain in the far wake of the block and in the fully developed channel flow downstream of the block.

3.5.3 Mean and fluctuating concentrations

Figure 3.11 shows the mean concentration field in the two overlapping areas in the initial mixing zone. Right behind the block dividing the two streams, there is a zone where the two streams are fairly well mixed compared to further out in the channel. The recirculation zone attached to

the block causes an increased mixing effect. Figure 3.12 shows the mean concentration profiles at different axial positions. The concentration is seen to become more uniform further out in the channel.

Figure 3.13 shows a contour plot of the concentration fluctuations in the initial mixing zone. From y/d=1 the fluctuations have a high value along the centreline. It can also be seen that the width of the shear layer grows from the inlet and out in the channel. Figure 3.14 shows the concentration fluctuations (c_{rms}) at different axial positions, and it can be seen that it increases from y/d=1 to y/d=5, and that it is smaller at y/d=22.

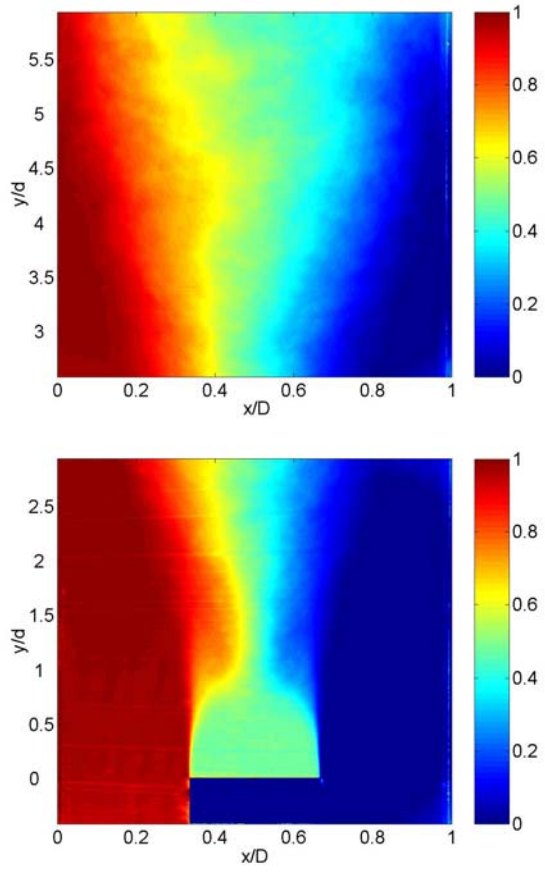

Figure 3.11: Mean concentration in the initial mixing zone (position 1 & 2, case 1).

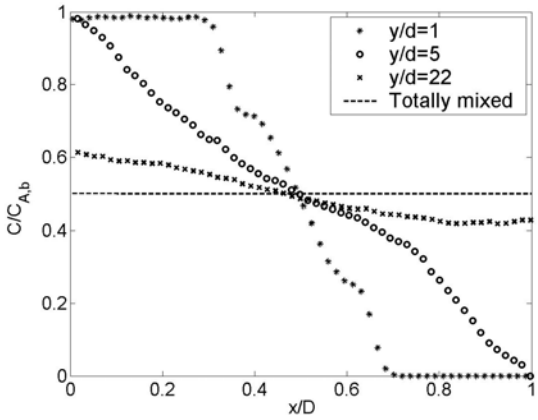

Figure 3.12: Mean concentration (C) at different axial positions (case 1).

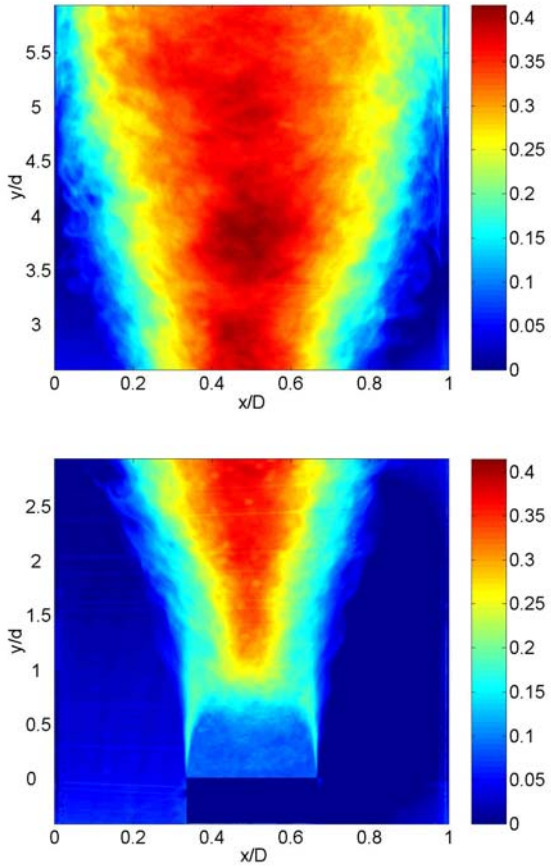

Figure 3.13: Concentration fluctuations in the initial mixing zone (case 1).

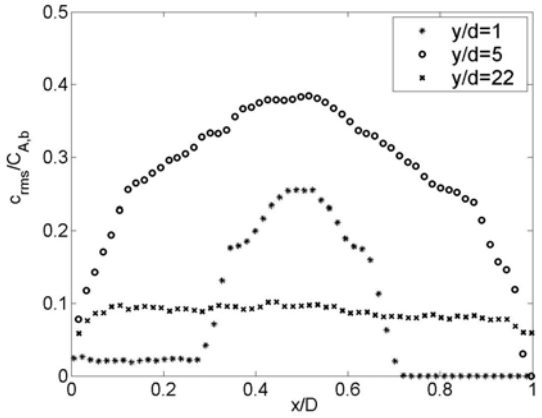

Figure 3.14: Concentration fluctuations (c_{rms}) at different axial positions (case 1).

3.5.4 Scalar Reynolds fluxes

The scalar Reynolds fluxes <uc> and <vc> represents turbulent transport of mean concentration in x- and y-direction, respectively. Figure 3.15 shows a vector plot of the scalar fluxes in the initial mixing zone. Apart from the recirculation zone, the scalar fluxes are noticed to go mainly in one direction, from high to low concentration. Figure 3.16 shows cross-sectional profiles of the scalar fluxes at y/d=5. The transverse scalar flux (<uc>) is seen to be positive over the cross-section, whereas the axial scalar flux (<vc>) is positive in the left half and negative in the right half of the cross-section.

Compared with the mean concentration profiles in Figure 3.12, the scalar Reynolds fluxes are noted to be in the opposite direction of the concentration gradients, indicating that turbulent transport of concentration can be described by the gradient diffusion hypothesis.

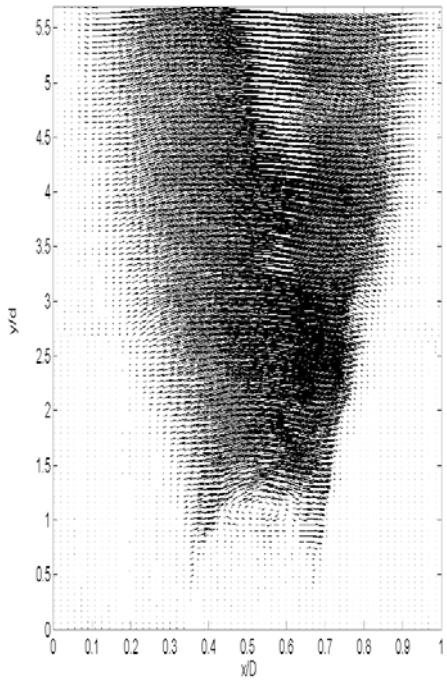

Figure 3.15: Mean scalar Reynolds flux in the initial mixing zone (case 1).

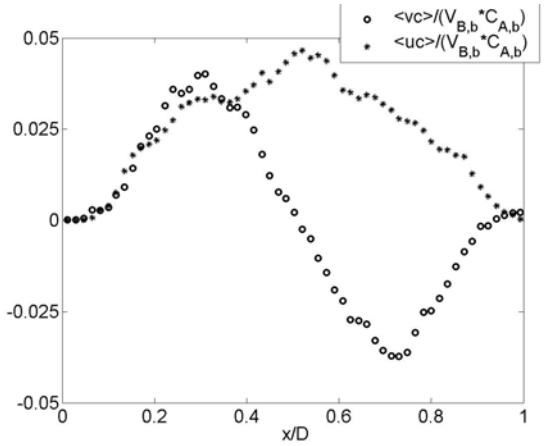

Figure 3.16: Scalar Reynolds fluxes at y/d=5 (case 1).

3.5.5 Analysis of degree of mixing

Macro- and micro-mixing

Mixing can be described as the process at which a non-uniform system is made uniform. The degree of mixing, or the uniformity, can be analysed by evaluating how well the flow is macro- or micromixed. Macro-mixing means that there is no mixing on molecular scale, but fluid elements are well mixed on a large scale. Micro-mixing is complete mixing of species even on a molecular scale.

A measure of uniformity is the Coefficient of Variation, CoV, which is the ratio of the standard deviation in concentration and the cross-sectional average of concentration, which can be expressed as (Bakker et al., 1998)

$$CoV = \frac{\sqrt{\sum_{i=1}^{N}\left(C_i - \langle C \rangle_A\right)^2}}{\langle C \rangle_A} \qquad (3.1)$$

Here $<C>_A$ is the cross-sectional average of concentration at a given axial position, C_i is the concentrations at the given axial position and N is the number of measurement points over the cross-section.

The coefficient of variation may be viewed as a measure of the macro-mixing. When the flow is totally unmixed, CoV=1, and when it is fully mixed, CoV=0.

To analyse the degree of micro-mixing another quantity called the decay function is evaluated. The decay function, d, can be expressed as the ratio between the cross-sectional average of the concentration fluctuations and the cross-sectional average of the concentration (Bird et al., 2002)

$$d = \frac{\langle c_{rms} \rangle_A}{\langle C \rangle_A} \qquad (3.2)$$

Here $<c_{rms}>_A$ is the cross-sectional average of concentration fluctuations.

The decay function starts at a value of d=0, when the flow is totally unmixed, increases to a certain peak value and decreases again and reaches d=0 when the flow is fully micro-mixed.

In Figure 3.17, the coefficient of variation CoV and the decay function d are plotted along the channel length. A cubic interpolation is made to give an impression of the curves in the region where experimental data are not available. The coefficient of variation starts at a value of CoV=1 at y/d=0, where the two inlet streams are totally unmixed. Just after the block dividing the two inlet streams, the coefficient of variation drops suddenly to a value of 0.85 indicating that the flow in the recirculation zone is well macro-mixed. Further downstream, the coefficient of variation decreases along the length of the channel. At the last measurement point the coefficient of variation is equal to a value of 0.15. A coefficient of variation of five percent or less (CoV≤0.05) is considered to be satisfactory for most industrial blending operations (Bakker et al., 1998).

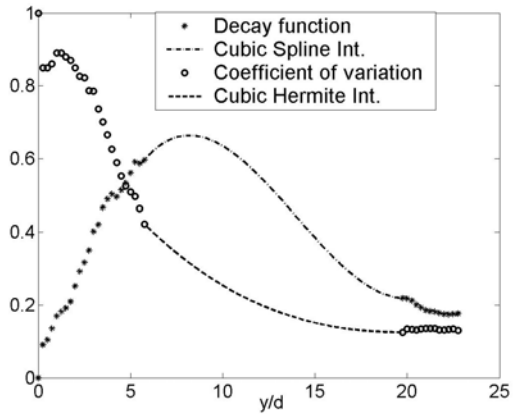

Figure 3.17: Coefficient of Variation and decay function (case 1).

The decay function is closely related to fluctuations in the concentration shown in Figure 3.14 as indicated by Equation (3.2). Since there are no concentration fluctuations in the inlet streams, the decay function is zero at y/d=0. Behind the block dividing the two inlet streams, the decay function increases with the increasing turbulent fluctuations in the separating shear layers. The decay function is estimated to reach a peak value of 0.65 at y/d=8. Further downstream, the decay function decreases as the velocity defect and thereby the turbulent fluctuations in the far

wake decreases. At the last measurement point, the decay function is somewhat larger than the coefficient of variation indicating that the flow is better macro-mixed than micro-mixed at this point.

Probability density functions (PDF)

The probability density function p(f) is a measure of the probability of a certain mixture fraction, f to occur in a particular position in the flow. The mixture fraction, f can be defined as:

$$f = \frac{\tilde{C}}{C_{A,b}} \tag{3.3}$$

where $\tilde{C}$ is the instantaneous concentration and $C_{A,b}$ is the bulk concentration in feed channel A.

Figure 3.18 displays PDF's at different positions in the flow. Along x/D=0.2 it can be seen that at y/d=0.5 the PDF is a single peak at f=1, further out in the channel it becomes a peak with a tail, and at the end of the channel, where the two streams are fairly well mixed the PDF becomes bell-shaped. A similar behaviour is seen along x/D=0.8, where at y/D=0.5 the PDF is a single peak at f=0, further out it becomes a peak with a tail and at the end it becomes bell-shaped. Along the centreline the PDF is bell shaped at y/d=0.5, and further out in the channel it becomes more flat with two smaller peaks on each side. At the end of the channel it becomes bell-shaped again. The PDF's support the results that are shown earlier, that there is a zone right behind the block were the two streams are fairly well mixed.

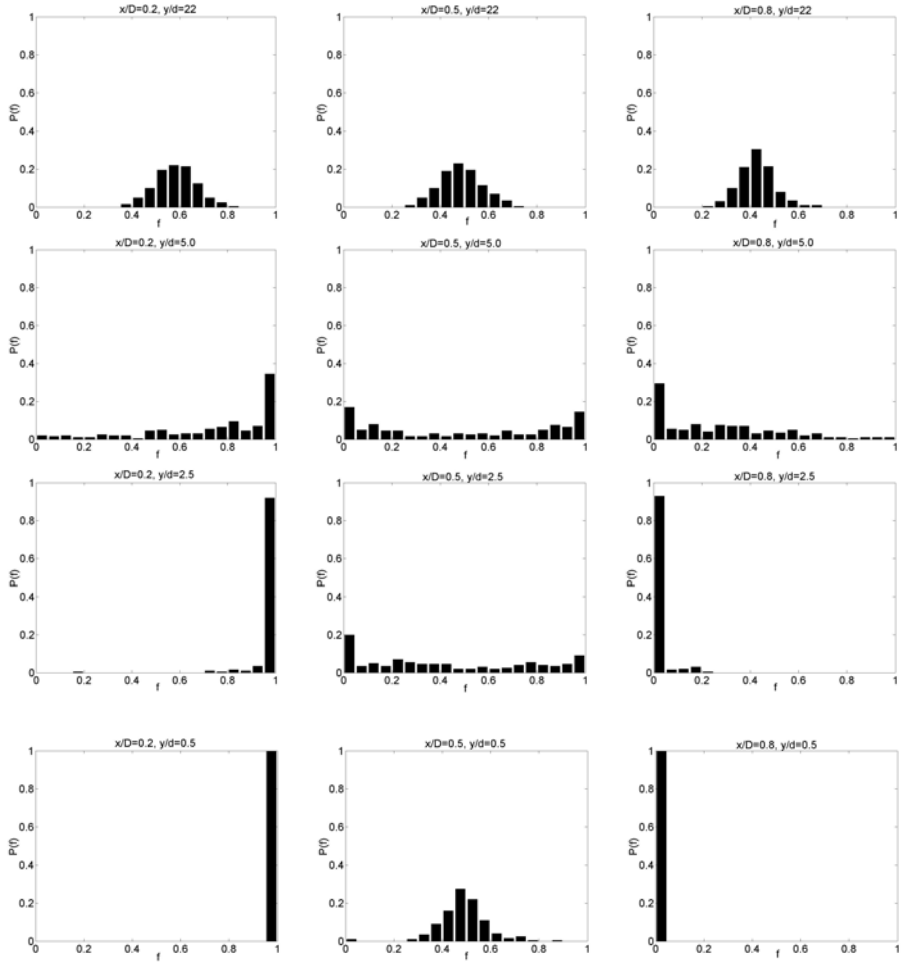

Figure 3.18: Probability density functions at different axial and transverse positions in the channel (case 1).

3.6 Results for case 2, velocity ratio 0.5:1

Figure 3.19 shows the instantaneous concentration field in the initial mixing zone (position 1 & 2), and at the position further out in the channel (position 3) for case 2. When comparing with the images in Figure 3.4 for case 1, the two streams are seen to be not as well mixed. At position 3, the concentration is far from being as homogeneously distributed as in case 1. Also, the transverse spreading is less than in case 1.

3.6.1 Mean and fluctuating velocities

Figure 3.20 shows the mean axial velocity along the centreline for case 2, and also for this case backflow is observed in the separating flow behind the block. The mean recirculation region extends to y/d=1.7, which compares to a recirculation length of 1.5 measured in case 1. The maximum negative velocity in the re-circulation zone for case 2 is half of the one measured in case 1, indicating that the mixing in the recirculation zone for case 2 is not as effective as in case 1.

Profiles of the mean axial velocity (V) and the mean transverse velocity (U) at three different axial positions for case 2 are shown in Figures 3.21 and 3.22, respectively. At y/d=1 the velocity of the flow coming from channel A is observed to be half of that from channel B. At y/d=5, the effect of this velocity difference is still significant, and at y/d=22, the effect is smaller but the velocity profile is clearly affected by this. At y/d=5, close to the left channel wall, negative velocities are observed, indicating that there is a backflow formed in this area. This very weak backflow can also be observed from the instantaneous concentration in Figure 3.19. It seems to be a transition from wake flow to a backward facing step in this case.

The axial velocity fluctuations (v_{rms}) and the transverse velocity fluctuations (u_{rms}) are shown in Figures 3.23 and 3.24, respectively. Normalised peak values of about 0.3 for the axial velocity fluctuations and 0.15 for the transverse velocity fluctuations are observed at y/d=1. Compared to case 1, the axial velocity fluctuation in the shear layer close to inlet B where the velocity is highest is approximately the same.

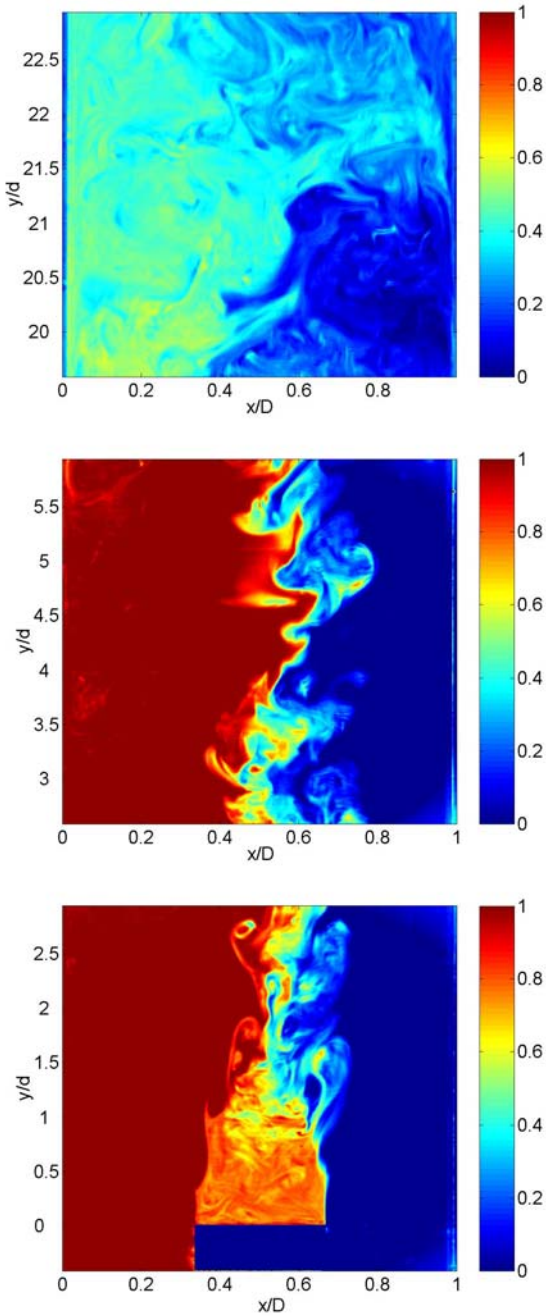

Figure 3.19: Instantaneous concentration fields at the different measurement positions along the channel (case 2).

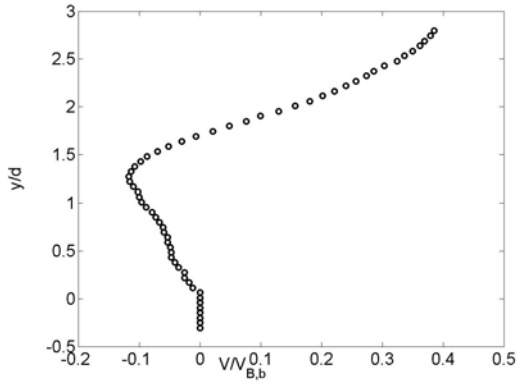

Figure 3.20: Axial velocity (V) along the centreline (case 2).

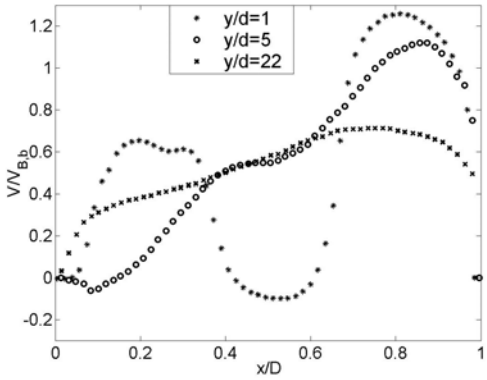

Figure 3.21: Axial velocity (V) at different axial positions (case 2).

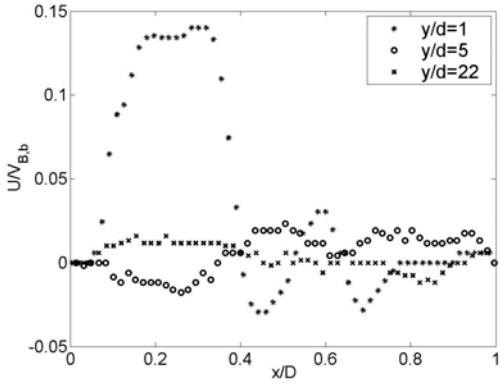

Figure 3.22: Transverse velocity (U) at different axial positions (case 2).

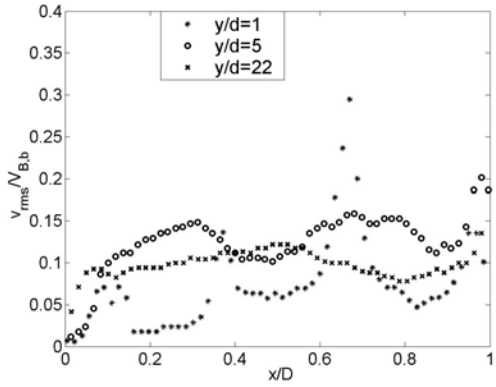

Figure 3.23: Axial velocity fluctuations (v_{rms}) at different axial positions (case 2).

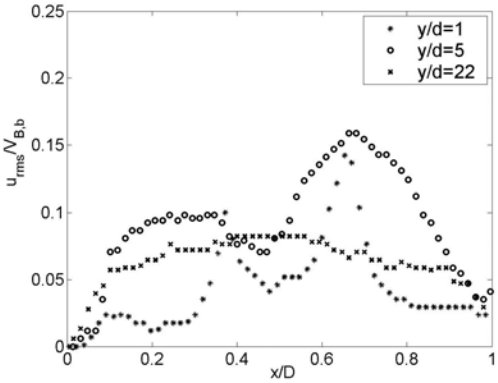

Figure 3.24: Transverse velocity fluctuations (u_{rms}) at different axial positions (case 2).

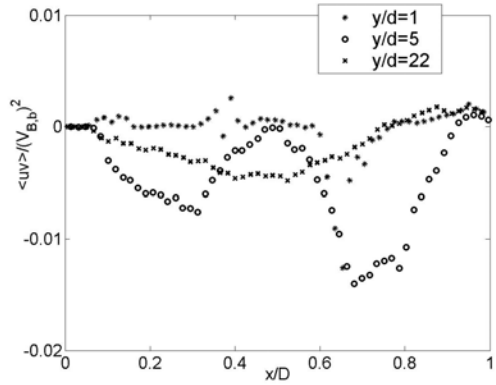

Figure 3.25: Reynolds shear stress (<uv>) at different axial positions (case 2).

The axial velocity fluctuation in the shear layer close to inlet A is almost half of the value in case 1. This corresponds well to the velocity in inlet A for case 2 which is half of the velocity in case 1. The transverse velocity fluctuations close to inlet B is about 0.15 compared to 0.25 for case 1, the lower velocity in inlet A has obviously a great impact on the transverse velocity fluctuations, and thereby the transverse spreading of concentration.

3.6.2 Reynolds shear stress

Figure 3.25 shows profiles of Reynolds shear stress (<uv>) at three different axial positions for case 2. At y/d=1, the normalised peak value of the shear stress close to inlet B is seen to be -0.013, and close to inlet A 0.003. This is significantly smaller than 0.025, which was measured in case 1.

3.6.3 Mean and fluctuating concentrations

Figure 3.26 shows the mean concentration field in the two overlapping areas in the initial mixing zone for case 2. As in case 1, the two streams are better mixed in the recirculation zone than further out in the channel. Here, the concentration has a value of about 0.7. This means that the low-velocity flow with concentration 1 is dominating in this area and that the high-velocity flow with concentration 0 is transported away from this area much faster. Figure 3.27 shows the mean concentration profiles at different axial positions. The concentration is seen to become more uniform further downstream in the channel, but has still not reached the value of 0.33 that is expected when the two streams are totally mixed in this case.

Figure 3.28 shows contour plots of the concentration fluctuations in the initial mixing zone. From y/d=2 the fluctuations have a high value along x/D=0.55. Compared to case 1 where the shear layer was placed in the middle of the channel (x/D=0.5), in this case it is moved towards channel B where the velocity is highest and thereby giving high velocity fluctuations that causes high concentration fluctuations. Figure 3.29 shows the concentration fluctuations (c_{rms}) at different axial positions. The concentration fluctuations at y/d=1 is highest at x/D=0.65, which again is caused by the velocity difference in the two inlet channels.

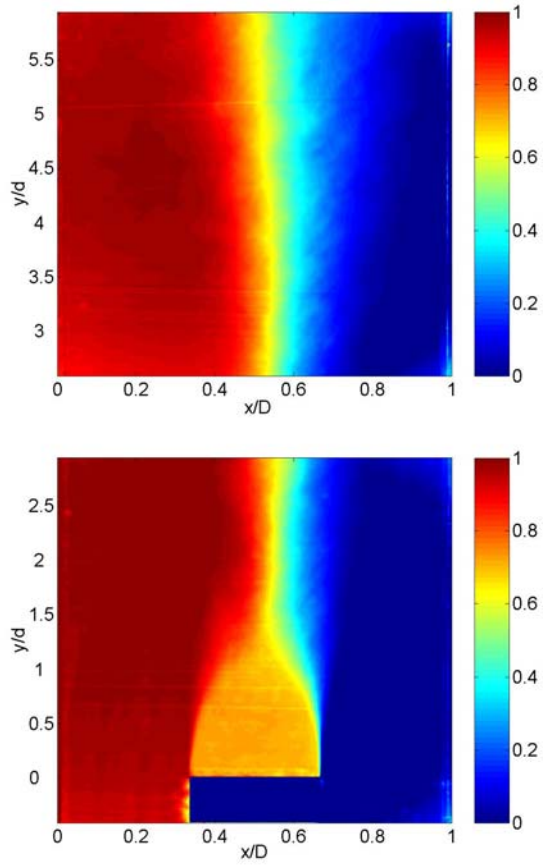

Figure 3.26: Mean concentration in the initial mixing zone (position 1&2, case 2).

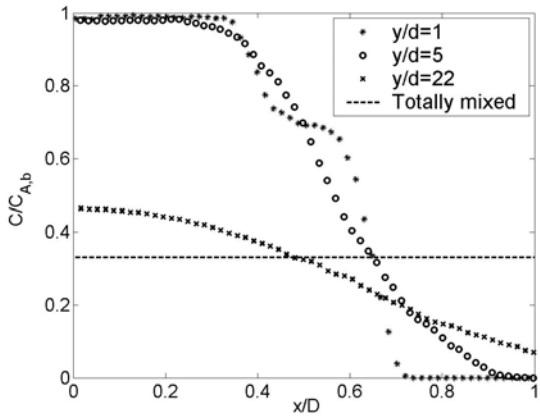

Figure 3.27: Mean concentration (C) at different axial positions (case 2).

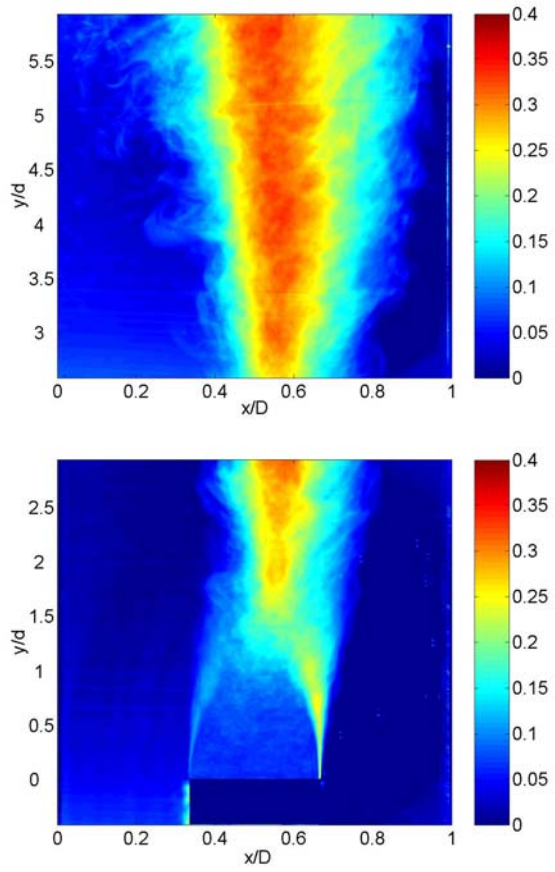

Figure 3.28: Concentration fluctuations in the initial mixing zone (case 2).

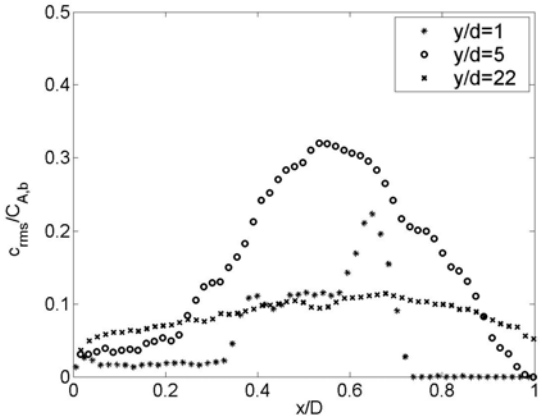

Figure 3.29: Concentration fluctuations (c_{rms}) at different axial positions (case 2).

3.6.4 Scalar Reynolds fluxes

Figure 3.30 shows a vector plot of the scalar Reynolds fluxes in the initial mixing zone for case 2. Comparing Figure 3.30 with Figure 3.15 it can be seen that the recirculation for case 2 is not as strong as for case 1. Figure 3.31 shows cross-sectional profiles of the scalar Reynolds fluxes at y/d=5. Compared to case 1, the scalar Reynolds fluxes seem to have lower values in this case.

Compared with the mean concentration profiles in Figure 3.27, the scalar Reynolds fluxes are noted to be in the opposite direction of the concentration gradients, indicating that turbulent transport of concentration can be described by the gradient diffusion hypothesis even in this case.

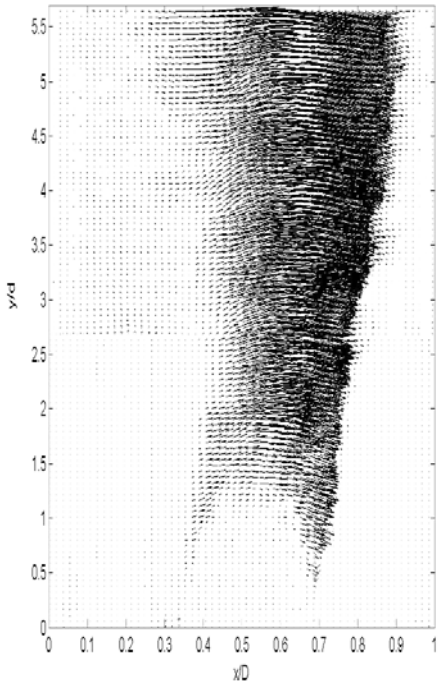

Figure 3.30: Mean scalar Reynolds flux in the initial mixing zone (case 2).

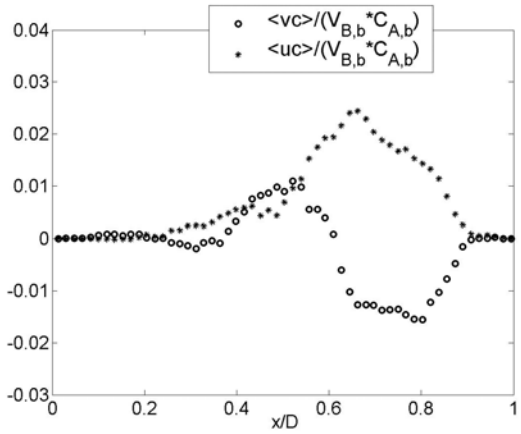

Figure 3.31: Scalar Reynolds fluxes at y/d=5 (case 2).

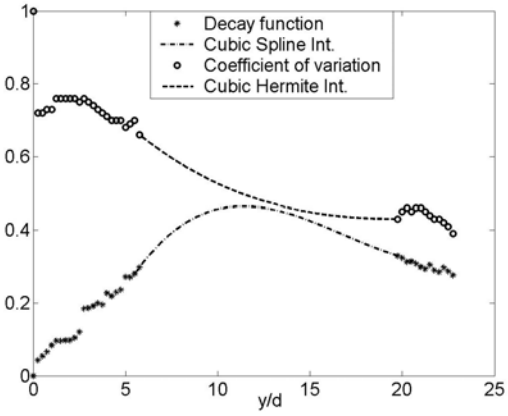

Figure 3.32: Coefficient of Variation and decay function (case 2).

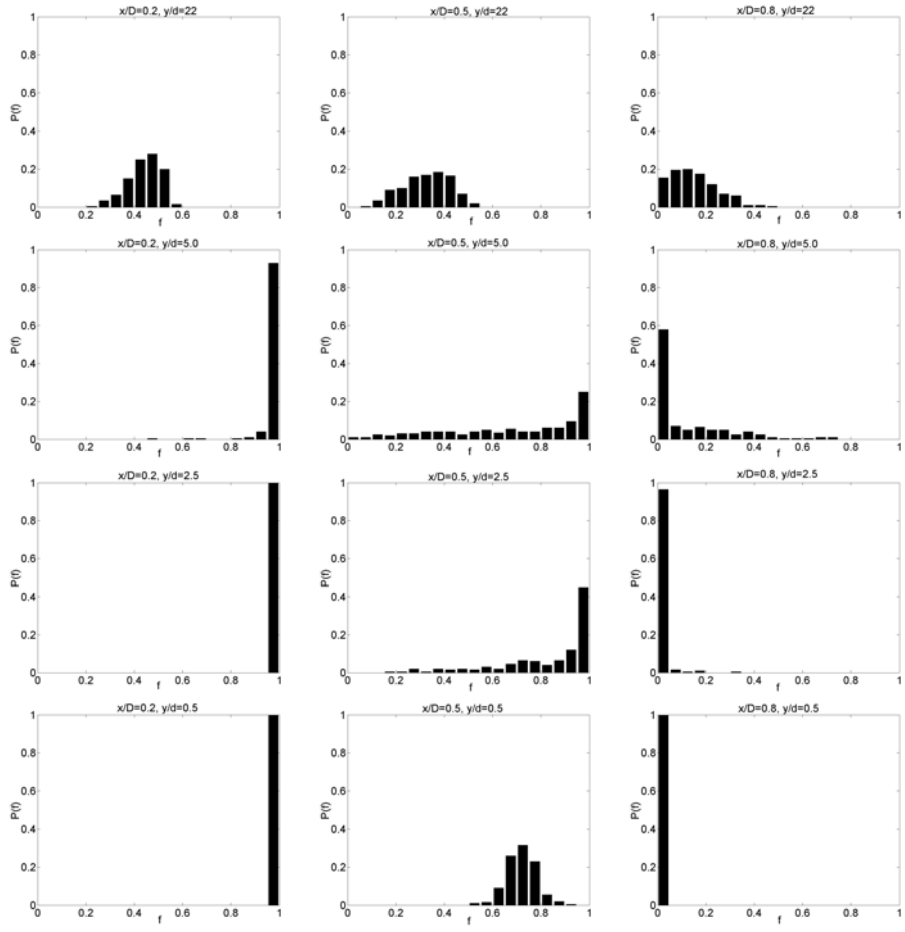

Figure 3.33: Probability density functions at different axial and transverse positions in the channel (case 2).

3.6.5 Analysis of degree of mixing

Macro- and micro-mixing

In Figure 3.32, the coefficient of variation CoV and the decay function d are plotted along the channel length. At the last measurement point the coefficient of variation is equal to a value of 0.38. In case 1, the value at the last measurement point was 0.15, meaning that case 1 is better macro-mixed than case 2 at this point.

The decay function is estimated to be smaller than the Coefficient of variation throughout the whole length of the channel. This indicates that the flow is better micro-mixed than macro-mixed. For case 1, an opposite behaviour was observed from y/d=5.

Probability density functions (PDF)

Figure 3.33 displays PDF's at different positions in the flow. Along x/D=0.2 the PDF at y/d=0.5 and 2.5 is seen to be a single peak at f=1. At y/d=5, the PDF becomes a peak with a tail, and at the end of the channel, the PDF becomes bell-shaped. In case 1, the tail starts already at y/d=2.5. This is because there is more transverse spreading in that case. Along the centreline the PDF is bell shaped at y/d=0.5 and it is located around f=0.7 compared to f=0.5 in case 1. The peak value is 0.32 and in case 1 it was 0.29.

From the PDF's it can be concluded that compared to case 1 the transverse spreading is smaller and there is more spreading towards the inlet with the higher velocity.

3.7 Results for case 3, velocity ratio 0.25:1

Figure 3.34 shows the instantaneous concentration field in the initial mixing zone (position 1 & 2), and at the position further out in the channel (position 3) for case 3. When comparing the images to the images in Figures 3.4 and 3.19, the two streams are seen to be not as well mixed right behind the block. Even at position 3, the flow is not so homogeneously distributed as for case 1 and 2. The main difference in this case compared to case 2 and 3 is that there is a recirculation zone formed along the left side of the channel where the flow is quite well mixed. The transverse spreading around x/D=0.65 is smaller than around x/D=0.5 in case 1 and x/D=0.55 in case 2. At y/d=5.5 the transverse spreading is better than for case 1 and 2 because of the backflow formed along the left side of the channel wall. This backflow ends/starts at y/d=0.5.

3.7.1 Mean and fluctuating velocities

Figure 3.35 shows the mean axial velocity (V) along the centreline for case 3. The mean re-circulation region extends to y/d=1.25, which compares to a recirculation length of 1.5 measured in case 1, and 1.7 measured in case 2. The maximum negative velocity in the recirculation zone for case 3 is much smaller than of the one measured in case 1 and 2, indicating that the re-circulation behind the block is not so strong as in case 1 and 2.

Profiles of the mean axial velocity (V) and the mean transverse velocity (U) at three different axial positions for case 3 are shown in Figures 3.36 and 3.37, respectively. At y/d=5 negative axial velocities are observed between x/D=0 and x/D=0.25, this corresponds well with the backflow observed in Figure 3.34. The backflow is much stronger than the backflow observed in case 2 and the flow seems to act almost as a backward facing step in this case. The backflow velocity is approximately 0.1 at y/d=5 (y/h=2.5). This is a smaller value than measured by Piirto et al. (2003) for the backward-facing step flow with a step height of h=10 mm, expansion ratio ER=1.5 and inlet streamwise maximum velocity U_0=1.48 m/s. They measured the backflow velocity at x/h=4 to be 0.2. Apparently the lower inlet streamwise velocity U_0=0.17 m/s, the higher ER=3 and the higher step height h=40 mm in the present experiment

gives a weaker backflow. Also, the axial position where the backflow velocity is measured is different, i.e. y/h=2.5 in the present experiment versus x/h=4 in the measurements of Piirto et al. (2003).

The axial velocity fluctuations (v_{rms}) and the transverse velocity fluctuations (u_{rms}) for case 3 are shown in Figures 3.38 and 3.39, respectively. Normalised peak values of about 0.27 for the axial velocity fluctuations and 0.11 for the transverse velocity fluctuations are observed at y/d=1. Compared to case 1 the axial velocity fluctuation in the shear layer close to inlet B where the velocity is highest is approximately the same. The axial velocity fluctuation in the shear layer close to inlet A is almost quarter of the value in case 1. This corresponds well to the velocity in inlet A for case 3 which is a quarter of the velocity in case 1. The transverse velocity fluctuations close to inlet B is about 0.07 compared to 0.25 for case 1, so the lower velocity in inlet A has obviously a great impact on the transverse velocity fluctuations, and thereby the transverse spreading of concentration.

3.7.2 Reynolds shear stress

Figure 3.40 shows profiles of Reynolds shear stress (<uv>) at three different axial positions for case 3. At y/d=1 the normalised peak value of the shear stress close to inlet B is seen to be -0.013, and close to inlet A 0.002. This is significantly smaller than 0.025, which was measured in case 1, but close to what was measured in case 2.

3.7.3 Mean and fluctuating concentrations

Figure 3.41 shows the mean concentration field in the two overlapping areas in the initial mixing zone for case 3. As in case 1 and 2 there is a re-circulation zone right behind the block, but as already seen from Figure 3.35 the mixing effect is not that strong. The concentration in this zone is about 0.85, this means that the low-velocity flow with concentration 1 is dominating in this area and that the high-velocity flow with concentration 0 is transported away from this area much faster. Different from case 1 there is a recirculation zone formed along the left side of the channel as already observed from Figures 3.34 and 3.36. Here the flow is homogeneously distributed at a concentration of about 0.6, meaning that a great part of the high-velocity flow is retarded around y/d=5.5 and mixes with the low-velocity flow in this area until y/d=0.5.

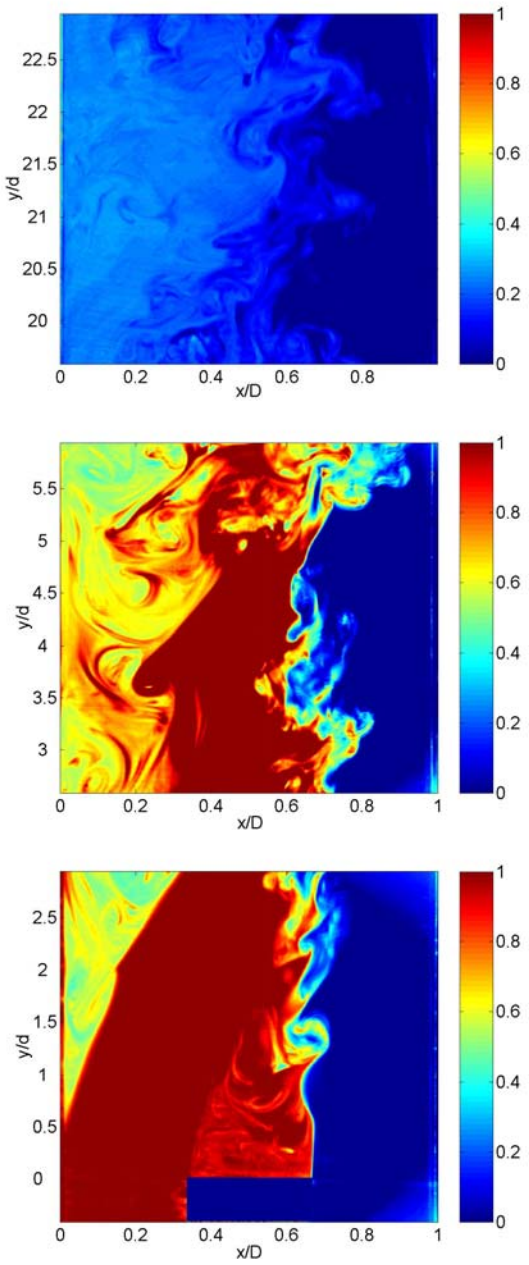

Figure 3.34: Instantaneous concentration fields at the different measurement positions along the channel (case 3).

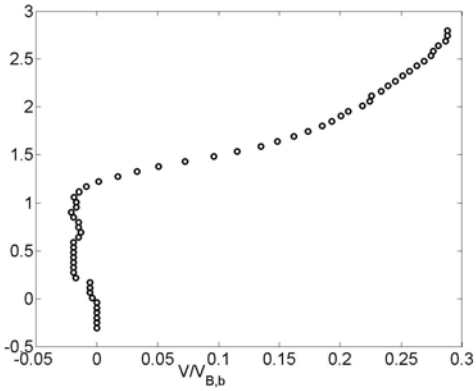

Figure 3.35: Axial velocity (V) along the centreline (case 3).

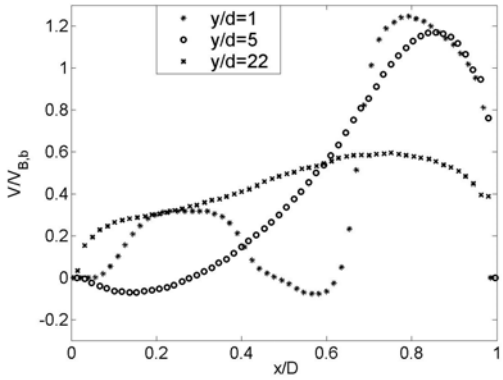

Figure 3.36: Axial velocity (V) at different axial positions (case 3).

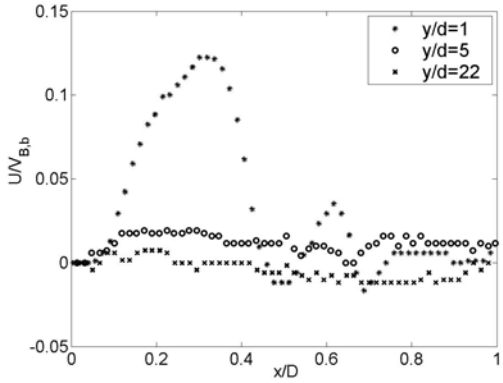

Figure 3.37: Transverse velocity (U) at different axial positions (case 3).

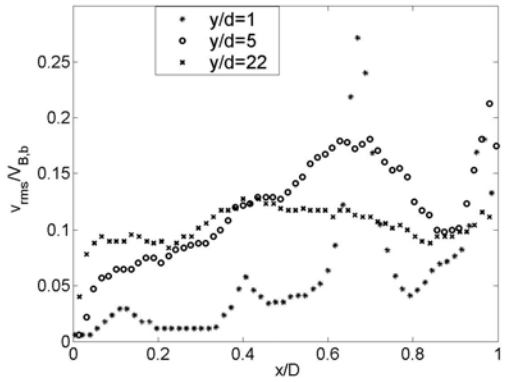

Figure 3.38: Axial velocity fluctuations (v_{rms}) at different axial positions (case 3).

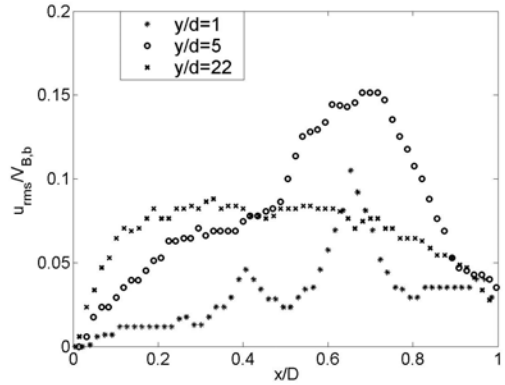

Figure 3.39: Transverse velocity fluctuations (u_{rms}) at different axial positions (case 3).

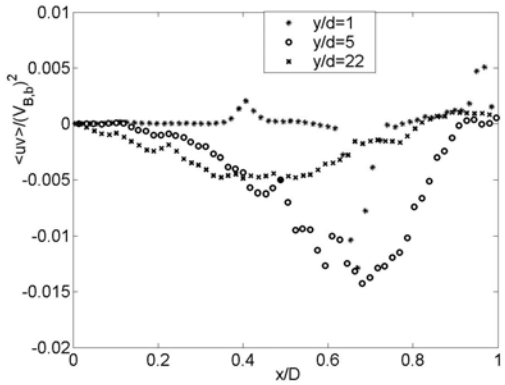

Figure 3.40: Reynolds shear stress (<uv>) at different axial positions (case 3).

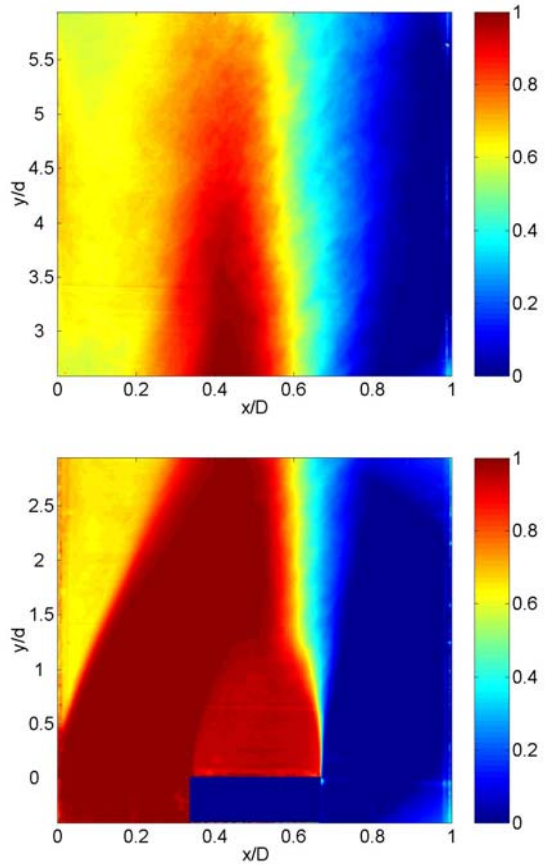

Figure 3.41: Mean concentration in the initial mixing zone (position 1&2, case 3).

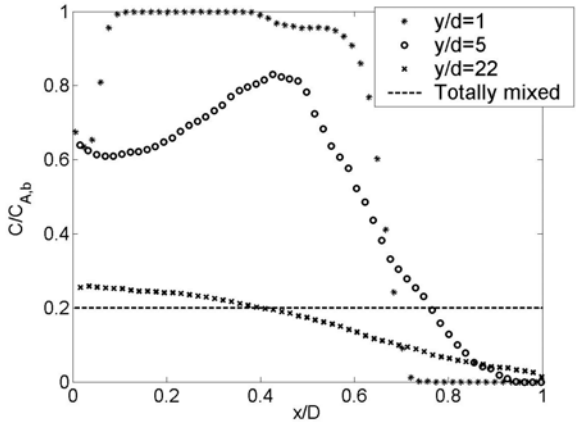

Figure 3.42: Mean concentration (C) at different axial positions (case 3).

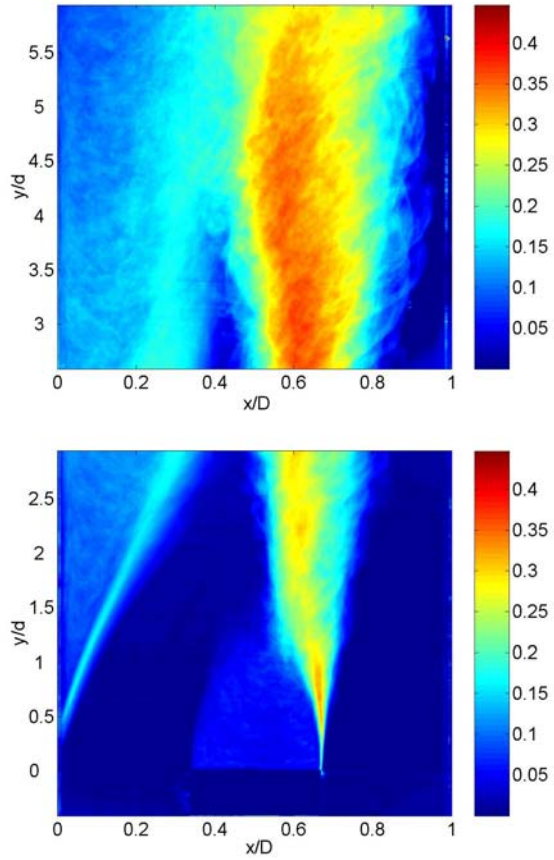

Figure 3.43: Concentration fluctuations in the initial mixing zone (case 3).

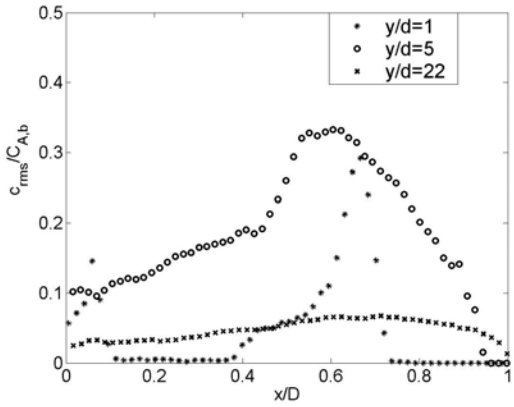

Figure 3.44: Concentration fluctuations (c_{rms}) at different axial positions (case 3).

Figure 3.42 shows the mean concentration (C) profiles at different axial positions. The concentration is seen to become more uniform further out in the channel, but has still not reach the value of 0.2 at y/d=22 that is expected when the two streams are totally mixed in this case.

Figure 3.43 shows the contour plot of the concentration fluctuations in the initial mixing zone. From y/d=2 the fluctuations have a high value along x/D=0.65. There is also a separating shear layer formed along the recirculation zone at the left side of the channel caused by the backflow. Figure 3.44 shows the concentration fluctuations (c_{rms}) at different axial positions. The concentration fluctuations at y/d=1 is highest at x/D=0.65.

3.7.4 Scalar Reynolds fluxes

Figure 3.45 shows a vector plot of the scalar fluxes in the initial mixing zone for case 3. Comparing Figure 3.45 with Figures 3.15 and 3.30 it can be seen that the recirculation behind the block for case 3 is not as strong as for case 1 and 2. Figure 3.46 shows cross-sectional profiles of the scalar fluxes at y/d=5. Compared to case 1, the scalar fluxes seem to have lower values in this case.

Compared with the mean concentration profiles in Figure 3.42, the scalar fluxes are noted to be in the opposite direction of the concentration gradients, indicating that turbulent transport of concentration can be described by the gradient diffusion hypothesis even in this case.

3.7.5 Analysis of degree of mixing

Macro- and micro-mixing

In Figure 3.47, the coefficient of variation CoV and the decay function d are plotted along the channel length. At the last measurement point the coefficient of variation is equal to a value of 0.48. For case 1, CoV=0.15, and for case 2, CoV=0.38, meaning that case 1 and 2 are better macro-mixed than case 3 at this point.

The decay function is estimated to be higher than the coefficient of variation from y/d=8 to y/d=15. This indicates that the flow is better macro-mixed than micro-mixed. As in case 2, at the last measurement point the decay function is smaller than the Coefficient of variation.

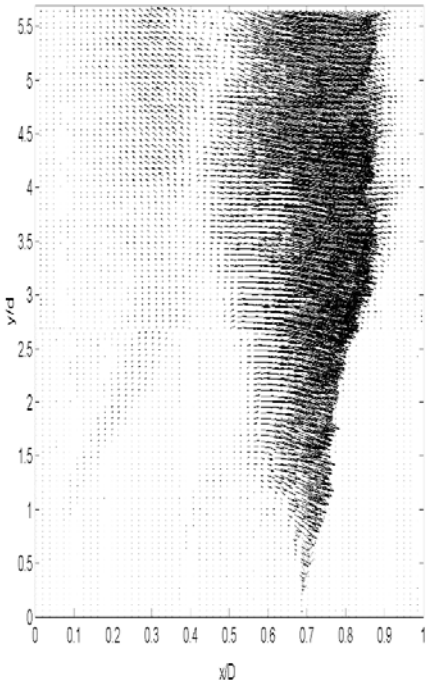

Figure 3.45: Mean scalar Reynolds flux in the initial mixing zone (case 3).

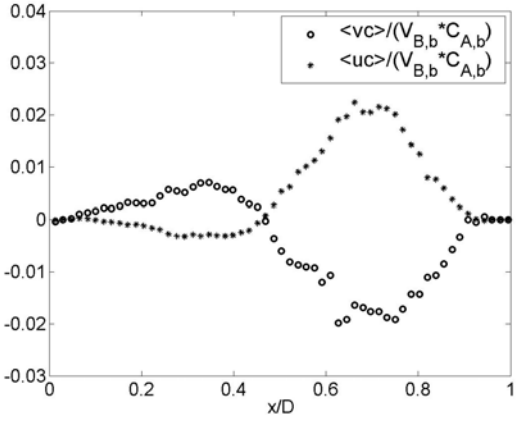

Figure 3.46: Scalar Reynolds fluxes at y/d=5 (case 3).

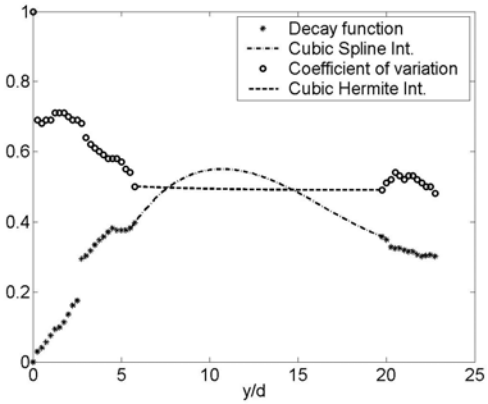

Figure 3.47: Coefficient of Variation (CoV) and decay function (d) (case 3).

Probability density functions (PDF)

Figure 3.48 displays PDF's at different positions in the flow. Comparing with case 1 and 2 it is clear that the flow in case 3 is better mixed along x/D=0.2 than the other two cases. However, the mixing along x/d=0.5 and 0.8 is worse compared to case 1 and 2.

3.8 Concluding remarks

A method for simultaneous measurement of velocity and concentration was successfully applied to measure turbulent mixing in a mixing channel. Three different flow cases were studied. Detailed information about turbulent quantities, such as axial and transverse velocity and concentration fluctuations, Reynolds shear stress and axial and transverse scalar Reynolds flux has been presented.

The measurements for case 1 revealed a backflow (recirculation zone) in the area behind the block and the flow acted as a typical wake flow. The backflow gave an increased mixing effect which resulted in a uniform concentration distribution in this area. Large scale transverse velocity fluctuations were also observed. PDF's at different positions in the flow showed that the concentration was more uniform behind the block than further out in the channel. The degree of macro and micro-mixing along the channel were studied by analysing the Coefficient of Variation and the

decay function. This showed how the mixing developed along the channel and it was found that at the last measurement point in the channel the flow was better macro than micro-mixed.

For case 2 it was found that the mixing in the recirculation zone was not as effective as in case 1. The transverse velocity fluctuations were also less which causes less transverse spreading of concentration. A weak backflow along the left side of the channel was identified and this indicates that there is a transition from a wake flow to a flow behind a backward facing step in this case. For case 2 it was also found that the flow is better micro-mixed than macro-mixed. From the PDF's it can be concluded that compared to case 1 the transverse spreading in case 2 is smaller and there is more spreading towards the inlet with the higher velocity.

The mixing in the recirculation zone for case 3 was found to be even less effective than in case 2. The measurements for case 3 also showed a backflow along the left channel wall that was much stronger than the one identified in case 2. The flow seemed to act almost as a backward facing step. The flow in case 3 seemed to be better macro-mixed than micro-mixed. From the PDF's it is found that the flow in case 3 is better mixed along x/D=0.2 than in the other two cases. However, the mixing along x/D=0.5 and 0.8 is worse compared to case 1 and 2.

These results are of great importance for validation of Computational Fluid Dynamics (CFD) simulations, and will be used for comparison with the results presented in Chapter 7.

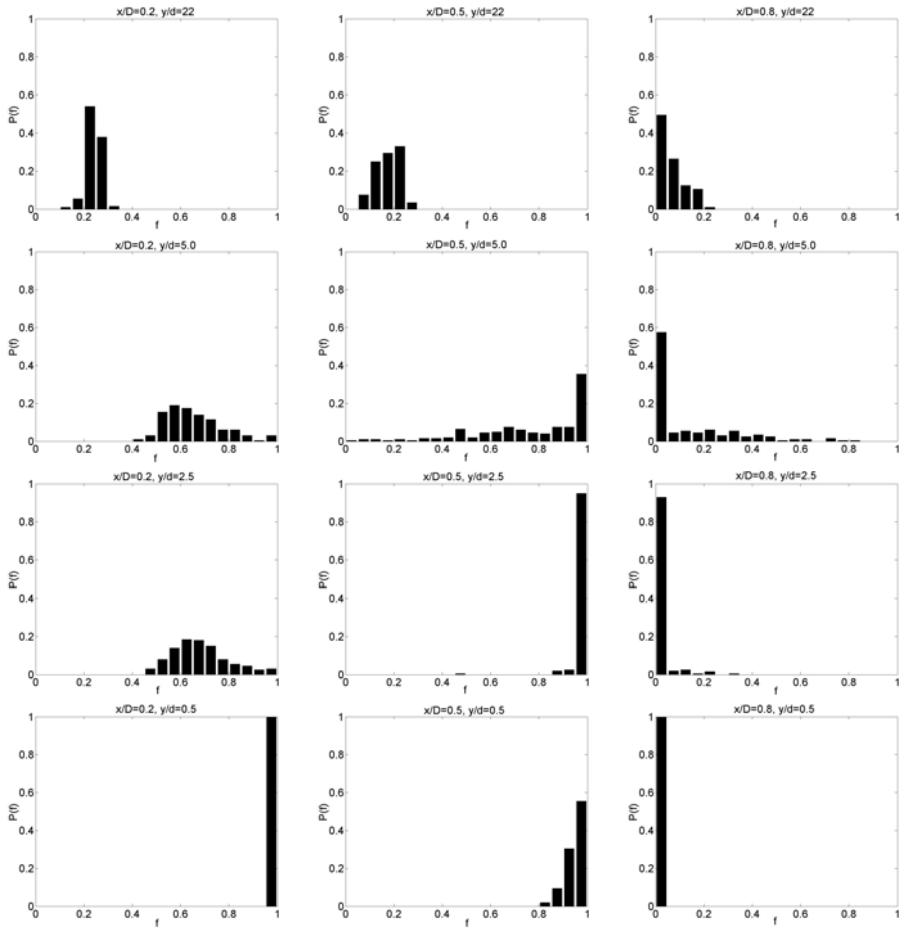

Figure 3.48: Probability density functions at different axial and transverse positions in the channel (case 3).

Chapter 4

Measurement of product concentration

4.1 Introduction

In this chapter experimental data obtained by using a reactive-PLIF technique to measure product concentration from an acid-base reaction will be presented. The method applied in this work is based on the work of Koochesfahani and Dimotakis (1986), Komori et al. (1993) and Neudeck (1998). Sodium Fluorescein was used as the fluorescent dye, Sulfuric Acid and Sodium Hydroxide was used as reactants.

4.2 Testing the dye properties

Preliminary testing of the dye was performed in a small test chamber to get information about the properties of the dye. The test chamber was made of the same material and had the same dimensions as the channel where the actual measurements were performed.

The response of the fluorescent light was monitored with 9 different dye concentrations in water (pH≈7), this was done to ensure linear response to the dye concentration. The correlation is seen from Figure 4.1 to be linear.

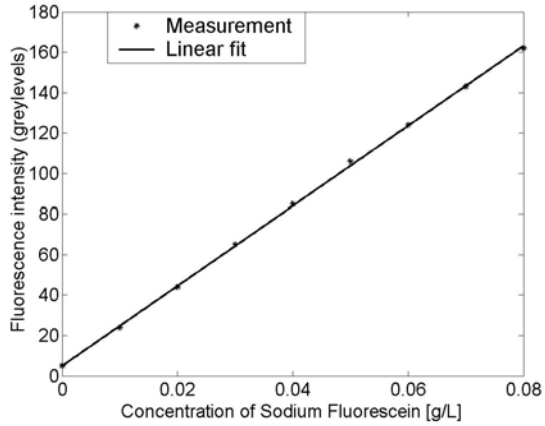

Figure 4.1: Fluorescence intensity versus concentration of Sodium Fluorescein.

Based on the curve in Figure 4.1 the dye concentration used in the actual measurements was chosen to be 0.08 g/L.

4.2.1 Acid-base Titration

An Acid-base titration is when adding a base to an acid until the equivalence point is reached (that is the moles of acid equals the moles of base). For the titration of a strong base and a strong acid this equivalence point is reached when the pH of the solution is 7. For titration of a strong base with a weak acid, the equivalence point is reached when the pH value is greater than 7.

The reactants used in this work are the same as in Komori et al. (1993) and Neudeck (1999). Acetic Acid and Ammonium Hydroxide reacts to form Ammonium Acetate and water i.e.

$$CH_3COOH + NH_4OH \rightarrow CH_3COONH_4 + H_2O \qquad (4.1)$$

This is a rapid irreversible second-order reaction. The reaction rate constant is in the order of 10^8 m^3/mol s and the concentration of the two species is 10 mol/m^3 (0.01 M).

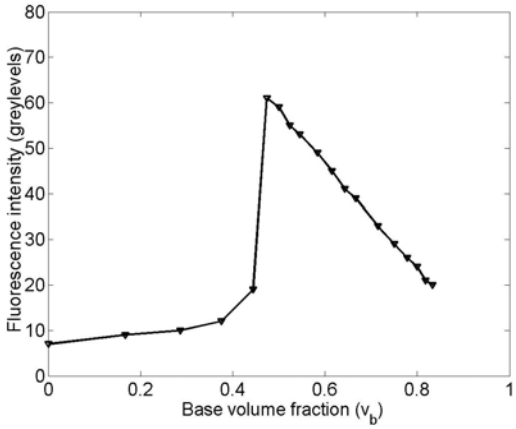

Figure 4.2: Titration of base into an acid+dye solution.

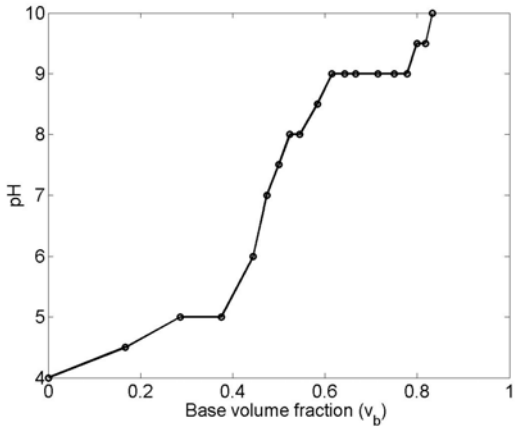

Figure 4.3: pH of the solution during the titration.

Titration experiments with Acetic Acid and Ammonium Hydroxide was performed in the test chamber to get information about the sensitivity of the dye. Titration of base in an acid+dye solution corresponds to the first case described in Chapter 2.4, and this showed a linear response when the base was in excess, as can be seen from Figure 4.2. Figure 4.3 shows the pH of the solution during the titration. At the equivalence point the pH is seen to be between 7 and 8.

From the titration experiments it was decided to use acid+dye and base in the actual measurements, corresponding to the first case described in Chapter 2.4, because this would make the data analysis easier. When base is in excess there are only base and/or product present. A base volume

fraction (v_b) of 0.5 corresponds to maximum product concentration ($C_{p,max}$) and when v_b is 1 there are no product present ($C_{p,0}$). The linear relationship between the fluorescence intensity and v_b can therefore be used directly to measure product concentration, C_p (CH_3COONH_4 + H_2O). It is important to notice that the measured product concentration is conditioned on $v_b \geq 0.5$, this has to be taken account for if the results are to be used for comparison with numerical simulations.

4.3 Experimental details

The reactive-PLIF technique was used for the measurements. Measurements were performed at 6 different positions in the mixing channel described in Chapter 3. Two different flow conditions were considered; case 1 and 2 as described in Chapter 3. 200 images were recorded for each measurement position.

In one of the 250 L feed tanks 2.5 L of 1.0 M Acetic acid was diluted to a concentration of 0.01 M. In addition 1 L of 20 g/L Sodium Fluorescein was added to this tank and gave a dye concentration of 0.08 g/L. This mixture was introduced through channel A (see Figure 3.2). In the other 250 L feed tank 2.5 L of 1.0 M Ammonium Hydroxide was diluted to a concentration of 0.01 M. This mixture was introduced through channel B (see Figure 3.2).

The remaining parameters are the same as used for the passive mixing experiment described in Chapter 3.

4.4 Data analysis

Before recording the actual measurements a series of 20 background images with base in the test chamber was taken. The mean background emission was found as the ensemble average of these 20 images and this was used to set the zero value for the cameras response on variation in dye concentration. Similarly, 20 reference images were taken with maximum dye concentration uniformly distributed in the test chamber. Maximum dye concentration was found by making a 50/50 solution of Acid+dye and base. This corresponds to the grey-level of maximum

product concentration. The actual concentration images were normalised according to Equation (2.4).

Since the response of the fluorescent light is only linear when the base is in excess, the data analysis can only be applied to the part of the channel where the base enters, i.e. base can be assumed to be in excess. The analysis is therefore performed only on half of the channel diameter.

4.5 Results for case 1, velocity ratio 1:1

Figure 4.4 shows instantaneous images of the product concentration from the reactive-PLIF measurements at different positions along the channel for case 1. As can be seen an increased amount of product is formed right behind the block.

Figure 4.5 shows the mean product concentration along the centreline. The product concentration has a maximum at y/d=0.5 within the recirculation region attached to the block and a minimum at y/d=2.5 just downstream of the recirculation region. Further downstream, the product concentration increases steadily along the channel length.

Figure 4.6 shows profiles of the mean product concentration at different axial positions. In the first measured profile downstream of the block at y/d=0.5, high values of mean product concentration are found due to the increased mixing effect of the recirculating flow. Similar levels of mean product concentration are also found at the end of the mixing channel. This corresponds well with what was found in the pure mixing experiments described in Chapter 3.

Figure 4.7 shows profiles of the product concentration fluctuations. As expected the fluctuations are noted to be highest where the highest concentration gradients are found.

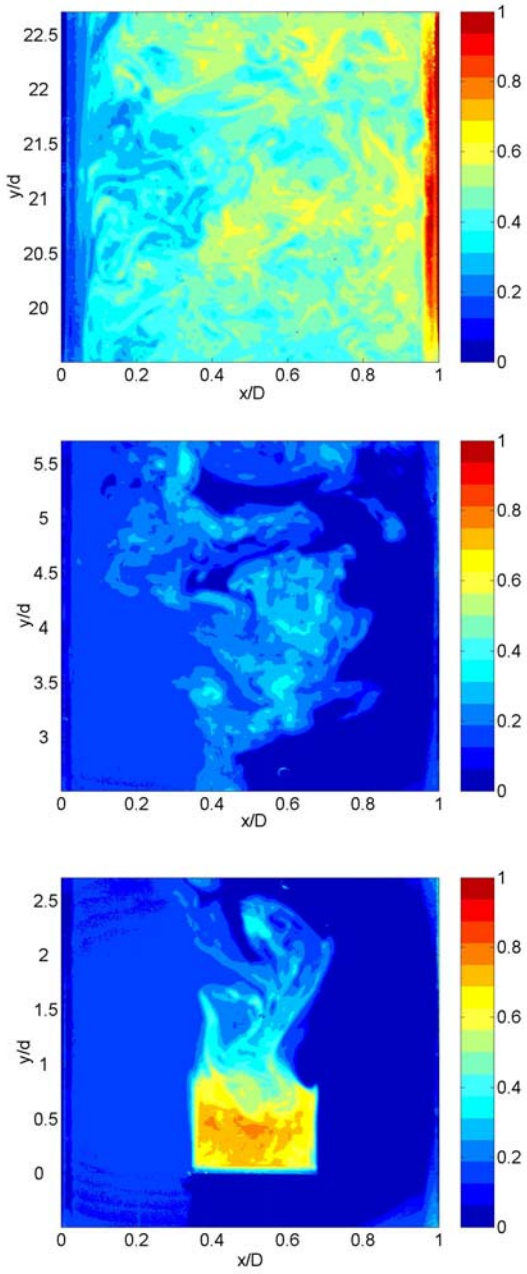

Figure 4.4: Instantaneous product concentration at different measurement positions along the channel for case 1.

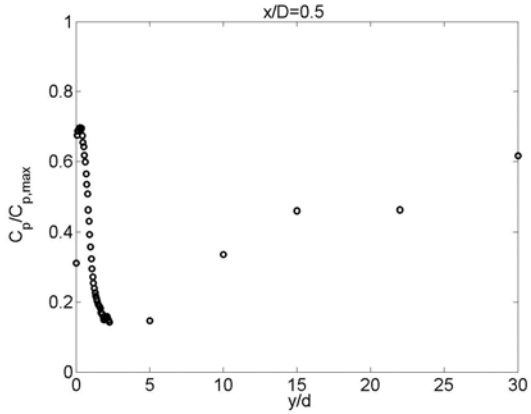

Figure 4.5: Mean product concentration along the centreline for case 1.

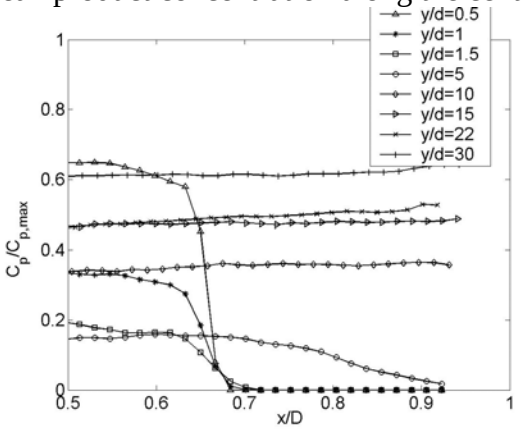

Figure 4.6: Mean product concentration profiles at different axial positions for case 1.

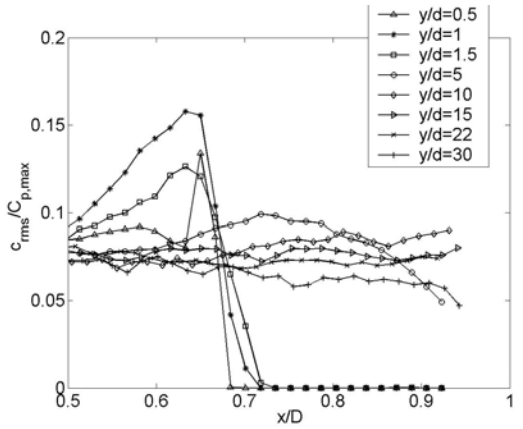

Figure 4.7: Product concentration fluctuation profiles at different axial positions for case 1.

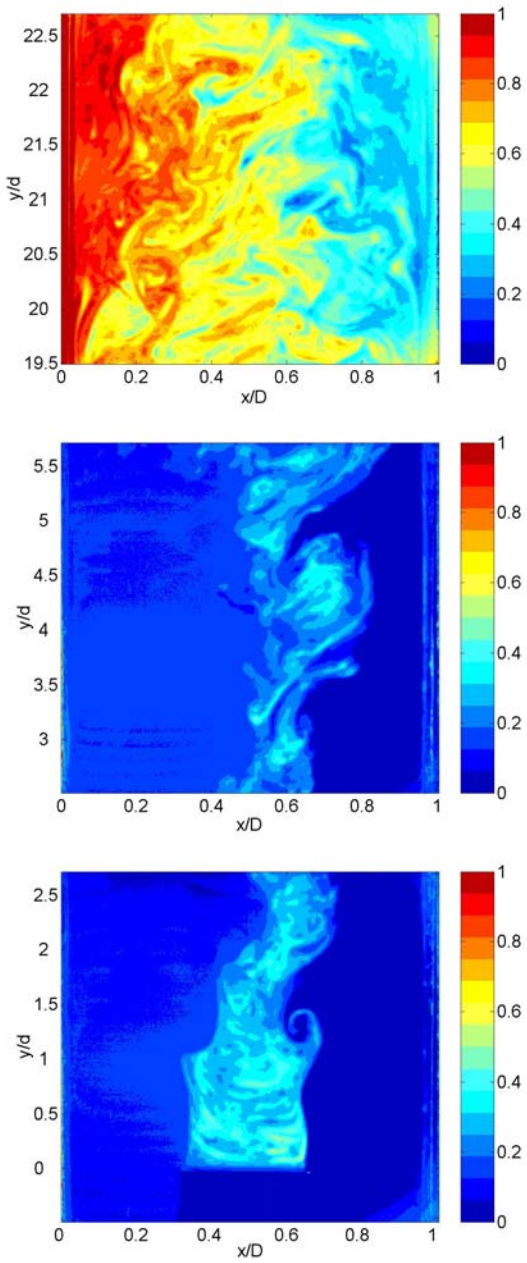

Figure 4.8: Instantaneous product concentration at different measurement positions along the channel for case 2.

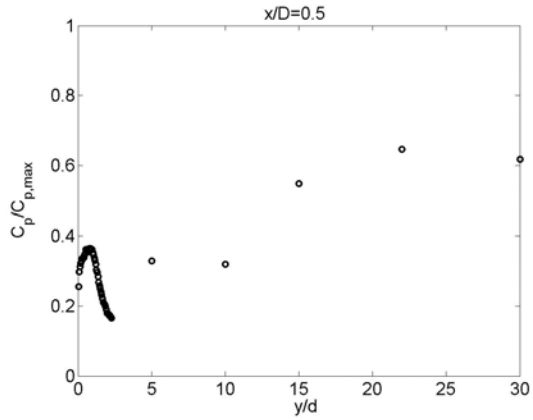

Figure 4.9: Mean product concentration along the centreline for case 2.

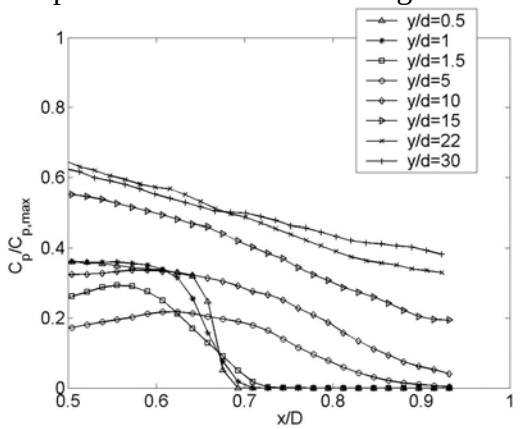

Figure 4.10: Mean product concentration profiles at different axial positions for case 2.

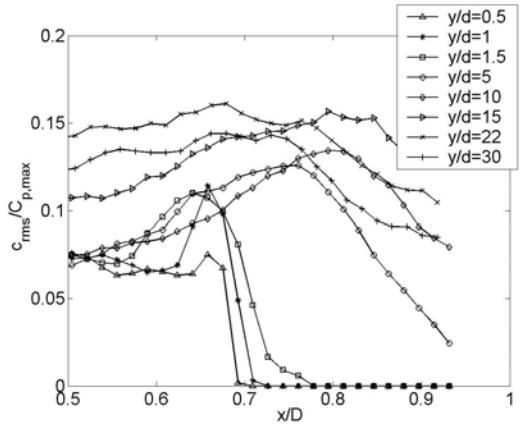

Figure 4.11: Product concentration fluctuation profiles at different axial positions for case 2.

4.6 Results for case 2, velocity ratio 0.5:1

Figure 4.8 shows instantaneous images of the product concentration from the reactive-PLIF measurements at different positions along the channel for case 2. The amount of product formed right behind the block is noted to be less than for case 1.

The mean product concentration along the centreline shown in Figure 4.9 exhibits the same trend as for case 1. However, the peak value within the recirculation region attached to the block is smaller.

Profiles of the mean and fluctuating product concentration at different axial positions are shown in Figure 4.10 and Figure 4.11, respectively. Again the profiles exhibit much the same trend as for case 1. However, the profiles at the end of the channel are not so uniform across the channel.

4.7 Concluding remarks

A reactive-PLIF method was successfully applied to measure product concentration from an acid-base reaction in a mixing channel. Two different flow cases were studied. Information about instantaneous, mean and fluctuating product concentration has been presented.

The measurements revealed that an increased amount of product is formed in the recirculation zone that was identified from the mixing experiments presented in Chapter 3. It is also shown that the amount of product formed depends on how well the two streams are mixed. This corresponds well with the fact that the reactants have to be mixed on a molecular level before the reaction occurs.

These results are of great importance for validation of Computational Fluid Dynamics (CFD) simulations, and will be used for comparison with the results presented in Chapter 8.

Part II

Numerical simulations

Chapter 5

Numerical models

5.1 Introduction

In this chapter, the governing equations used in the numerical simulations will be presented. The standard k-ε turbulence model is presented and the RNG and Chen-Kim variant of the k-ε model are also presented. Different models for describing mixing and chemical reactions in turbulent flows are also described. The models considered are the Eddy Dissipation Concept (EDC) and modifications of this model, presumed PDF models such as the double peak PDF model, the beta-PDF model and the multi-peak presumed PDF model and finally the multiple timescale turbulent mixer model.

5.2 Governing equations

Turbulent flows of incompressible Newtonian fluids are governed by the Reynolds Averaged Navier-Stokes (RANS) equations. The continuity and the momentum equations for the mean flow may be written in Cartesian tensor notations as

$$\frac{\partial U_j}{\partial x_j} = 0 \tag{5.1}$$

$$\frac{\partial}{\partial t}(\rho U_i) + \frac{\partial}{\partial x_j}(\rho U_j U_i) = -\frac{\partial P}{\partial x_i} + \frac{\partial \tau_{ij}}{\partial x_j} \tag{5.2}$$

Here, U_i is the mean velocity in x_i-direction, P is the mean pressure and ρ is the density. The Reynolds stresses $\tau_{ij} = -\rho\overline{u_i u_j}$, resulting from the averaging procedure of the non-linear convective terms in the momentum equations, represent the effects of the turbulence on the mean flow.

The transport of a passive scalar ϕ in a turbulent flow is governed by a convection-diffusion equation of the form

$$\frac{\partial}{\partial t}(\rho\phi) + \frac{\partial}{\partial x_j}(\rho U_j \phi) = -\frac{\partial J_{\phi_j}}{\partial x_j} \tag{5.3}$$

where the turbulent scalar fluxes $J_{\phi_j} = \rho\overline{u_j \phi'}$ again results from the averaging procedure of the non-linear convective terms in the passive scalar equation.

The presence of turbulent stresses and scalar fluxes leads to an unclosed system of equations. A turbulence model, that is additional equations for these terms, must therefore be provided.

5.3 Turbulence models

The effects of the turbulence on the mean flow are modelled by a so-called eddy viscosity model. Accordingly, the Reynolds stresses are modelled in analogy with laminar stresses using the Boussinesq approximation as

$$\tau_{ij} = -\rho\overline{u_i u_j} = 2\mu_T S_{ij} - \frac{2}{3}\delta_{ij}\rho k \tag{5.4}$$

where the mean rate-of-strain tensor is given by

$$S_{ij} = \frac{1}{2}\left(\frac{\partial U_i}{\partial x_j} + \frac{\partial U_j}{\partial x_i}\right) \tag{5.5}$$

Likewise, the turbulent scalar fluxes are modelled using the gradient-diffusion hypothesis as

$$J_{\phi_j} = \rho \overline{u_j \phi'} = -\Gamma_\phi \frac{\partial \phi}{\partial x_j} \tag{5.6}$$

The turbulent viscosity μ_T can be found from dimensional argument to be described by a velocity scale and a length scale characterising the turbulence. Adopting a k-ε turbulence model, which belongs to the class of two-equation models, the two scales can be defined by the turbulent kinetic energy k and its dissipation rate ε. The turbulent viscosity is then given by

$$\mu_T = C_\mu \rho \frac{k^2}{\varepsilon} \tag{5.7}$$

The turbulent transport coefficient or diffusivity Γ_ϕ is related to the turbulent viscosity μ_T by the turbulent Prandtl / Schmidt number σ_ϕ as

$$\Gamma_\phi = \frac{\mu_T}{\sigma_\phi} \tag{5.8}$$

5.3.1 Standard k-ε model

The transport equations for the turbulent kinetic energy k and its dissipation rate ε for the standard k-ε model may be written as

$$\frac{\partial}{\partial t}(\rho k) + \frac{\partial}{\partial x_j}(\rho U_j k) = \frac{\partial}{\partial x_j}(\Gamma_k \frac{\partial k}{\partial x_j}) + P_k - \rho \varepsilon \tag{5.9}$$

$$\frac{\partial}{\partial t}(\rho \varepsilon) + \frac{\partial}{\partial x_j}(\rho U_j \varepsilon) = \frac{\partial}{\partial x_j}(\Gamma_\varepsilon \frac{\partial \varepsilon}{\partial x_j}) + C_1 \frac{\varepsilon}{k} P_k - C_2 \rho \frac{\varepsilon^2}{k} \tag{5.10}$$

Here, the production of turbulent kinetic energy P_k is expressed by

$$P_k = \tau_{ij} \frac{\partial U_i}{\partial x_j} = \mu_T S^2 \tag{5.11}$$

where the mean strain rate S is given by

$$S = \sqrt{2 S_{ij} S_{ij}} \tag{5.12}$$

The modeling constants $C_{\mu},,C_1,C_2,\sigma_k$ and σ_ε are given in Table 5.1.

The standard k-ε model makes use of a single time scale, $\tau_d = k/\varepsilon$, called dissipation range timescale. Since turbulence consists of fluctuating motions with a spectrum of timescales, a single timescale approach seems unlikely to be sufficient under all circumstances. The model is also well-known to perform less satisfactorily in many flow situations such as separated flows, flows with streamline curvature, swirling flows and compressible flows. Modifications of the standard k-ε model have been proposed and among the most well-known ones are the RNG and the Chen-Kim k-ε models. (Schmalzriedt et al., 2003)

5.3.2 RNG k-ε model

A popular alternative to the standard k-ε model is the so-called RNG k-ε model (Versteeg and Malalasekera, 1996). The renormalisation group theory (RNG) has been used to obtain the k-ε equations from the Navier-Stokes equations. In the RNG k-ε model there is also an additional term in the ε-equation, which is an ad hoc model, not derived from RNG theory. The transport equation for the dissipation of turbulent kinetic energy may then be written as

$$\frac{\partial}{\partial t}(\rho \varepsilon) + \frac{\partial}{\partial x_j}(\rho U_j \varepsilon) = \frac{\partial}{\partial x_j}(\Gamma_\varepsilon \frac{\partial \varepsilon}{\partial x_j}) + C_1 \left(1 - C_1^* \frac{\eta\left(1 - \eta/\eta_0\right)}{1 + \beta \eta^3} \right) \frac{\varepsilon}{k} P_k - C_2 \rho \frac{\varepsilon^2}{k} \tag{5.13}$$

where $\eta = S\tau_d$ is a timescale ratio between the turbulence and the mean flow. The modelling constants take the values $C_1^* = 1/C_1$, $\eta_0 = 4.377$ and $\beta = 0.012$. The remaining constants determined by the RNG analysis are given in Table 5.1.

5.3.3 Chen-Kim k-ε model

The Chen- Kim k-ε model (Schmalzriedt et al., 2003) attempts to improve the dynamical response of the ε equation by introducing an additional timescale related to the mean flow

$$\tau_{P_k} = \frac{\rho k}{P_k} = \frac{\tau_d}{C_\mu \eta^2} \tag{5.14}$$

which is called the production-range timescale. The transport equation for the dissipation of turbulent kinetic energy may then be written as

$$\frac{\partial}{\partial t}(\rho \varepsilon) + \frac{\partial}{\partial x_j}(\rho U_j \varepsilon) = \frac{\partial}{\partial x_j}(\Gamma_\varepsilon \frac{\partial \varepsilon}{\partial x_j}) + C_1 \left(1 + C_1^* \eta^2\right) \frac{\varepsilon}{k} P_k - C_2 \rho \frac{\varepsilon^2}{k} \tag{5.15}$$

where $C_1^* = (C_\mu \cdot C_3)/C_1$ and $C_3 = 0.25$ are additional modelling constants. The remaining modelling constants are given in Table 5.1.

Table 5.1: k-ε turbulence model constants.

Models	C_μ	C_1	C_2	σ_k	σ_ε
Standard	0.0900	1.44	1.92	1.0	1.3
RNG	0.0845	1.42	1.68	0.72	0.72
Chen-Kim	0.0900	1.15	1.90	0.75	1.15

5.4 Models for micro-mixing and chemical reactions

5.4.1 The Eddy Dissipation Concept

Standard EDC model

The EDC model was developed for combustion reactions. These reactions can often be treated as single-step irreversible reactions with finite reaction rates (Magnussen and Hjertager, 1976), i.e.

$$1 \text{ kg A} + s \text{ kg B} \rightarrow (1+s) \text{ kg C} \tag{5.16}$$

Here s is the stoichiometric mass requirement of species B to consume 1 kg of species A.

This simple reaction scheme results in mixture composition being determined by solving for only two variables, the mass fraction of species A, Y_A, and the mixture fraction, ξ. According to Equation (5.16)

$$\frac{\partial}{\partial t}(\rho \cdot Y_A) + \frac{\partial}{\partial x_j}(\rho \cdot U_j \cdot Y_A) = \frac{\partial}{\partial x_j}\left[\frac{\mu_T}{Sc_T} \cdot \frac{\partial Y_A}{\partial x_j}\right] + R_A \tag{5.17}$$

$$\frac{\partial}{\partial t}(\rho \cdot \xi) + \frac{\partial}{\partial x_j}(\rho \cdot U_j \cdot \xi) = \frac{\partial}{\partial x_j}\left[\frac{\mu_T}{Sc_T} \cdot \frac{\partial \xi}{\partial x_j}\right] \tag{5.18}$$

where R_A is the time-averaged reaction rate and Sc_T is the turbulent Schmidt number. The basis for this to be valid is that the turbulent Schmidt numbers are equal for all species, an approximation, which is often found to be valid in turbulent flows. The mixture fraction is defined as

$$\xi = \frac{\beta - \beta_\infty}{\beta_0 - \beta_\infty} \tag{5.19}$$

where β is a conserved combined variable of, for example, mass fraction of component A, Y_A, and mass fraction of component B, Y_B, expressed as

$$\beta = Y_A - \frac{Y_B}{s} \tag{5.20}$$

β_∞ is the value of β at a B rich inlet and β_0 is the value at an A rich inlet.

The reaction rate of species A in Equation (5.17) is taken to be the smallest of the turbulent dissipation rates of species A, B and C

$$R_A = -A \cdot \rho \cdot \frac{\varepsilon}{k} \cdot \min\left(Y_A, \frac{Y_B}{s}, B \cdot \frac{Y_C}{1+s}\right) \tag{5.21}$$

The constants A and B in Equation (5.21) are taken to be 4 and 0.5, respectively, for gaseous combustion reactions (Magnussen and Hjertager, 1976).

5.4.2 Scalar mixing/dissipation theory (SDT)

Since the EDC-model is strictly valid only for Sc~1, an algebraic expression for the scalar dissipation timescale could be used to include effects of higher Sc-numbers (Sc>>1). From Fox (1996), the scalar dissipation rate can be expressed as

$$\frac{\varepsilon_\phi}{\left\langle \phi'^2 \right\rangle} = \frac{2 + Sc^{-1}}{2}\left[\frac{1}{2}\frac{k}{\varepsilon} + \frac{1}{2}\ln(Sc)\left(\frac{\nu}{\varepsilon}\right)^{1/2}\right]^{-1} \tag{5.22}$$

Here ε_ϕ is the dissipation rate of a scalar variable ϕ and $<\phi'^2>$ is the variance of the scalar variable.

The EDC-model for infinitely fast reaction assumes that the reaction is limited by micro-mixing. For gases (Sc~1) this mixing rate is said to be proportional to the dissipation rate of turbulent kinetic energy. However, for liquid reactions (Sc>>1), the mixing rate must be related to dissipation of scalar variables. One alternative is to replace the timescale of fluid dynamic dissipation (k/ε) with the time scale of scalar dissipation ($<\phi'^2>/\varepsilon_\phi$). If we use the expression in Equation (5.22), we get the modified time-averaged reaction rate for chemical species A (EDC-SDT) as

$$R_A = -A \cdot \rho \cdot \left(\frac{\varepsilon_\phi}{<\phi'^2>}\right) \cdot \min\left(Y_A, \frac{Y_B}{s}\right) \tag{5.23}$$

In the standard EDC-model, the dissipation of the product C is also included, this is because combustion reactions are strongly exothermic reactions. For liquid reactions, which are isothermal, the dissipation of the product C does not have to be considered.

The above mentioned scalar time scale is valid for a fully developed turbulent structure. It has been found that the development in liquid mixtures takes longer time. The multiple time scale turbulent mixer model of Baldyga (1989) takes account of these processes.

5.4.3 Multiple-time-scale turbulent mixer model (MTS)

To calculate distributions of mixture fraction (ξ) variances characterising the intertial-convective, σ_1^2, the viscous-convective, σ_2^2 and the viscous-diffusive σ_3^2 sub-ranges of the turbulent spectrum, the turbulent mixer model can be used. The model interprets the mixing process as the process of convection, dispersion and dissipation of the concentration variance (Baldyga et al., 2001)

$$\sigma_S^2 = \sigma_1^2 + \sigma_2^2 + \sigma_3^2 \tag{5.24}$$

Figure 5.1 shows the spectrum of concentration variance in liquids, displaying the three subranges.

Inertial convective (σ_1^2)
The inertial convective variance is produced from the macroscopic inhomogeneity of the mixture fraction as a result of velocity fluctuations and determined from the transport equation (Baldyga, 1989)

$$\frac{\partial}{\partial t}\left(\rho\sigma_1^2\right)+\frac{\partial}{\partial x_j}\left(\rho U_j\sigma_1^2\right)=\frac{\partial}{\partial x_j}\left[\Gamma_T\frac{\partial\sigma_1^2}{\partial x_j}\right]+2\,\Gamma_T\left(\frac{\partial\xi}{\partial x_j}\right)^2-\sigma_1^2 R\rho\frac{\varepsilon}{k} \tag{5.25}$$

Here, R is the ratio of the timescale for the decay of the velocity fluctuations to the time scale for the decay of the concentration fluctuations, taken to have a numerical value of 2.0.

The dissipation of large eddies causes smaller concentration fluctuations, thus the sink term of the inertial-convective range is equal to the source term of the viscous-convective range. (Kruis and Falk, 1996)

Viscous-convective (σ_2^2)
The dissipation in the viscous-convective range is the engulfment of surrounding fluid by vortex movement (Kruis and Falk, 1996). The viscous-convective variance is calculated from the transport equation (Baldyga, 1989)

$$\frac{\partial}{\partial t}\left(\rho\sigma_2^2\right)+\frac{\partial}{\partial x_j}\left(\rho U_j\sigma_2^2\right)=\frac{\partial}{\partial x_j}\left[\Gamma_T\frac{\partial\sigma_2^2}{\partial x_j}\right]+\sigma_1^2R\rho\frac{\varepsilon}{k}-\rho E\sigma_2^2 \quad (5.26)$$

where, the engulfment parameter, E, is given by

$$E=0.058\left(\frac{\varepsilon}{\nu}\right)^{1/2} \quad (5.27)$$

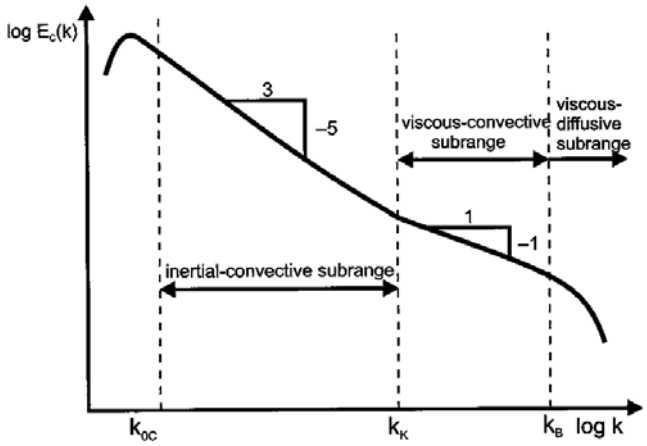

Figure 5.1: Spectrum of concentration variance in liquids. From (Baldyga and Bourne, 1999).

Viscous-diffusive (σ_3^2)
Decreasing the scale of segregation by viscous deformation increases the wave numbers and brings the variance into the viscous-diffusive sub-range of the concentration spectrum. Here, mixing on the molecular scale occurs by molecular diffusion in deforming slabs (Baldyga, 1989).

By the vorticity, lamellar structures are formed which dissipate the concentration fluctuation by molecular mixing. (Kruis and Falk, 1996) The molecular diffusion parameter is defined by

$$G\approx\left(0.303+17050/Sc\right)\cdot E \quad (5.28)$$

The viscous-diffusive variance is determined from the transport equation (Baldyga, 1989)

$$\frac{\partial}{\partial t}\left(\rho\sigma_3^2\right)+\frac{\partial}{\partial x_j}\left(\rho U_j\sigma_3^2\right)=\frac{\partial}{\partial x_j}\left[\Gamma_T\frac{\partial\sigma_3^2}{\partial x_j}\right]+\rho E\sigma_2^2-\rho G\sigma_3^2 \qquad (5.29)$$

After summing up Equations (5.25), (5.26) and (5.29) the evolution of the complete variance (σ_s^2) becomes (Baldyga, 1989)

$$\frac{\partial}{\partial t}\left(\rho\sigma_s^2\right)+\frac{\partial}{\partial x_j}\left(\rho U_j\sigma_s^2\right)=\frac{\partial}{\partial x_j}\left[\Gamma_T\frac{\partial\sigma_S^2}{\partial x_j}\right]+2\,\Gamma_T\left(\frac{\partial\xi}{\partial x_j}\right)^2-\rho\,G\sigma_3^2 \qquad (5.30)$$

Another alternative for the time-averaged reaction rate is to take account of the Multiple-time-scale turbulent mixer model given by Baldyga (1989) and described above. Since for infinitely fast reactions the reaction is limited by the micro-mixing rate ($\rho G\sigma_3^2$), the modified form of the EDC-model (EDC-MTS) will be expressed as

$$R_A=-A\cdot\rho\cdot G\cdot\sigma_3^2\cdot\min\left(Y_A,\frac{Y_B}{s}\right) \qquad (5.31)$$

5.5 Presumed PDF methods

Presumed PDF methods describe the passive scalar concentration distribution by probability density functions. The concentration may be expressed by the mixture fraction, ξ (Baldyga, 1999). Transport equations are solved for the time-averaged of the square of the concentration fluctuations, σ_S^2. From the calculated values of that quantity, and assumptions regarding the shape of the instantaneous concentration-time history, a hypothetical distribution of the instantaneous concentrations with time is derived (Serag-El-Din, 1977). Three versions of the presumed PDF will be described, namely the double peak PDF, the beta PDF and the multi-peak presumed PDF model.

5.5.1 Double peak PDF

The instantaneous concentrations at a point are assumed to follow "battlement shaped time variation" between its maximum and minimum values, i.e. $\hat{\xi}_{\max} \geq \hat{\xi} \geq \hat{\xi}_{\min}$ (Serag-El-Din, 1977). Three different situations may be identified:

1. Figure 5.2 shows the distribution of the instantaneous concentrations when $\sigma_S \langle \left(\hat{\xi}_{\max} - \xi\right)$ and $\sigma_S \langle \left(\xi - \hat{\xi}_{\min}\right)$.
2. Figure 5.3 shows the distribution of the instantaneous concentrations when $\sigma_S \rangle \left(\hat{\xi}_{\max} - \xi\right)$.
3. Figure 5.4 shows the distribution when $\sigma_S \rangle \left(\xi - \hat{\xi}_{\min}\right)$.

Based on the above relation the time averaged of the mass fraction may be calculated by the following expression

$$Y_A = \alpha \cdot Y_A(\xi_+) + (1-\alpha) \cdot Y_A(\xi_-) \tag{5.32}$$

$$\alpha = 0.5 \qquad \xi_+ = \xi + \sigma_S \qquad \xi_- = \xi - \sigma_S$$

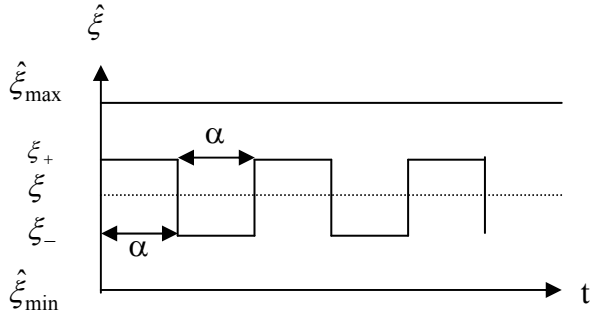

Figure 5.2: Distribution of the instantaneous concentration for $\sigma_S \langle \left(\hat{\xi}_{\max} - \xi\right)$ and $\sigma_S \langle \left(\xi - \hat{\xi}_{\min}\right)$.

$$\alpha = \frac{\xi - \xi_-}{\hat{\xi}_{\max} - \xi_-} \qquad \xi_+ = \hat{\xi}_{\max} \qquad \xi_- = \xi - \frac{\sigma_S^2}{\left(\hat{\xi}_{\max} - \xi\right)}$$

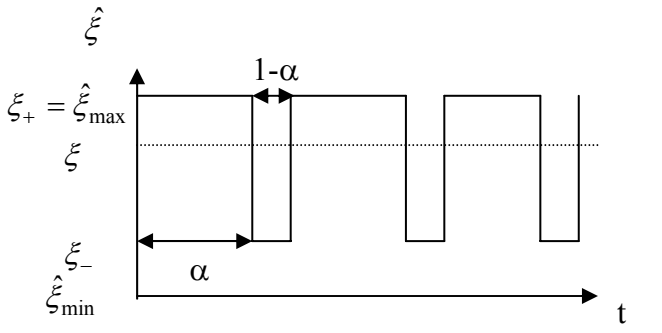

Figure 5.3: Distribution of the instantaneous concentration for $\sigma_S \rangle \left(\hat{\xi}_{\max} - \xi\right)$.

$$\alpha = \frac{\xi - \hat{\xi}_{\min}}{\xi_+ - \hat{\xi}_{\min}} \qquad \xi_+ = \xi + \frac{\sigma_S^2}{\left(\xi - \hat{\xi}_{\min}\right)} \qquad \xi_- = \hat{\xi}_{\min}$$

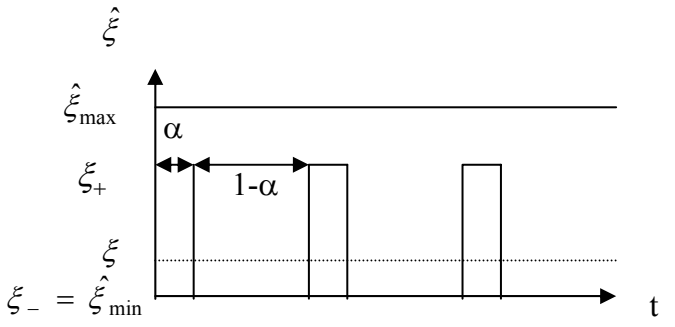

Figure 5.4: Distribution of the instantaneous concentration for $\sigma_S \rangle \left(\xi - \hat{\xi}_{\min}\right)$.

5.5.2 Beta PDF

The beta function written as a PDF has the following form (Li and Toor, 1986)

$$\phi(\hat{\xi}) = \frac{\hat{\xi}^{v-1}\left(1-\hat{\xi}\right)^{w-1}}{B(v,w)} \tag{5.33}$$

Here *B(v, w)* represents the integral

$$B(v,w) = \int_0^1 x^{v-1}(1-x)^{w-1}\,dx \tag{5.34}$$

The variables *v* and *w* are related to the mixture fraction ξ and its variance σ_s^2 by

$$v = \xi\left[\frac{\xi(1-\xi)}{\sigma_S^2} - 1\right] = \xi\frac{1-I_s}{I_s} \tag{5.35}$$

$$w = (1-\xi)\left[\frac{\xi(1-\xi)}{\sigma_S^2} - 1\right] = (1-\xi)\frac{1-I_s}{I_s} \tag{5.36}$$

The intensity of segregation, I_s, is related to the concentration variance σ_s^2 by

$$I_S = \frac{\sigma_s^2}{\xi(1-\xi)} \tag{5.37}$$

Based on the above relation the time averaged of the mass fraction may be calculated by the following expression

$$Y_A = \int_0^1 \hat{Y}_A\left(\hat{\xi}\right)\phi\left(\hat{\xi}\right)d\hat{\xi} \tag{5.38}$$

In Figure 5.5 typical shapes of the beta distribution are shown.

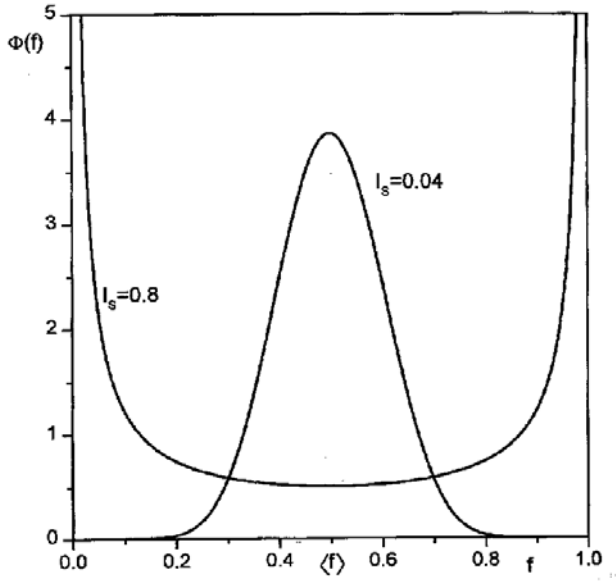

Figure 5.5: Probability density function for mixture fraction: the beta distribution. From (Baldyga and Bourne, 1999).

5.5.3 Multi-peak presumed PDF model

The multi-peak presumed PDF model proposed by Fox (1998) represents the PDF by a finite set of delta functions. In this approach each control volume in the computational domain is divided into a finite number of homogeneous environments. Each environment corresponds to a discretization of the composition PDF in a finite set of delta functions as

$$f_\phi(\psi;x,t) \equiv \sum_{n=1}^{Ne} p_n(x,t)\cdot\delta\left(\psi - \langle\phi\rangle_n(x,t)\right) \tag{5.39}$$

where $p_n(x,t)$ is the probability of environment n, $<\phi>_n(x,t)$ is the value of scalar ϕ corresponding to environment n, N_e is the total number of environments. (Marchisio et al., 2001)

The exchange of material between the environments allows the inlet streams to contact each other. Figure 5.6 gives an illustration of the present model with five environments or peaks (Fox, 2000). Environment

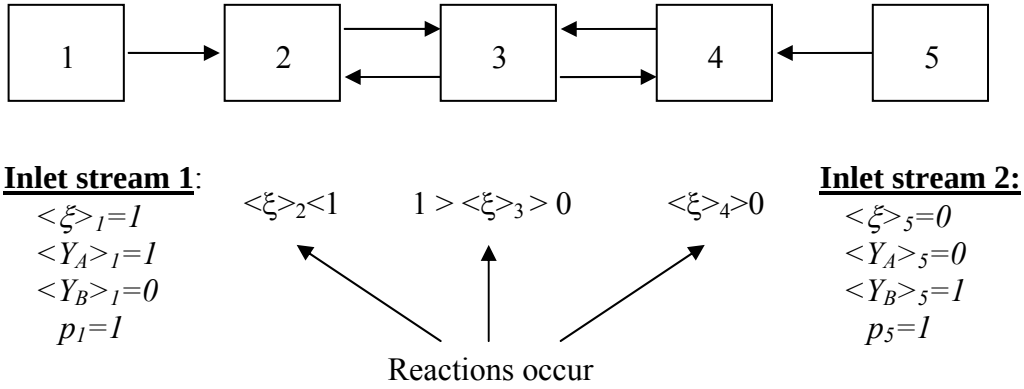

Figure 5.6: Illustration of the multi-peak model with 5 environments.

n is described by the local scalar variable $\langle\phi\rangle_n$, the local volume fraction p_n and the local volume-weighted scalar variable $\langle s_\phi\rangle_n = p_n\langle\phi\rangle_n$, where ϕ is the mixture fraction or concentration of species A or B, i.e. $\phi = \xi$, Y_A, Y_B.

The Reynolds-averaged transport equation for the volume fractions may be written as

$$\frac{\partial p_n}{\partial t} + U_j \frac{\partial p_n}{\partial x_j} = \frac{\partial}{\partial x_j}\left(\Gamma_T \frac{\partial p_n}{\partial x_j}\right) + G_n(p) \tag{5.40}$$

The probability exchange rates that describe the change of p_n due to micro-mixing are taken as

$$\begin{aligned} G_1(p) &= -r_1(p) \\ G_2(p) &= r_1(p) - r_2(p) + r_3(p) \\ G_3(p) &= r_2(p) - 2\cdot r_3(p) + r_4(p) \\ G_4(p) &= r_3(p) - r_4(p) + r_5(p) \\ G_5(p) &= -r_5(p) \end{aligned} \tag{5.41}$$

Conservation of volume fractions requires that

$$\sum_{n=1}^{5} G_n(p) = 0 \tag{5.42}$$

The probability fluxes are given by

$$\begin{aligned} r_1(p) &= \gamma \cdot p_1(1-p_1) \\ r_2(p) &= \gamma \cdot p_2 \\ r_3(p) &= \gamma \cdot p_3 \\ r_4(p) &= \gamma \cdot p_4 \\ r_5(p) &= \gamma \cdot p_5(1-p_5) \end{aligned} \tag{5.43}$$

Global continuity requires that the volume fractions sum to one, i.e.

$$\sum_{n=1}^{5} p_n = 1 \tag{5.44}$$

The relationship between the multi-peak presumed PDF model and other presumed mixture fraction PDF models can be understood when deriving transport equations for the mixture fraction mean and variance from the multi-peak presumed PDF model. The mixture fraction, $<\xi>$ has exactly the same form as the equation for volume fraction, p_n (see Equation (5.40)), except that $G_n=0$. The equation for mixture fraction variance $<\xi'^2>$ contains spurious dissipation terms, and terms can be derived to eliminate the spurious dissipation in the multi-peak presumed PDF model. The relative importance of these terms is small and is therefore neglected in this work (Piton et al., 2000).

Transport equation for volume weighted scalar variables may be written as

$$\frac{\partial \langle s_\phi \rangle_n}{\partial t} + U_j \frac{\partial \langle s_\phi \rangle_n}{\partial x_j} = \frac{\partial}{\partial x_j}\left(\Gamma_T \frac{\partial \langle s_\phi \rangle_n}{\partial x_j} \right) + \underbrace{M_\phi^n(p,s)}_{mixing} + \underbrace{p_n \cdot S_\phi\left(\langle \phi \rangle_n\right)}_{reaction} \tag{5.45}$$

The scalar fluxes between environments which accounts for the micro-mixing are taken as

$$\begin{aligned} M_{\phi}^{1}(p,s) &= -r_1(p)\cdot\langle\phi\rangle_1 \\ M_{\phi}^{2}(p,s) &= r_1(p)\cdot\langle\phi\rangle_1 - r_2(p)\cdot\langle\phi\rangle_2 + r_3(p)\cdot\langle\phi\rangle_3 \\ M_{\phi}^{3}(p,s) &= r_2(p)\cdot\langle\phi\rangle_2 - 2\cdot r_3(p)\cdot\langle\phi\rangle_3 + r_4(p)\cdot\langle\phi\rangle_4 \\ M_{\phi}^{4}(p,s) &= r_3(p)\cdot\langle\phi\rangle_3 - r_4(p)\cdot\langle\phi\rangle_4 + r_5(p)\cdot\langle\phi\rangle_5 \\ M_{\phi}^{5}(p,s) &= -r_5(p)\cdot\langle\phi\rangle_5 \end{aligned} \tag{5.46}$$

Conservation of mass requires that

$$\sum_{n=1}^{5} M_{\phi}^{n}(p,s) = 0 \tag{5.47}$$

The local concentration of the scalar variable, $<\phi>_n$, in environment n can be expressed by

$$\langle\phi\rangle_n = \frac{\langle s_\phi \rangle_n}{p_n} \quad n = 2,3,4 \tag{5.48}$$

The mean value of the scalar variable, $<\phi>$, can be expressed by

$$\langle\phi\rangle = \sum_{n=1}^{5} p_n \cdot \langle\phi\rangle_n = \sum_{n=1}^{5} \langle s_\phi \rangle_n \tag{5.49}$$

The variance of the scalar variable $<\phi'^2>$ can be expressed by

$$\langle\phi'^2\rangle = \sum_{n=1}^{5} \frac{\langle s_\phi \rangle_n^2}{p_n} - \langle\phi\rangle^2 \tag{5.50}$$

The rate of micro-mixing γ can be defined as

$$\gamma = \frac{1}{\tau_m} \tag{5.51}$$

where τ_m is the characteristic timescale for micro-mixing.

Two different micro-mixing timescales will be tested. The first micro-mixing timescale tested is a simple large-scale-motion dominated model denoted MMR1. The characteristic micro-mixing timescale for MMR1 is given by

$$\tau_{m,1} = \frac{1}{C_\phi} \cdot \frac{k}{\varepsilon} \tag{5.52}$$

where C_ϕ=1 (MMR1a) for fully-developed turbulence. For moderate Reynolds numbers close to the transition region and when taking account of the fact that the scalar field near the injection point is not fully developed a value of C_ϕ=0.5 (MMR1b) have been used by others (Marchisio et al., 2000; Marchisio et al., 2001; Piton et al., 2000).

The second micro-mixing timescale tested is the classical formula of Corrsin (1964) denoted MMR2. The characteristic micro-mixing timescale for MMR2 is given by

$$\tau_{m,2} = \frac{3}{2} \cdot \frac{k}{\varepsilon} + \frac{1}{2} \ln(Sc) \left(\frac{\nu}{\varepsilon} \right)^{1/2} \tag{5.53}$$

This timescale contains the correct scaling for fluids with high Schmidt number and is derived for a fully developed turbulence at high Reynolds number where a viscous-convective spectrum is present. For liquid flows, this is the only timescale that accounts for the well-known scaling of -1 for the viscous-convective range at high-Schmidt numbers indicated in Figure 5.1 (Tsai et al., 2002).

Mixing

For a pure mixing case without any reaction transport equations for the volume fractions p_n and the volume weighted mixture fraction $\langle s_\xi \rangle_n$ have to be solved. Since the mixture fraction is constant in environment 1 and 5 only the weighted mixture fraction in environment 2, $\langle s_\xi \rangle_2$, environment 3, $\langle s_\xi \rangle_3$, and environment 4, $\langle s_\xi \rangle_4$, have to be solved. In addition to the five volume fractions that have to be solved this give a total of 8 transport equations.

The transport equations for the volume-weighted mixture fractions can be summarized as

$$\frac{\partial\langle s_\xi\rangle_2}{\partial t}+U_j\frac{\partial\langle s_\xi\rangle_2}{\partial x_j}=\frac{\partial}{\partial x_j}\left(\Gamma_T\frac{\partial\langle s_\xi\rangle_2}{\partial x_j}\right)+\gamma\left[(1-p_1)\cdot\langle s_\xi\rangle_1-\langle s_\xi\rangle_2+\langle s_\xi\rangle_3\right] \tag{5.54}$$

$$\frac{\partial\langle s_\xi\rangle_3}{\partial t}+U_j\frac{\partial\langle s_\xi\rangle_3}{\partial x_j}=\frac{\partial}{\partial x_j}\left(\Gamma_T\frac{\partial\langle s_\xi\rangle_3}{\partial x_j}\right)+\gamma\left[\langle s_\xi\rangle_2-2\cdot\langle s_\xi\rangle_3+\cdot\langle s_\xi\rangle_4\right] \tag{5.55}$$

$$\frac{\partial\langle s_\xi\rangle_4}{\partial t}+U_j\frac{\partial\langle s_\xi\rangle_4}{\partial x_j}=\frac{\partial}{\partial x_j}\left(\Gamma_T\frac{\partial\langle s_\xi\rangle_4}{\partial x_j}\right)+\gamma\left[\langle s_\xi\rangle_3-\langle s_\xi\rangle_4+(1-p_5)\cdot\langle s_\xi\rangle_5\right] \tag{5.56}$$

Table 5.2 gives the typical boundary conditions for the mixing case with 5 environments and two inlet streams

Table 5.2: Typical boundary conditions for the mixing case with 5 environments.

	Inlet stream	
Variable	**1**	**2**
p_1	1	0
p_2	0	0
p_3	0	0
p_4	0	0
p_5	0	1
$<s_\xi>_1$	1	0
$<s_\xi>_2$	0	0
$<s_\xi>_3$	0	0
$<s_\xi>_4$	0	0
$<s_\xi>_5$	0	0
$<\xi>$	1	0

Single reaction

The next step is to put up the transport equations for a simple irreversible chemical reaction like

$$A + B \rightarrow C \tag{5.57}$$

Transport equations for the volume weighted concentration of species A ($<s_{YA}>_n$) and the volume weighted concentration of species B ($<s_{YB}>_n$) in environment 2, 3 and 4 have to be solved. In addition to the five volume fractions that have to be solved this give a total of 11 transport equations for a single reaction case.

The transport equations for the volume-weighted concentration of species A can be summarised as

$$\frac{\partial \langle s_{Y_A} \rangle_2}{\partial t} + U_j \frac{\partial \langle s_{Y_A} \rangle_2}{\partial x_j} = \frac{\partial}{\partial x_j}\left(\Gamma_T \frac{\partial \langle s_{Y_A} \rangle_2}{\partial x_j} \right) + \gamma\left[(1 - p_1) \cdot p_1 - \langle s_{Y_A} \rangle_2 + \langle s_{Y_A} \rangle_3 \right] + p_2 \cdot S\left(\langle Y \rangle_2 \right) \tag{5.58}$$

$$\frac{\partial \langle s_{Y_A} \rangle_3}{\partial t} + U_j \frac{\partial \langle s_{Y_A} \rangle_3}{\partial x_j} = \frac{\partial}{\partial x_j}\left(\Gamma_T \frac{\partial \langle s_{Y_A} \rangle_3}{\partial x_j} \right) + \gamma\left[\langle s_{Y_A} \rangle_2 - 2 \cdot \langle s_{Y_A} \rangle_3 + \langle s_{Y_A} \rangle_4 \right] + p_3 \cdot S\left(\langle Y \rangle_3 \right) \tag{5.59}$$

$$\frac{\partial \langle s_{Y_A} \rangle_4}{\partial t} + U_j \frac{\partial \langle s_{Y_A} \rangle_4}{\partial x_j} = \frac{\partial}{\partial x_j}\left(\Gamma_T \frac{\partial \langle s_{Y_A} \rangle_4}{\partial x_j} \right) + \gamma\left[\langle s_{Y_A} \rangle_3 - \langle s_{Y_A} \rangle_4 \right] + p_4 \cdot S\left(\langle Y \rangle_4 \right) \tag{5.60}$$

Likewise, the transport equations for the volume-weighted concentration of species B can be summarized as

$$\frac{\partial \langle s_{YB} \rangle_2}{\partial t} + U_j \frac{\partial \langle s_{YB} \rangle_2}{\partial x_j} = \frac{\partial}{\partial x_j}\left(\Gamma_T \frac{\partial \langle s_{YB} \rangle_2}{\partial x_j} \right) + \gamma\left[- \langle s_{YB} \rangle_2 + \langle s_{YB} \rangle_3 \right] + p_2 \cdot S\left(\langle Y \rangle_2 \right) \tag{5.61}$$

$$\frac{\partial \langle s_{YB} \rangle_3}{\partial t} + U_j \frac{\partial \langle s_{YB} \rangle_3}{\partial x_j} = \frac{\partial}{\partial x_j}\left(\Gamma_T \frac{\partial \langle s_{YB} \rangle_3}{\partial x_j} \right) + \gamma\left[\langle s_{YB} \rangle_2 - 2 \cdot \langle s_{YB} \rangle_3 + \langle s_{YB} \rangle_4 \right] + p_3 \cdot S\left(\langle Y \rangle_3 \right) \tag{5.62}$$

$$\frac{\partial \langle s_{YB} \rangle_4}{\partial t} + U_j \frac{\partial \langle s_{YB} \rangle_4}{\partial x_j} = \frac{\partial}{\partial x_j}\left(\Gamma_T \frac{\partial \langle s_{YB} \rangle_4}{\partial x_j} \right) + \gamma\left[\langle s_{YB} \rangle_3 - \langle s_{YB} \rangle_4 + (1 - p_5) \cdot p_5 \right] + p_4 \cdot S\left(\langle Y \rangle_4 \right) \tag{5.63}$$

Here, $S(\langle Y \rangle_2)$, $S(\langle Y \rangle_3)$ and $S(\langle Y \rangle_4)$ represents the rate of change of $\langle s_\phi \rangle_n$ due to the chemical source term, i.e. reaction, and can be expressed by

$$\begin{aligned} S\left(\langle Y \rangle_2 \right) &= -k_1 \cdot \langle Y_A \rangle_2 \cdot \langle Y_B \rangle_2 \\ S\left(\langle Y \rangle_3 \right) &= -k_1 \cdot \langle Y_A \rangle_3 \cdot \langle Y_B \rangle_3 \\ S\left(\langle Y \rangle_4 \right) &= -k_1 \cdot \langle Y_A \rangle_4 \cdot \langle Y_B \rangle_4 \end{aligned} \tag{5.64}$$

Table 5.3 gives the typical boundary conditions for the reacting case with 5 environments and two inlet streams.

Table 5.3: Typical boundary conditions for the single reaction case with 5 environments.

	Inlet stream	
Variable	**1**	**2**
p_1	1	0
p_2	0	0
p_3	0	0
p_4	0	0
p_5	0	1
$<s_{YA}>_1$	1	0
$<s_{YA}>_2$	0	0
$<s_{YA}>_3$	0	0
$<s_{YA}>_4$	0	0
$<s_{YA}>_5$	0	0
$<Y_A>$	1	0
$<s_{YB}>_1$	0	0
$<s_{YB}>_2$	0	0
$<s_{YB}>_3$	0	0
$<s_{YB}>_4$	0	0
$<s_{YB}>_5$	0	1
$<Y_B>$	0	1

5.6 Solution procedure

The governing equations given above are solved by a finite volume method (Patankar, 1980). The calculation domain is divided into a number of control volumes. At the centre of the control volumes, the scalar variables are stored. A staggered grid is used for the velocity components that are stored at the surface of the control volumes. The SIMPLE algorithm updates pressure and corrects the velocities. Power law differencing is used for all variables.

Chapter 6

Simulations of a tubular reactor*

6.1 Introduction

In this chapter the EDC-model will be validated on an infinitely fast chemical reaction in a turbulent liquid flow. The model is improved to make it more suitable for liquid phase reactions. Different presumed PDF models are also tested. The numerical results are compared to the experimental data of Pohorecki and Baldyga (1983) and the numerical simulations performed by Hannon et al. (1998).

6.2 Numerical configuration

6.2.1 Simulation data

The various reaction and turbulence models will be tested against the experimental data of Pohorecki and Baldyga (1983), where they found the reaction-zone length for 95 % conversion of species A (base), for a simple acid-base neutralisation expressed as

$$A + B \rightarrow C \qquad (6.1)$$

*Based on: Hjertager, L.K., B.H Hjertager and T. Solberg (2002). 'CFD Modeling of Fast Chemical Reactions in Turbulent Liquid Flows'. *Computers and Chemical Engineering* **26**, 507-515.

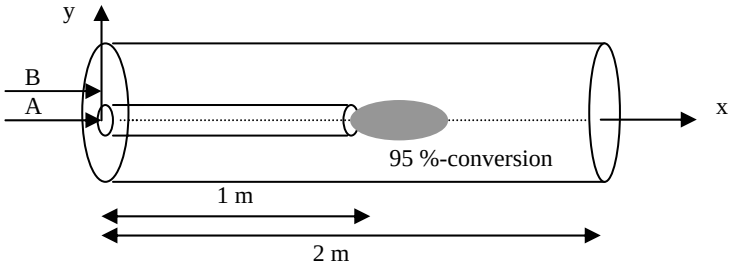

Figure 6.1: The simulated tube reactor.

Table 6.1: Data for the numerical simulations.

	Diameter [m]	Length [m]	Feed Component
Outer tube	0.04	2	B (Acid)
Inner tube	0.0052	1	A (Base)

Figure 6.1 shows the tube arrangement that was simulated. Table 6.1 shows the configuration data used in the numerical simulations.

The simulations were performed at three different Reynolds numbers; 13000, 20000 and 25000. The simulations were performed with the standard EDC-model, the EDC-model with an algebraic expression for the scalar dissipation time scale (EDC-SDT), and the EDC-model with the multiple-time-scale turbulent mixer model (EDC-MTS) as described in Chapter 5.4.

Simulations were also performed with the use of two different presumed PDF models, the double peak PDF and the beta PDF. The Schmidt number was set to 800. The reaction rate constant, A, was set to 4 in the first cases and calibrated to 1 in the EDC-MTS case. Both the standard k-ε-model and the RNG-k-ε-model were used in the simulations.

6.2.2 Grid

The tubular reactor geometry was modelled as two-dimensional and axi-symmetric. The grid used had 1302×50 cells, where the grid in the y-direction had a constant size, and the grid in the x-direction was expanding. This was done to get a finer grid in the area where the reaction takes place. The grid size in the reaction zone was approximately $4 \cdot 10^{-4}$ m in the x- and y-directions.

6.3 Results and discussion

Figure 6.2 shows the results from the simulations where the standard EDC-model was used. The results are compared to the experimental data by Pohorecki and Baldyga (1983) and the numerical results by Hannon et al. (1998) where EDC-model was used. Clearly the standard EDC-model is not able to predict the reaction-zone length found in the experiments of Pohorecki and Baldyga (1983). Compared to the numerical results by Hannon et al. (1998), the standard EDC-model predicts a longer reaction-zone length. As pointed out by Hannon et al. (1998), the reason for the short reaction-zone length may be caused by the fact that the EDC-model contains no information about mixing at the scales where viscous/diffusive effects are important.

Figure 6.3 gives the results from the simulations where the EDC-SDT-model was used. Figure 6.3 shows that the EDC-SDT-model does not give a much better prediction of the reaction-zone length found in the experiments of Pohorecki and Baldyga (1983) than the standard EDC-model. The reaction-zone length is still too short, indicating that the time scale is still not right.

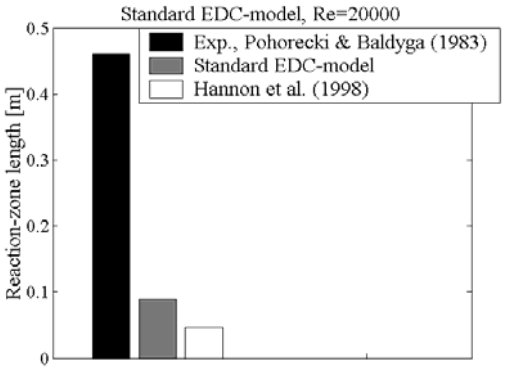

Figure 6.2: Predicted reaction-zone length with the standard EDC-model.

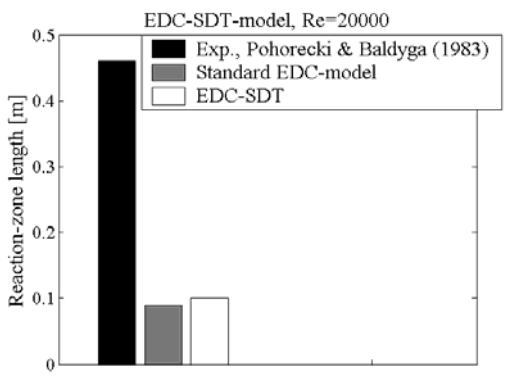

Figure 6.3: Predicted reaction-zone length with the EDC-SDT-model.

Table 6.2: Predicted reaction-zone length with the EDC-MTS model with different parameters.

Re-number	**Pohorecki and Baldyga (1983)**	**k-ε- model, A=4**	**k-ε-model, A=1**	**RNG-k-ε-model, A=1**
13000	0.55	0.33	0.40	0.40
20000	0.46	0.36	0.44	0.45
25000	0.38	0.38	0.47	0.48

Table 6.2 gives the results from simulations where the EDC-MTS model was used. Table 6.2 shows that using the reaction rate constant, A=4, which is calibrated for combustion reactions gives shorter reactions-zone lengths than the measured ones. A recalibrated value of A=1 appears to be better suited for liquid phase reactions. Results where the RNG-k-ε-model is used instead of the standard k-ε-model is also given in Table 6.2. Both models give approximately the same results for all three Reynolds-numbers.

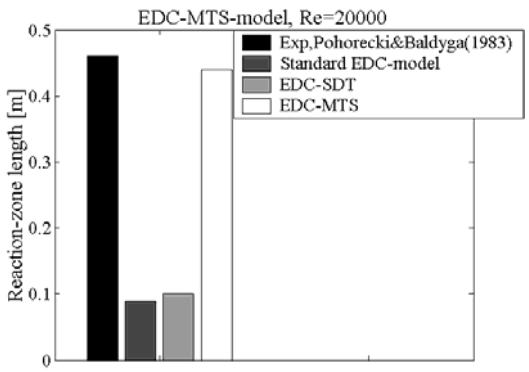

Figure 6.4: Predicted reaction-zone length with the EDC-MTS-model.

Figure 6.4 shows the results from the simulations with the EDC-MTS-model where the reaction rate constant was modified to A=1. Apparently the EDC-MTS-model is able to predict the reaction-zone length found in the experiments of Pohorecki and Baldyga (1983). The reaction-zone length is approximately the same, indicating that the micromixing is taken account for by having a multiple-time scale.

Figure 6.5 shows the distribution of the reaction rate using the EDC-MTS model and Figure 6.6 shows the distribution of mass fraction of species A for the same case.

In Figure 6.7, the reaction-zone length predicted with the different EDC-models at the three different Reynolds numbers are illustrated. The EDC-MTS model is noticed to be the most promising model since it is the only model which is able to predict the reaction-zone length within a reasonable limit. None of the models are able to predict the effect of increasing Reynolds number, not even the EDC-MTS model in which the effect of mixing at scales where viscous/diffusive effects are important should be accounted for.

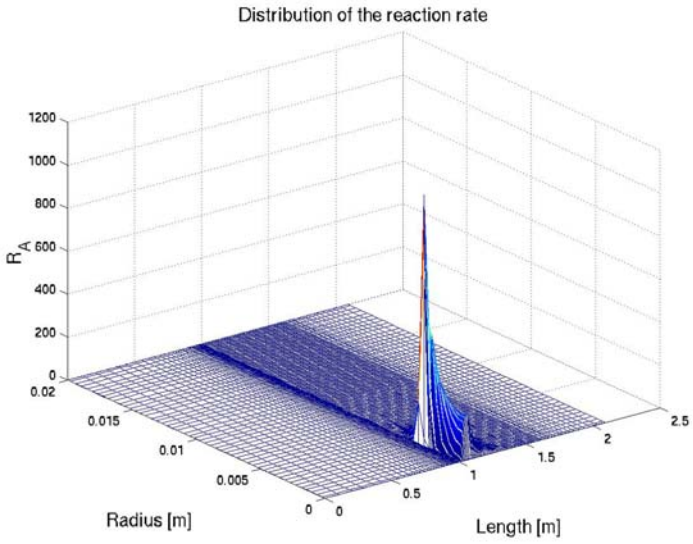

Figure 6.5: Distribution of the reaction rate from the EDC-MTS-model.

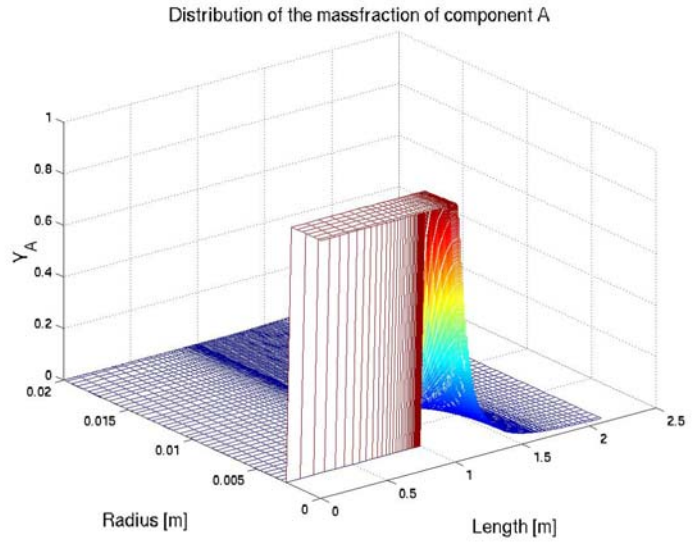

Figure 6.6: Mass fraction of species A from the EDC-MTS-model.

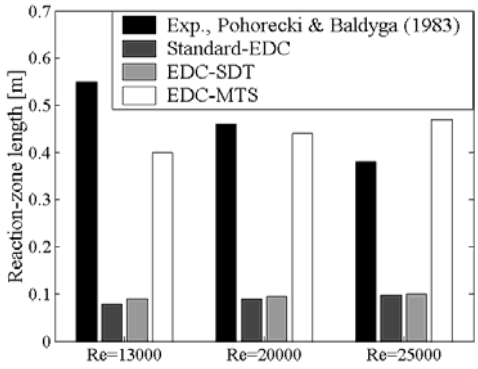

Figure 6.7: Comparing the results from the different EDC-models at different Reynolds numbers.

In Figure 6.8, the results from the different PDF-models are compared with the numerical results by Hannon et al. (1998) where they used Baldyga's model (Baldyga, 1989). Present double peak PDF and beta PDF reaction predictions exhibit a too short reaction zone length. The beta PDF is the only model that is able to predict the correct influence of increasing Reynolds number. The same type of model used by Hannon et al. (1998) gave very satisfying results using the commercial CFD code, Fluent. This indicates that the reason why the EDC-MTS model is not able to predict this effect can be because the EDC-model uses time-averaged concentrations in the reaction rate expression instead of instantaneous concentrations as in Baldyga's model.

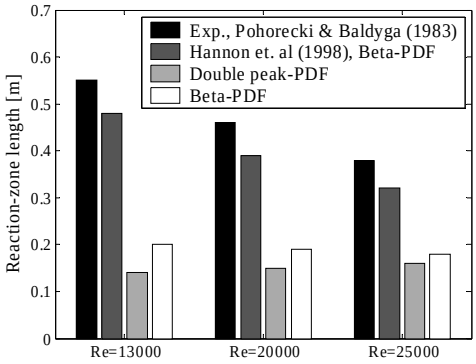

Figure 6.8: Comparing the results from the different PDF-models at different Reynolds numbers.

6.4 Concluding remarks

The EDC-model has been examined and the results showed that the standard-EDC model is not able to predict the reaction-zone length for an acid-base neutralisation in a tubular reactor correctly.

The first modification denoted the EDC-SDT-model, in which the time scale of fluid dynamic dissipation was replaced with the time scale of scalar dissipation, did not improve the results much. The second modification denoted the EDC-MTS model that accounted for multiple time scales gave results that were comparable with the experimental results. None of the models were able to predict the effect of increasing Reynolds number, not even the EDC-MTS model in which the effect of mixing at scales where viscous/diffusive effects are important are taken into account. This may be caused by the fact that the EDC-model uses time-averaged concentrations in the reaction rate expression instead of instantaneous concentrations.

Both the double peak and the beta PDF model predict too short reaction-zone length. The beta PDF model is the only model that predicts correctly the effect of increasing Reynolds-numbers. This is probably due to the fact that this model uses instantaneous concentrations.

Chapter 7

Simulations of turbulent mixing*

7.1 Introduction

In Chapter 3, measurements of turbulent mixing in a mixing channel for three different flow cases were presented. These measurements will in this chapter be used to evaluate numerical simulations of that flow. First three versions of the k-ε turbulence model will be evaluated by comparing predicted and measured profiles of axial and transverse mean velocities and their fluctuations. Then the mean concentration of the passive tracer and its fluctuations will be evaluated to test the performance of two different mixing models. PDF's from the experiments will also be compared with the PDF's obtained from the multi-peak presumed PDF model.

7.2 Numerical configuration

The numerical model uses a two-dimensional grid, which represents the geometry of the mixing channel shown in Figure 7.1. Three cases with different inlet velocity in the two feed channels are simulated, see Table 7.1. The grid is uniform and consists of 200×50 cells in axial and transverse directions, respectively. Accordingly, the grid cell size is 5×1.2 mm^2. The inlet concentration in feed channel A, $C_{A,b}$=1 and the inlet concentration in feed channel B, $C_{B,b}$=0.

*Partly based on: Hjertager, L.K., B.H. Hjertager, and T. Solberg (2003). 'CFD modelling of turbulent mixing in a confined wake flow'. Proceedings AIChE Annual Meeting, San Francisco, CA., USA, Nov. 16-21.

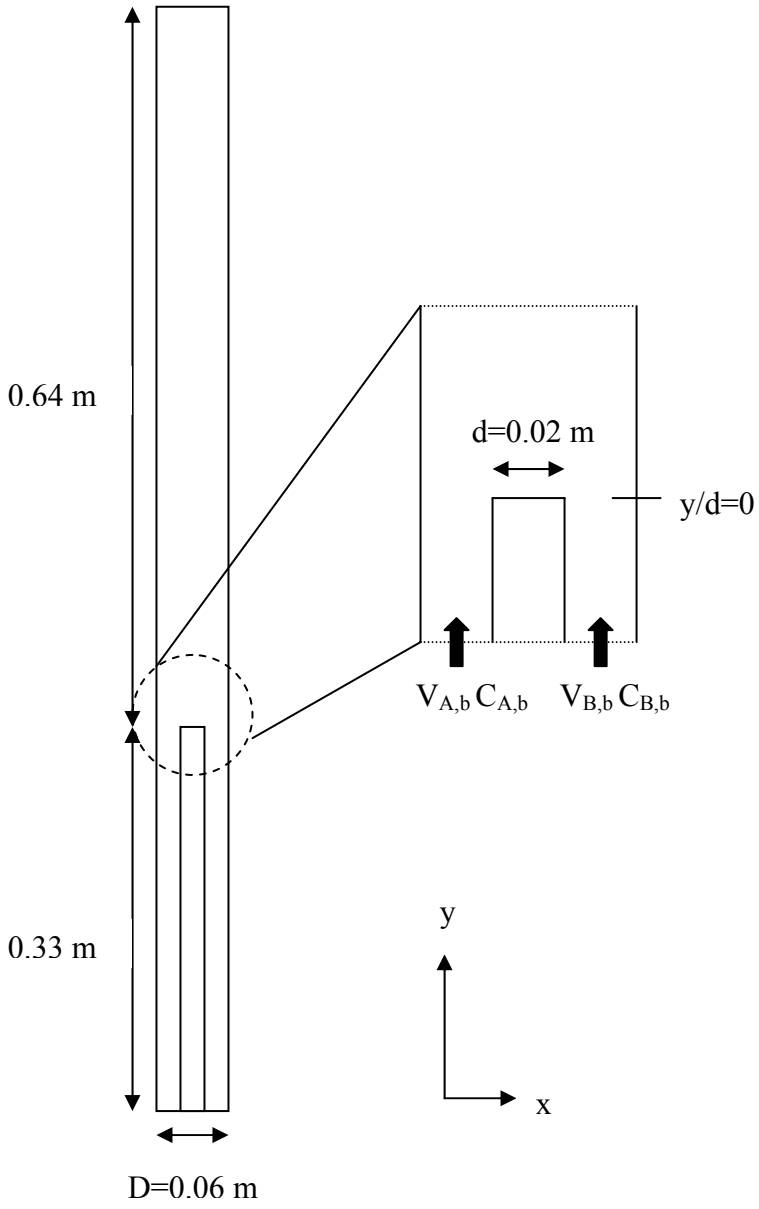

Figure 7.1: Schematic drawing of the simulated mixing channel.

Table 7.1: Velocities for the different flow cases.

	Velocity [m/s]	
Case	**Inlet A($V_{A,b}$)**	**Inlet B($V_{B,b}$)**
1	0.17	0.17
2	0.085	0.17
3	0.0425	0.17

The turbulence is modelled by using three different versions of the k-ε model, i.e. the standard k-ε model, the RNG k-ε model and the Chen-Kim k-ε model. Mixing is modelled by the use of the two mixing models: the multiple timescale turbulent mixer model and the multi-peak presumed PDF model with 5 environments (referred to here as 5-peak presumed PDF model). The turbulence and mixing models were presented in Chapter 5.3, 5.4 and 5.5, respectively.

7.3 Mixing predictions for case 1, velocity ratio 1:1

7.3.1 Mean and fluctuating velocities

In Figures 7.2 and 7.3, axial (V) and transverse (U) velocity profiles at different axial positions for different versions of the k-ε model are shown and compared to the experimental data. As noticed, the different k-ε models predict almost similar profiles. Some discrepancies between measured and simulated velocities are observed. In particular, the simulated wake tends to recover slower than the measured one.

The predicted turbulent velocity $u_t = \sqrt{2/3k}$ is expected to lie in between the axial (v_{rms}) and transverse (u_{rms}) turbulent velocity fluctuations. As shown in Figure 7.4, the shape of the predicted turbulent velocity is similar to the measured turbulent velocity fluctuations, but the turbulence levels are somewhat underpredicted. Accordingly, the turbulent viscosity also appears to be underpredicted. Clearly, the k-ε turbulence model is not able to account for the influence of the large scale fluctuating motion found in the near wake of the separating block. A Large Eddy Simulation (LES) turbulence model would certainly be a better choice for this flow.

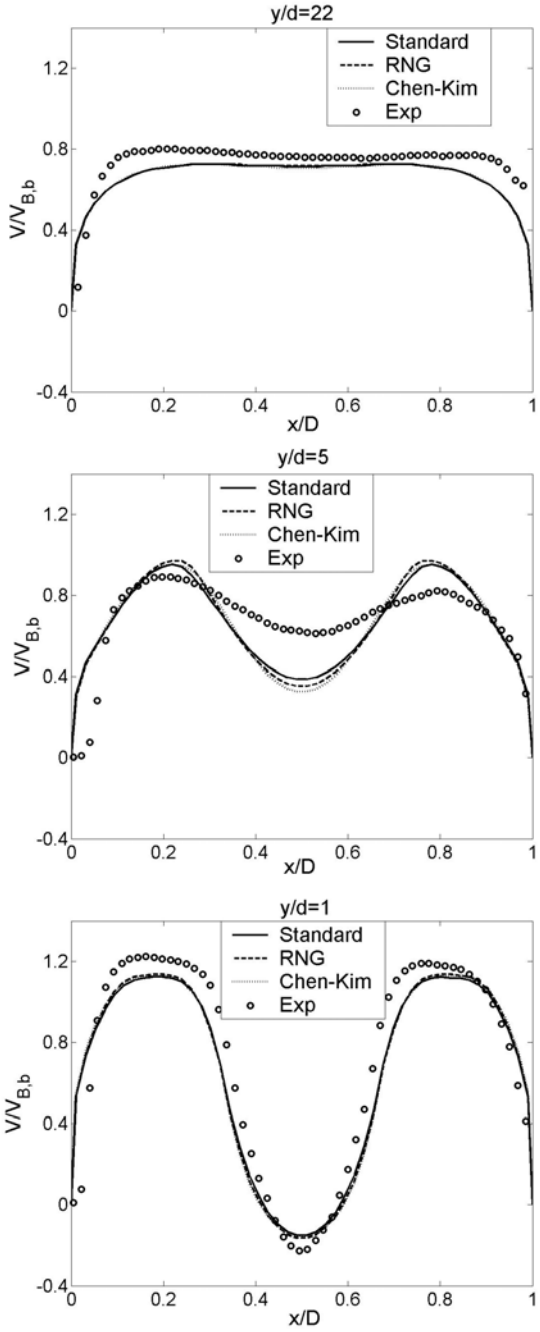

Figure 7.2: Axial(V) velocity profiles at different axial positions for case 1.

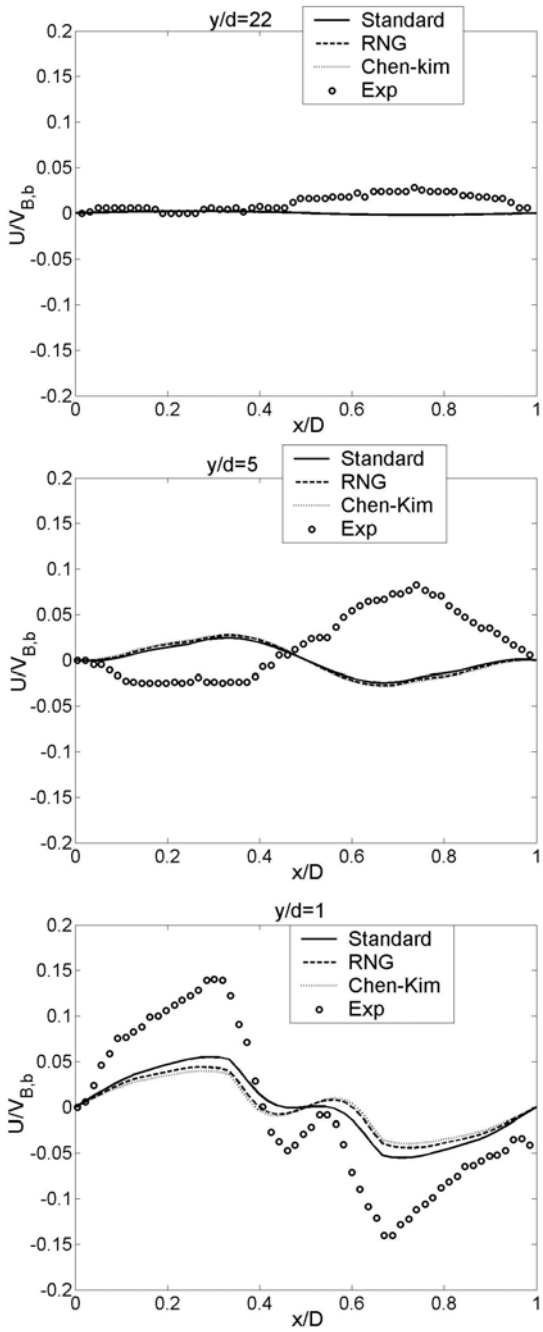

Figure 7.3: Transverse (U) velocity profiles at different axial positions for case 1.

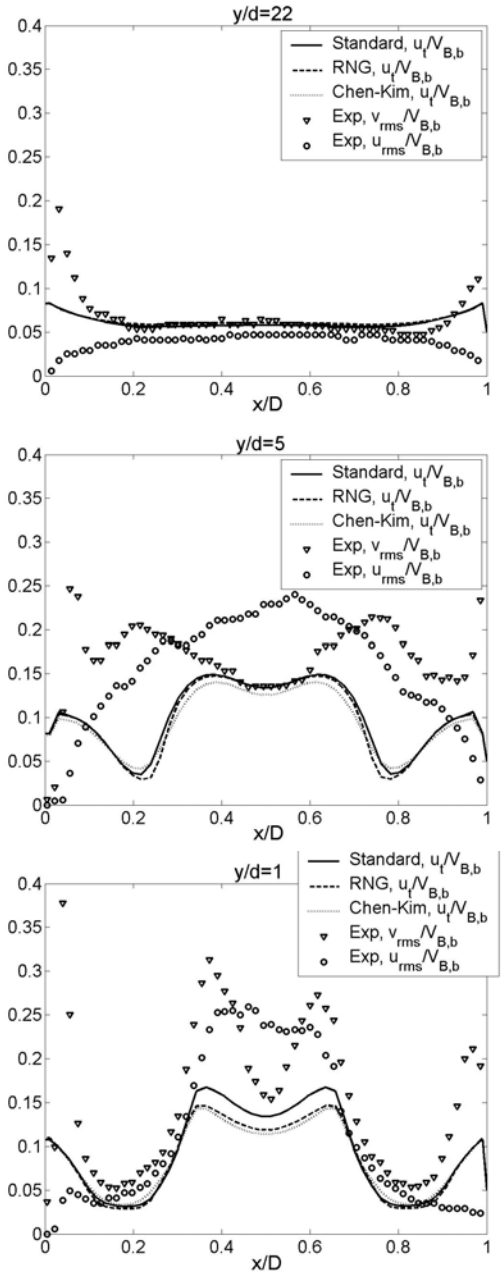

Figure 7.4: Axial(v_{rms}) and transverse (u_{rms}) velocity fluctuations compared to the turbulence velocity (u_t) at different axial positions for case 1.

7.3.2 Mean and fluctuating concentrations

In Figure 7.5, predicted mean concentration profiles for the three different k-ε-models are shown. Again, they are noted to yield very similar results. In Figure 7.6, predicted mean concentration profiles using different turbulent Schmidt Sc_T numbers are shown. The agreement between predictions and measurements tends to improve by reducing the turbulent Schmidt number from $Sc_T = 0.70$ to $Sc_T = 0.15$. However, discrepancies found in the mean velocity will certainly also appear in the mean concentration.

In Figure 7.7, predicted concentration fluctuations for the MTS model using different turbulent Schmidt numbers are shown. Again, reducing the turbulent Schmidt from $Sc_T = 0.70$ to $Sc_T = 0.15$ in the predictions appears to improve the agreement with the measurements.

In Figures 7.8, 7.9 and 7.10, predicted concentration fluctuations from the 5-peak presumed PDF model using different turbulent Schmidt numbers are shown for the three micromixing timescales considered. The effect of the Schmidt number is observed to be the same as for the MTS model. In Figure 7.8, the micromixing timescale MMR1a (see Equation (5.52)) is used in the predictions, whereas the micromixing timescale MMR1b is used in Figure 7.9. The micromixing timescale MMR2 (see Equation (5.53)) is used in the predictions in Figure 7.10. The micromixing timescale MMR1a, which is a simple large-scale dominated model seems to give the best agreement between predictions and measurements. Comparing the two mixing models, that is the MTS model in Figure 7.7 and the 5-peak model using MMR1a in Figure 7.8, the latter model appear to give predictions in better agreement with the experimental data.

He et al. (1999) have tested the adequacy and accuracy of the constant turbulent Schmidt number assumption in predicting turbulent scalar fields in jet-in-cross-flows. They have simulated a round jet that was injected into a confined cross-flow in a rectangular tunnel using the RANS equations with the standard k-ε turbulence model. The major observation in their work is that the turbulent Schmidt number has a significant effect on the prediction of the species spreading rate in jet-to-crossflows, especially for the cases where jet-to-crossflow momentum flux ratios are relatively small. They recommended a turbulent Schmidt number of 0.2

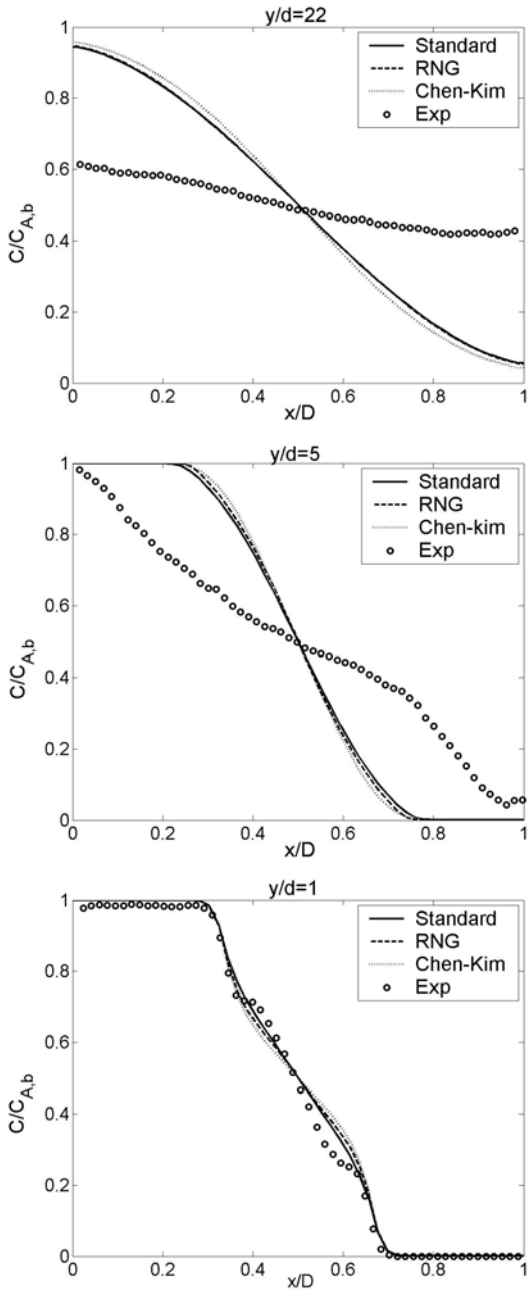

Figure 7.5: Concentration profiles from different turbulence models compared to experimental data for case 1.

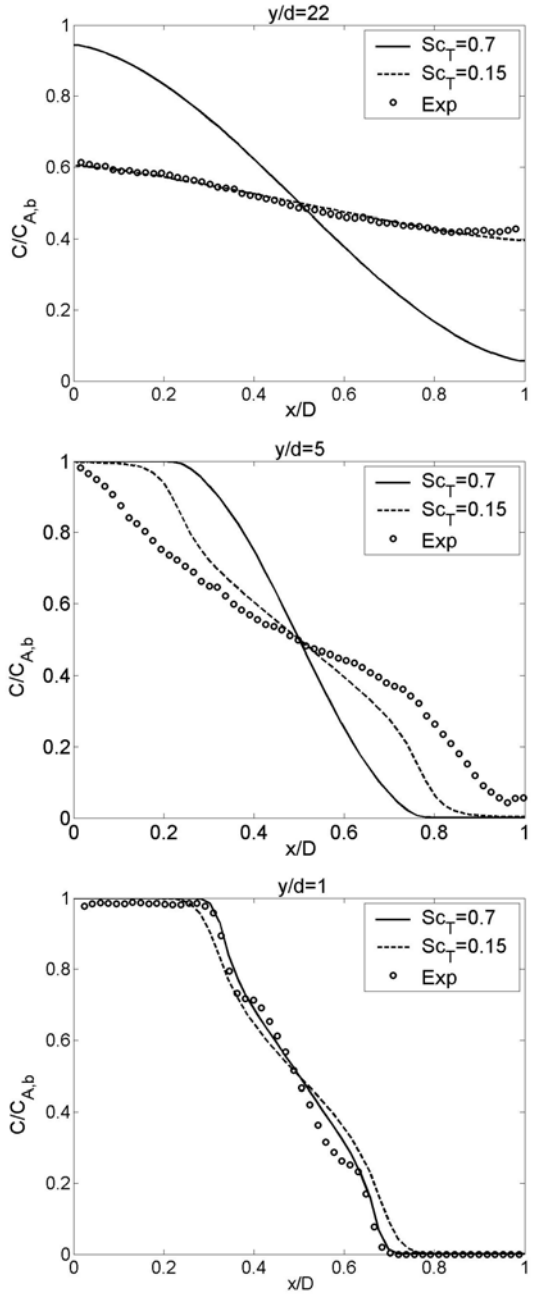

Figure 7.6: Concentration profiles from different turbulent Schmidt numbers compared to experimental data for case 1.

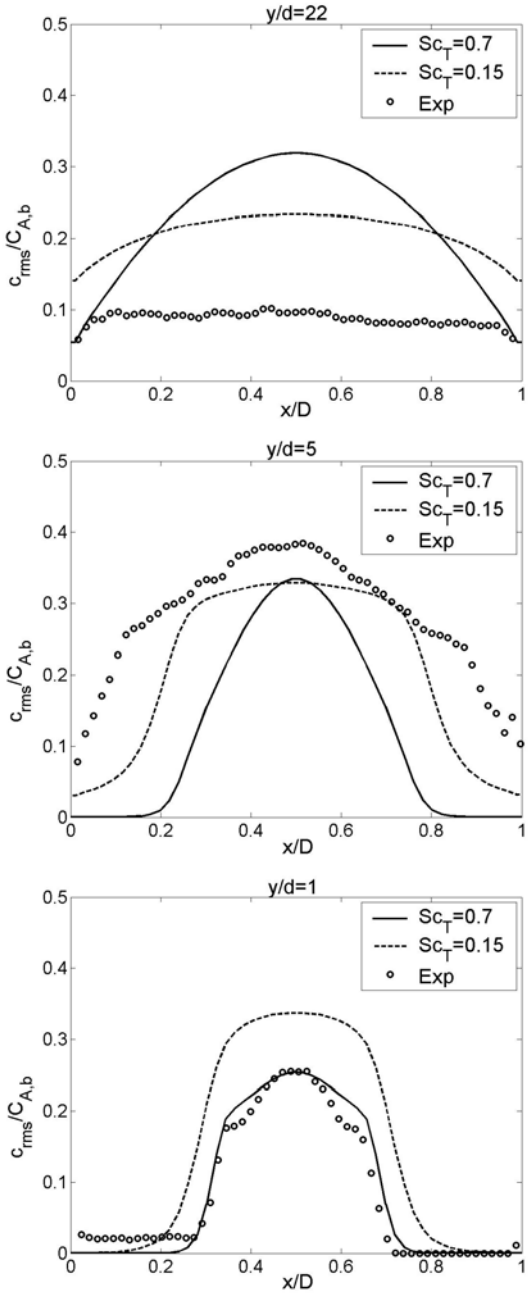

Figure 7.7: Concentration fluctuations from the MTS-model with different turbulent Schmidt numbers compared to experimental data for case 1.

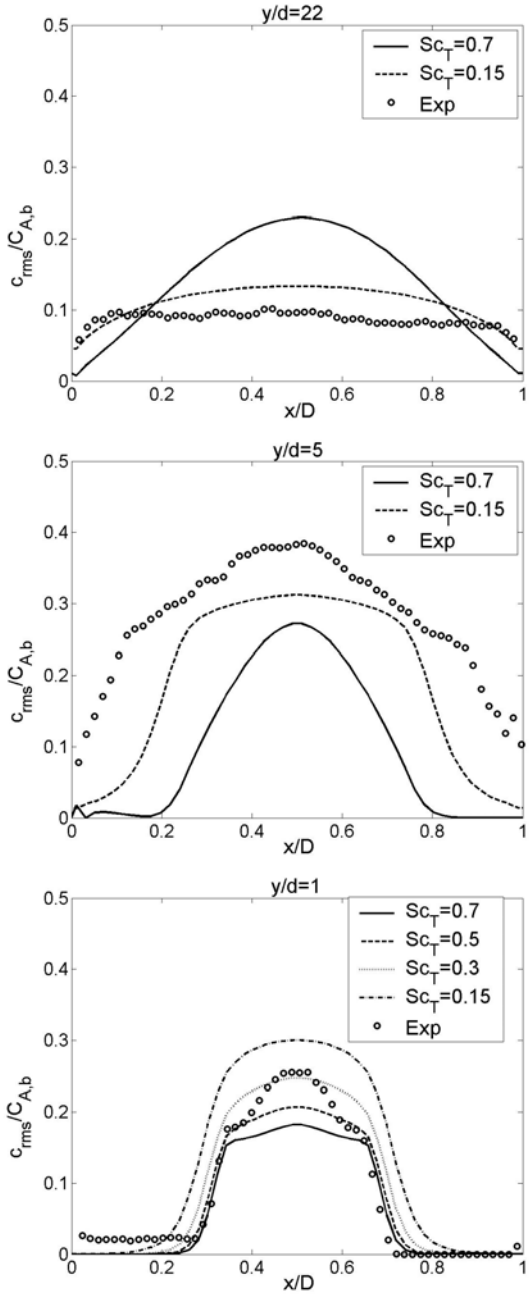

Figure 7.8: Concentration fluctuations from the 5-peak model-MMR1a with different turbulent Schmidt numbers compared to experimental data for case 1.

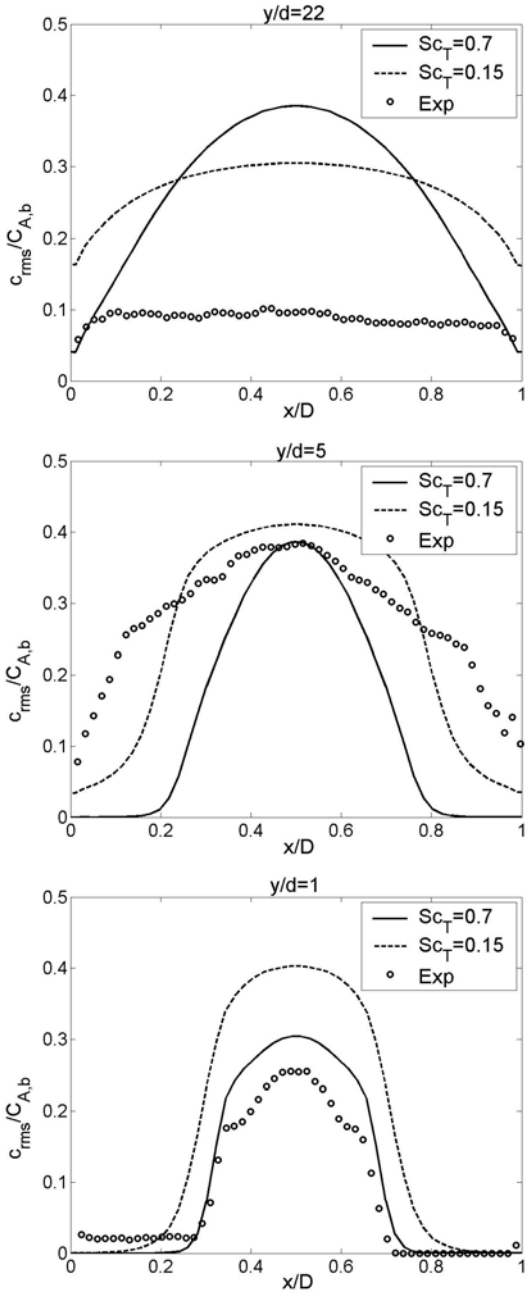

Figure 7.9: Concentration fluctuations from the 5-peak model-MMR1b with different turbulent Schmidt numbers compared to experimental data for case 1.

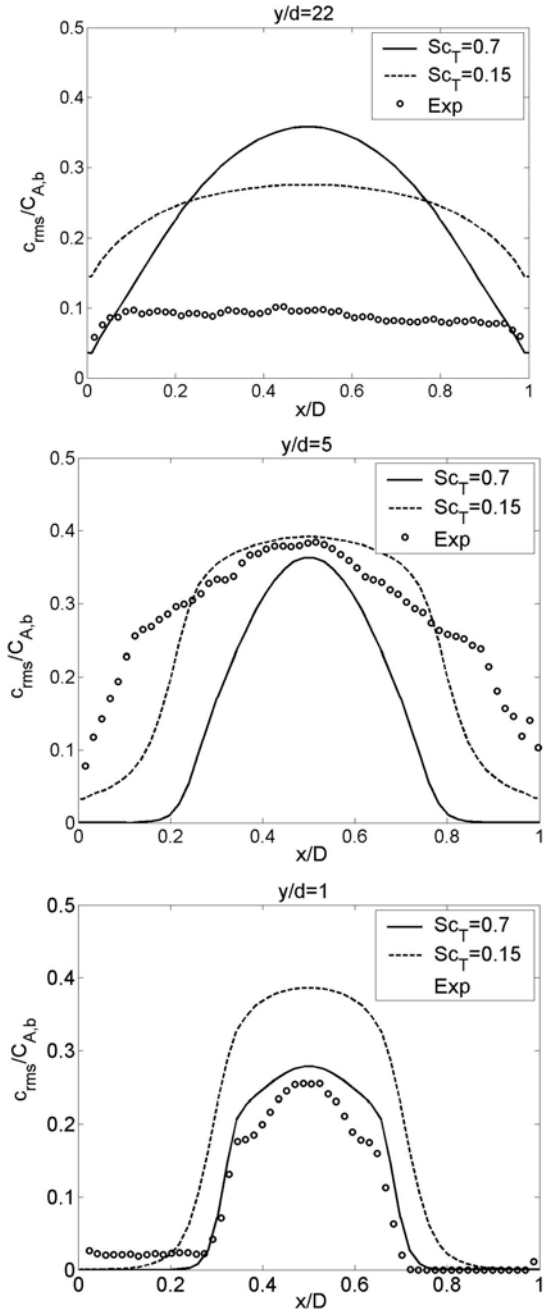

Figure 7.10: Concentration fluctuations from the 5-peak model-MMR2 with different turbulent Schmidt numbers compared to experimental data for case 1.

for best agreement with experimental data, which is close to 0.15 found in this work.

Pollei et al. (2000) have studied a simple mixing tube where the inlet cross section was divided into two coaxial regions where the reactants entered. They measured the mixing length visually and compared it with numerical simulations. The mixing predicted by $Sc_T = 0.9$ was too strong. The predicted mixing length was 2/3 of the measured one. They obtained a very good agreement between experiments and simulations for $Sc_T = 2.5$. In the case studied here and in the work of He et al. (1999) the turbulent Schmidt number had to be reduced to fit the experimental results. This indicates that the turbulent Schmidt number may be flow dependent and that there may be introduced a significant uncertainty by using a constant value.

7.3.3 Analysis of degree of mixing

Macro- and micro-mixing

The 5-peak model using MMR1a with $Sc_T = 0.15$ seemed to give the best predictions at all three axial positions. Therefore the coefficient of variation (CoV) and the decay function (d) (defined in Chapter 3.5.5) shown in Figures 7.11 and 7.12 is from the simulations using MMR1a and $Sc_T = 0.15$.

In Figure 7.11 the predicted and measured coefficient of variation are plotted along the channel length. In the recirculation zone the predicted CoV fits the experimental data well, this is also the case at y/d=22. From y/d=2 to y/d=6 it seems that the macro-mixing happens faster in the experiment than in the predictions.

In Figure 7.12 the predicted and measured decay function are plotted along the channel length. The predicted decay function fits the experimental data well in the recirculation zone and also at y/d=22. From y/d=2 to y/d=6 the predicted decay function is lower than the measured one.

This supports the results seen from the mean- and fluctuating concentrations.

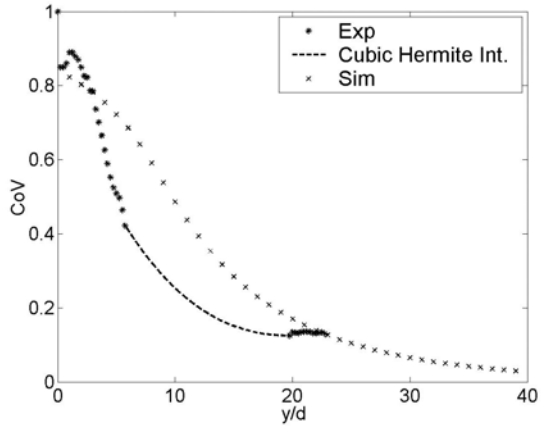

Figure 7.11: Measured and predicted Coefficient of Variation for case 1.

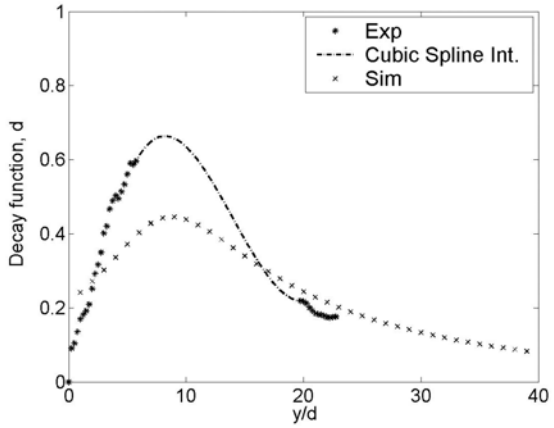

Figure 7.12: Measured and predicted decay function for case 1.

Probability density functions

The 5-peak model using MMR1a with $Sc_T = 0.15$ seemed to give the best predictions at all three axial positions. When comparing the PDF's from the 5-peak model with the PDF's from the experiment it is important that the concentration profiles and concentration fluctuation profiles fits as closely as possible therefore the PDF's shown in Figure 7.13 is from the simulations using MMR1a and $Sc_T = 0.15$. The overall agreement between the measured and predicted PDF's is quite good.

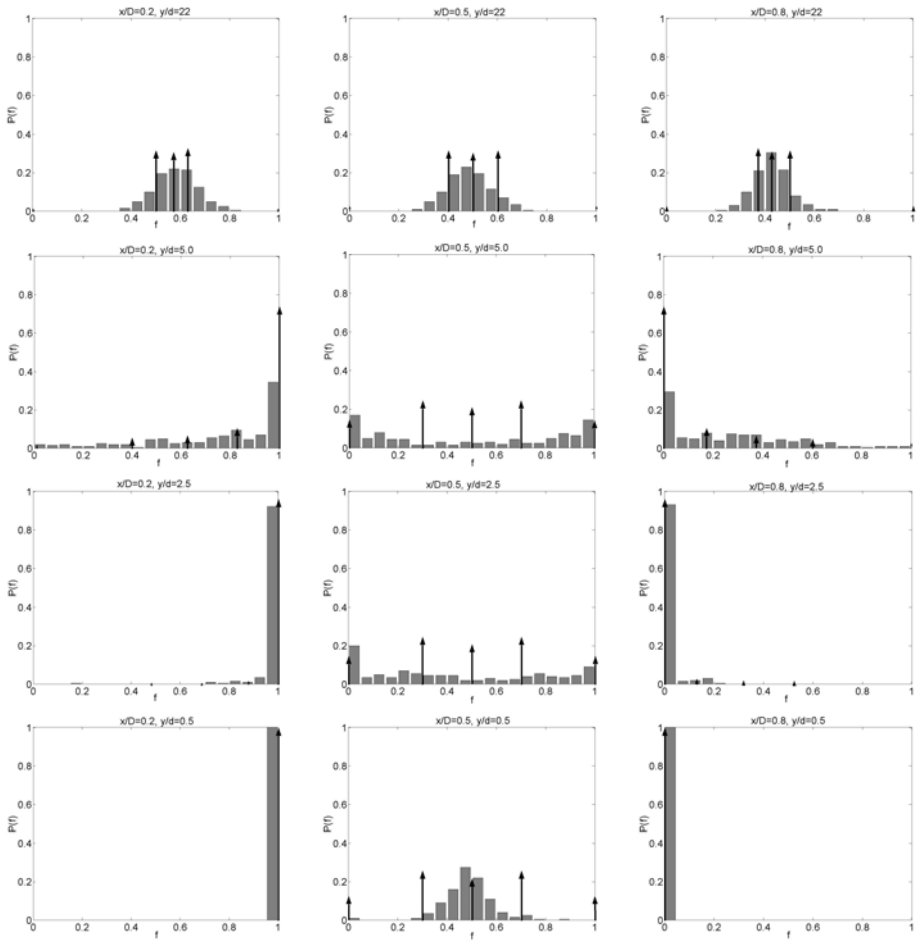

Figure 7.13: PDF's at different axial and transverse positions in the channel. ↑ - Num, 5-peak, MMR1a ▩ - Exp.

In Figure 7.14 the PDF's at x/D=0.5 for different axial positions are shown. At the left side the PDF's from MMR1a with $Sc_T = 0.70$ is shown and at the right side PDF's with $Sc_T = 0.15$ is shown. The trend for the PDF's calculated with different turbulent Schmidt number is the same as for the mean and fluctuating concentrations.

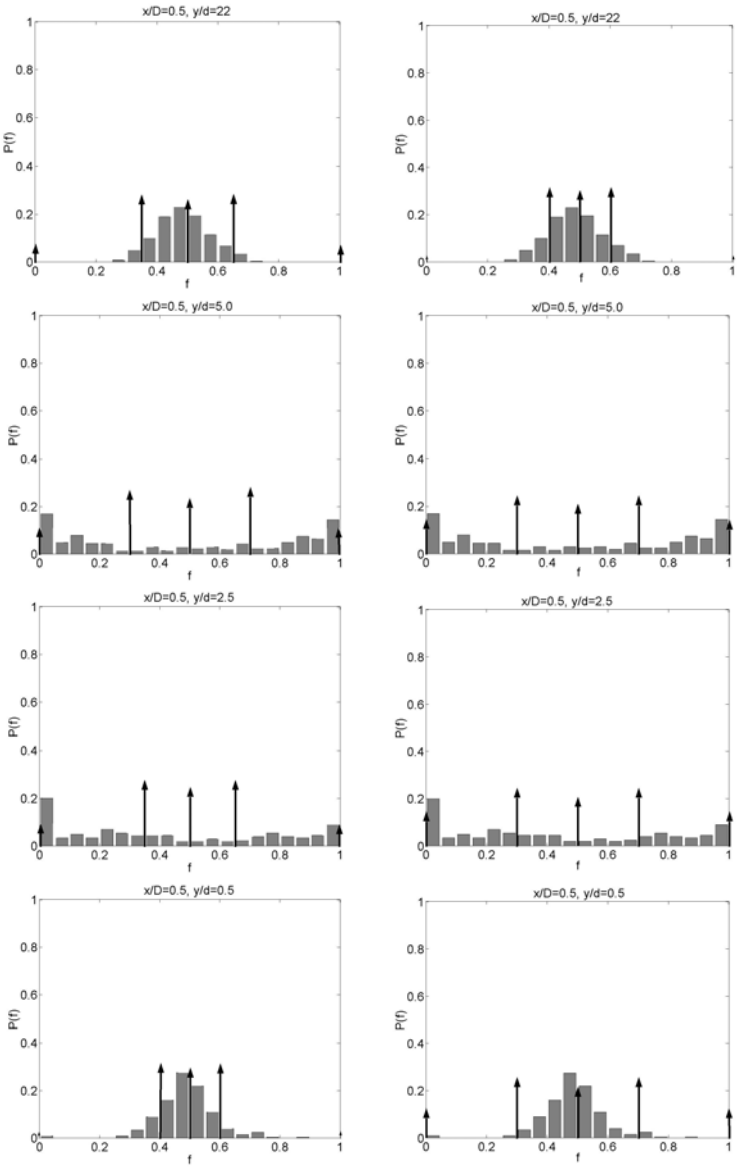

Figure 7.14: PDF's at x/D=0.5 Left: Sc_T=0.7 Right: Sc_T=0.15
↑ - Num, 5-peak, MMR1a ■ - Exp.

7.4 Mixing predictions for case 2, velocity ratio 0.5:1

7.4.1 Mean and fluctuating velocities

In Figures 7.15 and 7.16, axial (V) and transverse (U) velocity profiles at different axial positions for different versions of the k-ε model for case 2 are shown and compared to the experimental data. Again the different k-ε models predict almost similar profiles, except at y/d=22 where the Chen-Kim model prediction deviates a bit from the two other models. The agreement between measured and simulated velocities is better than for case 1. Especially, the profile at y/d=22 fits well with experimental data.

As shown in Figure 7.17, the predicted turbulent velocity fits well with the measured turbulent velocity fluctuations, especially at y/d=22. This indicates that the turbulent viscosity is well predicted by the k-ε model for this case. This may be caused by the fact that the fluctuating motion in this flow is not as large as in case 1, and therefore the k-ε model is able to give a better prediction of this flow. The weak backflow observed in the experiment along the left channel wall is not captured by the predictions indicating that the k-ε model is not the best choice for this case either.

7.4.2 Mean and fluctuating concentrations

In Figure 7.18, predicted mean concentration profiles for the three different k-ε-models for case 2 are shown. Again, they are noted to yield very similar results. In Figure 7.19, predicted mean concentration profiles using different turbulent Schmidt Sc_T numbers are shown. The agreement between predictions and measurements is good when using a turbulent Schmidt number of $Sc_T = 0.70$, but reducing it to $Sc_T = 0.50$ improves the results and make them even better. For this case where the predicted velocity profiles fitted well with the experimental data, the concentration profiles were also expected to fit well.

In Figure 7.20, predicted concentration fluctuations for the MTS model using different turbulent Schmidt numbers are shown. Reducing the turbulent Schmidt from $Sc_T = 0.70$ to $Sc_T = 0.50$ did not have a great impact on the results. In Figure 7.21, 7.22 and 7.23, predicted concentration fluctuations from the 5-peak presumed PDF model using

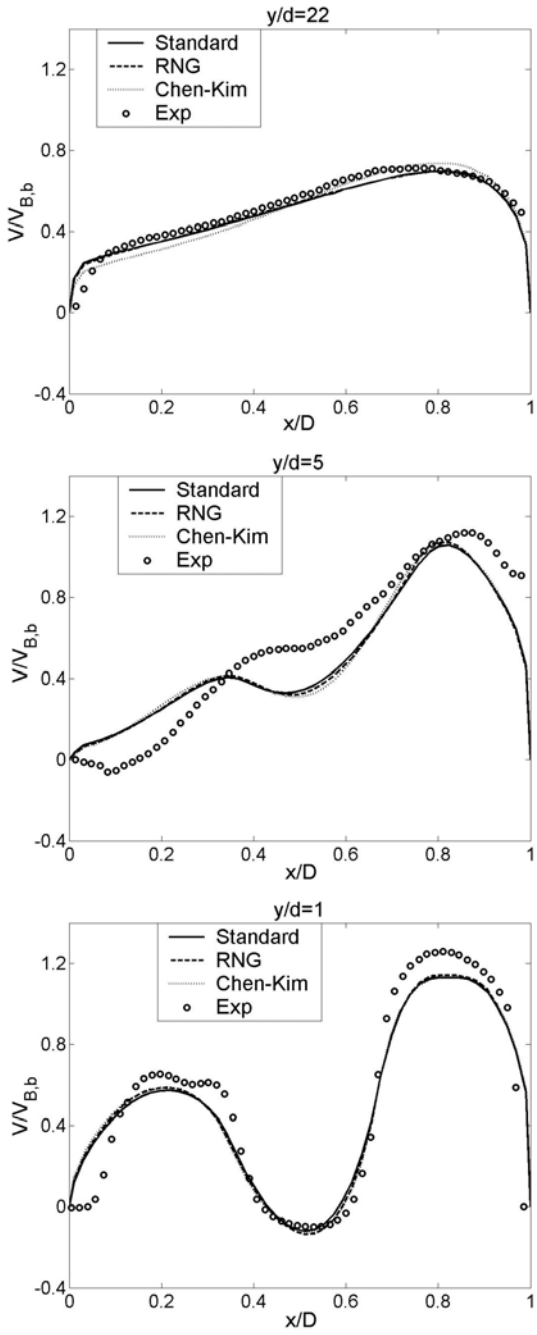

Figure 7.15: Axial (V) velocity profiles at different axial positions for case 2.

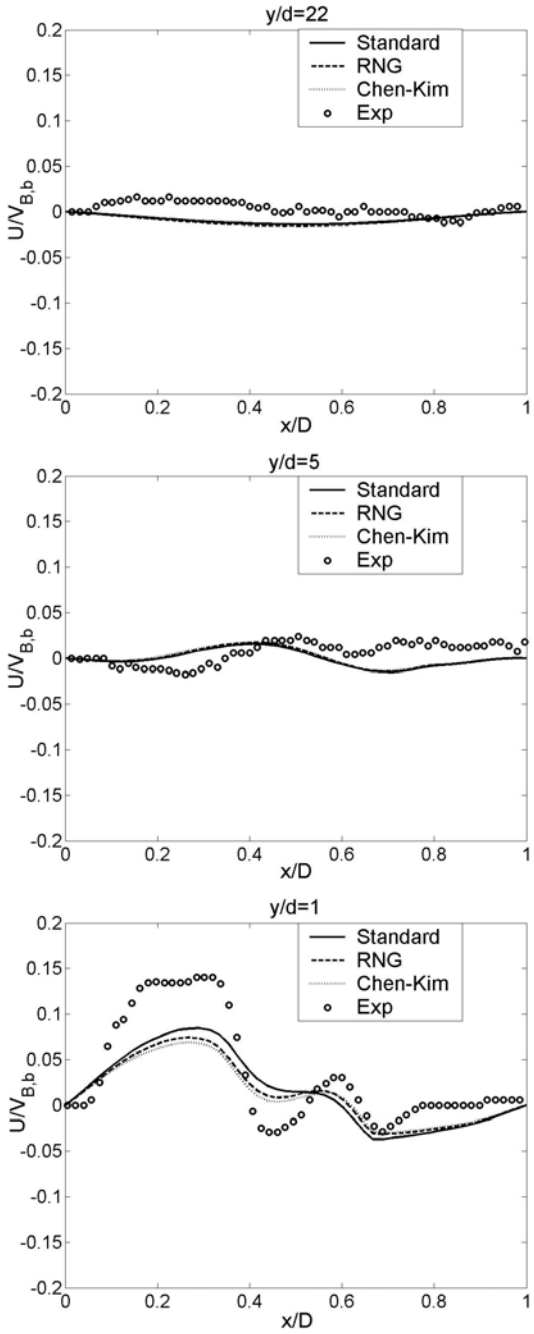

Figure 7.16: Transverse (U) velocity profiles at different axial positions for case 2.

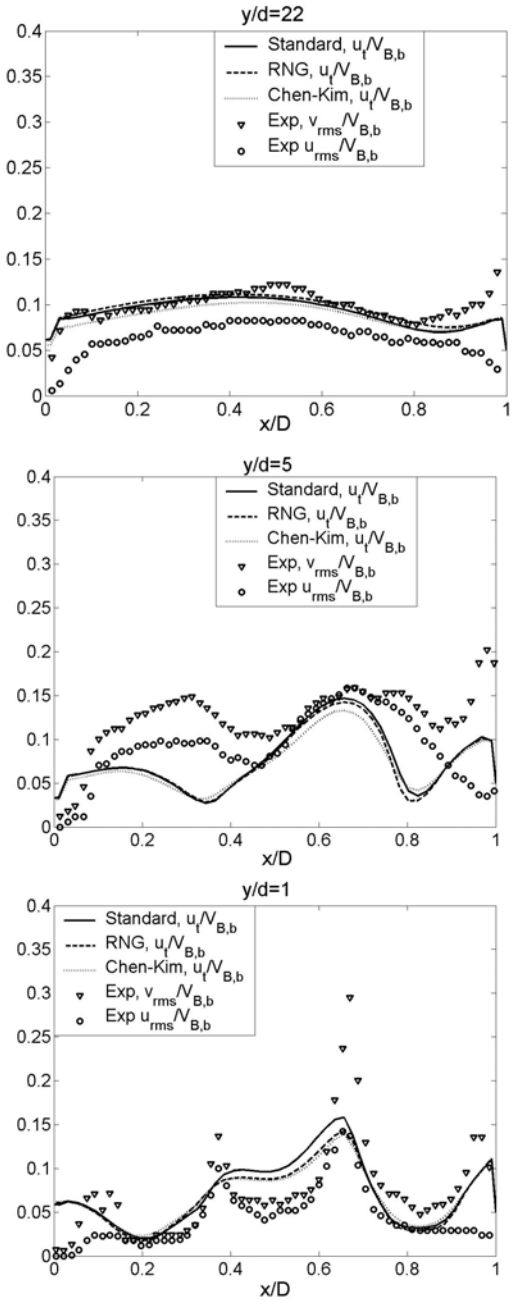

Figure 7.17: Axial(v_{rms}) and transverse (u_{rms}) velocity fluctuations compared to the turbulence velocity (u_t) at different axial positions for case 2.

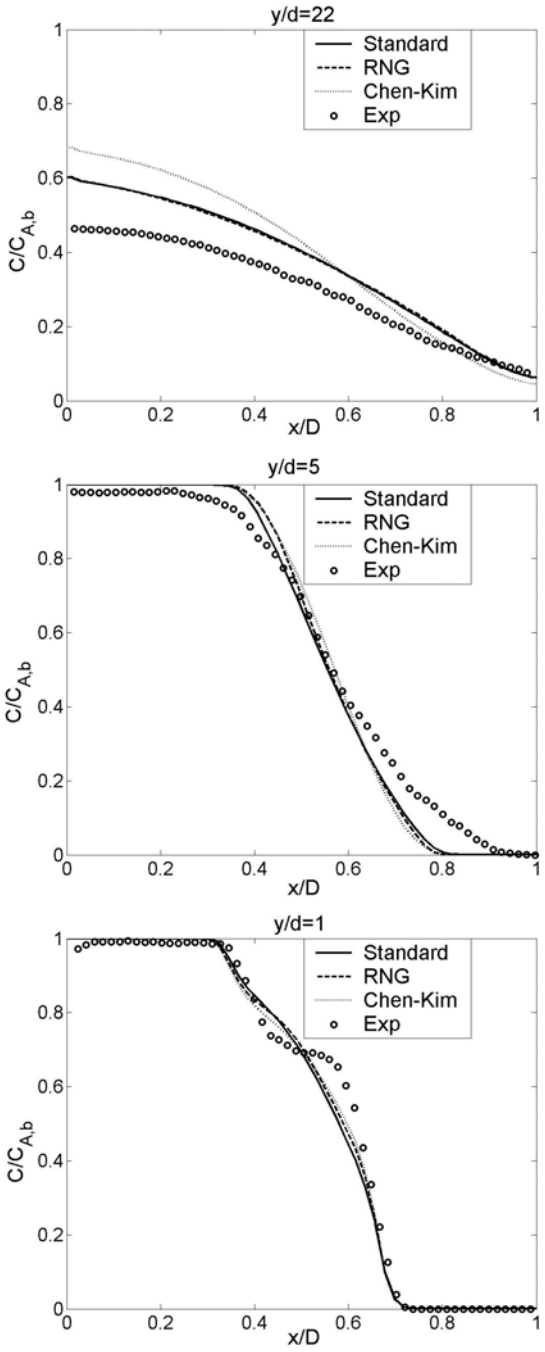

Figure 7.18: Concentration profiles from different turbulence models compared to experimental data for case 2.

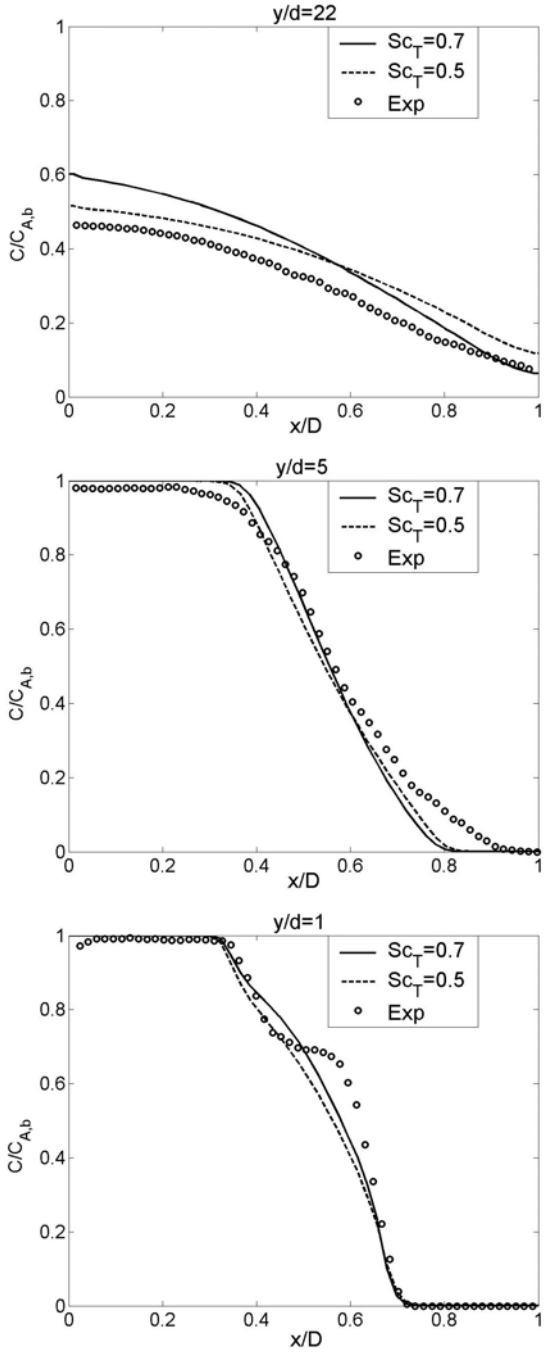

Figure 7.19: Concentration profiles from different turbulent Schmidt numbers compared to experimental data for case 2.

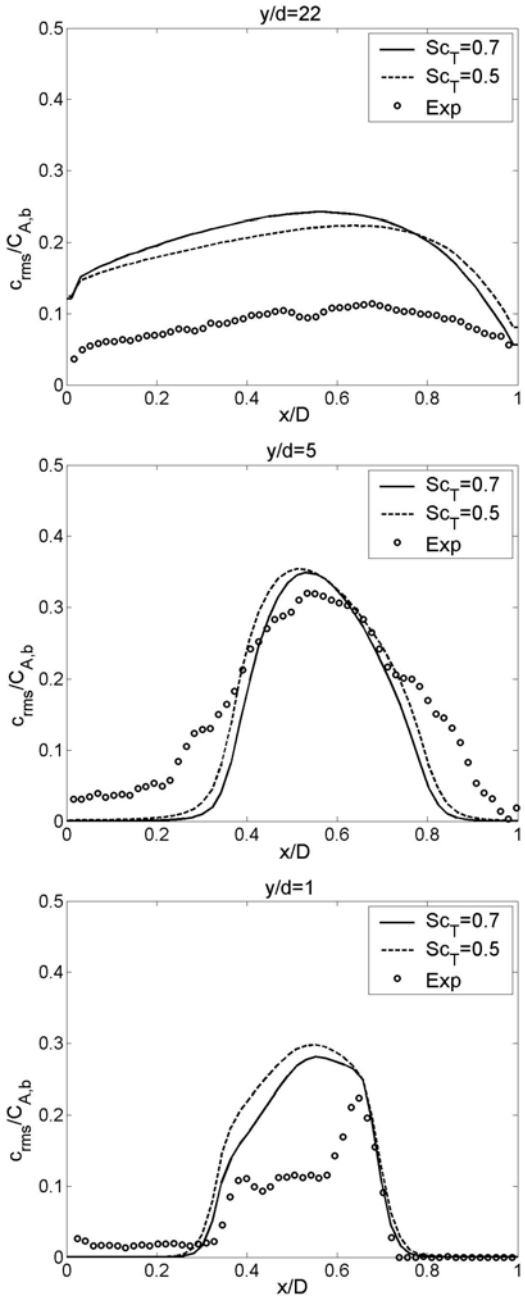

Figure 7.20: Concentration fluctuations from the MTS-model with different turbulent Schmidt numbers compared to experimental data for case 2.

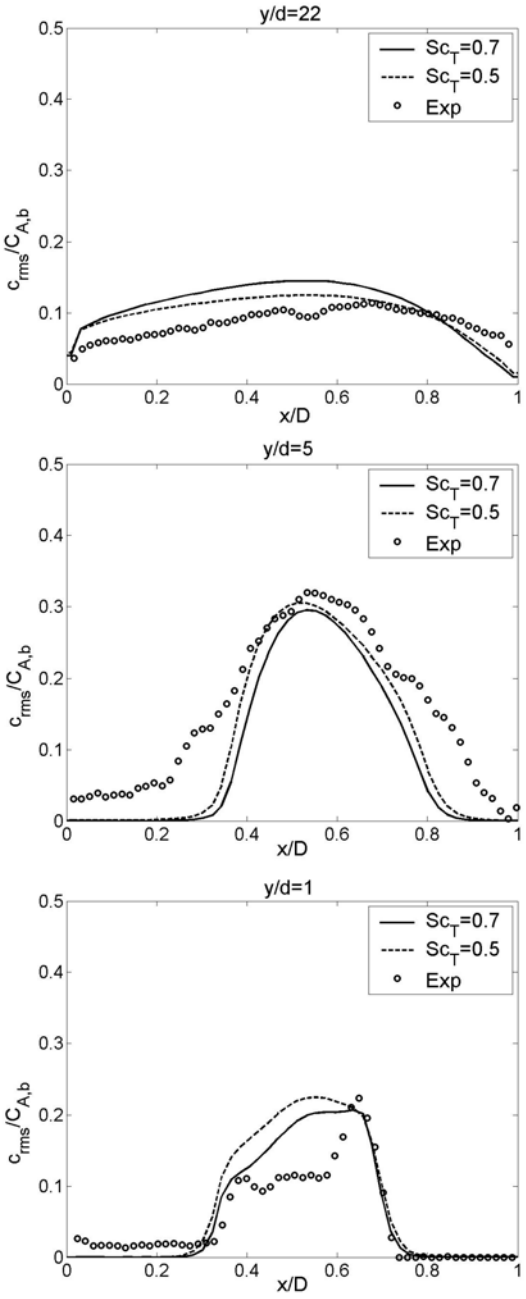

Figure 7.21: Concentration fluctuations from the 5-peak model-MMR1a with different turbulent Schmidt numbers compared to experimental data for case 2.

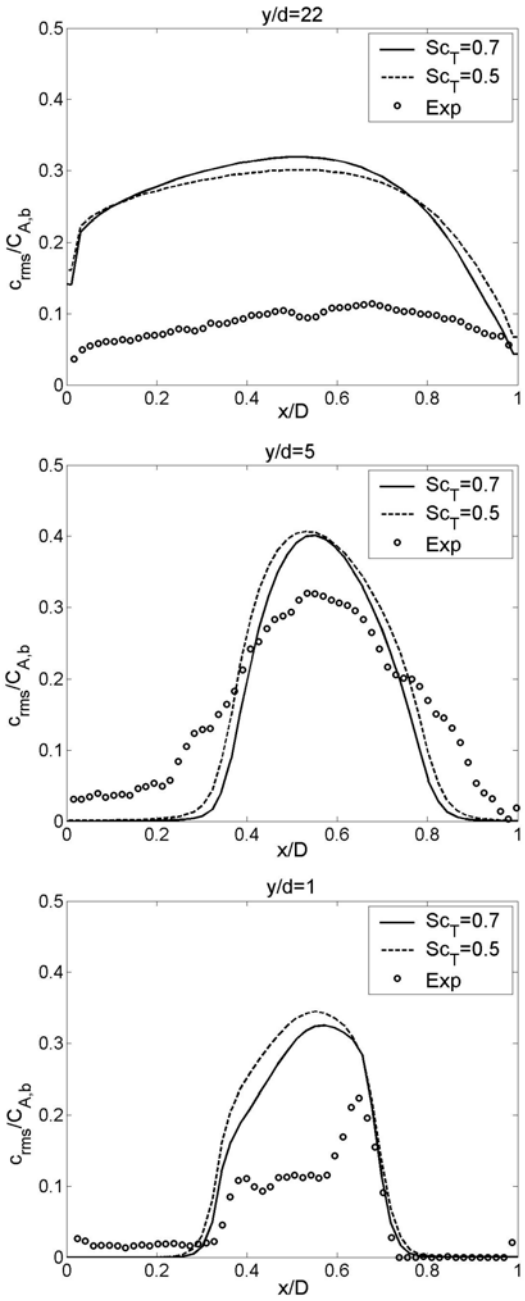

Figure 7.22: Concentration fluctuations from the 5-peak model-MMR1b with different turbulent Schmidt numbers compared to experimental data for case 2.

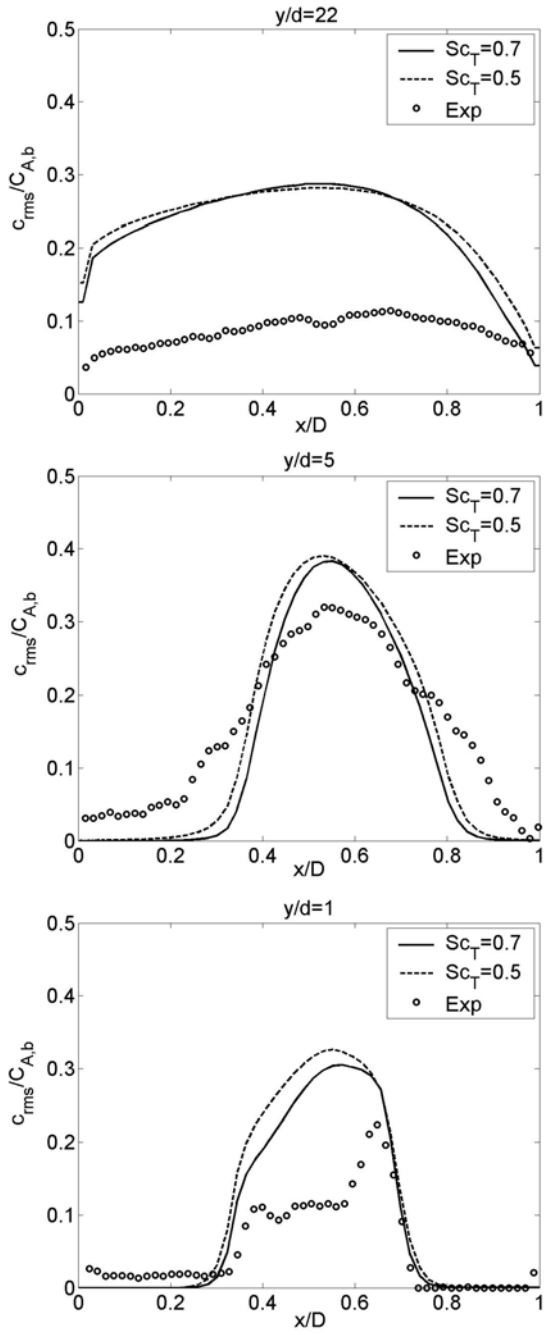

Figure 7.23: Concentration fluctuations from the 5-peak model-MMR2 with different turbulent Schmidt numbers compared to experimental data for case 2.

different turbulent Schmidt numbers are shown for the three micromixing timescales considered. The effect of reducing the Schmidt number from 0.7 to 0.5 is seen to be small.

The micromixing timescale MMR1a seems to give the best agreement between predictions and measurements. Again, when comparing the two mixing models, that is the MTS model in Figure 7.20 and the 5-peak model using MMR1a in Figure 7.21, the latter model appears to give predictions in better agreement with the experimental data.

7.4.3 Analysis of degree of mixing

Macro- and micro-mixing

The 5-peak model using MMR1a with $Sc_T = 0.50$ seemed to give the best predictions at all three axial positions for case 2. Therefore the coefficient of variation (CoV) and the decay function (d) shown in Figures 7.24 and 7.25 is from the simulations using MMR1a and $Sc_T = 0.50$.

In Figure 7.24 the predicted and measured Coefficient of variation (CoV) are plotted along the channel length. The predicted CoV fits the experimental data well.

In Figure 7.25 the predicted and measured decay function (d) are plotted along the channel length. The predicted decay function fits the experimental data well.

This supports the results seen from the mean- and fluctuating concentrations.

Probability density functions

The 5-peak model using MMR1a with $Sc_T = 0.5$ seemed to give the best predictions at all three axial positions. The PDF's shown in Figure 7.26 is therefore from the simulations using MMR1a and $Sc_T = 0.5$. Also for this case the overall agreement between the measured and predicted PDF's is quite good.

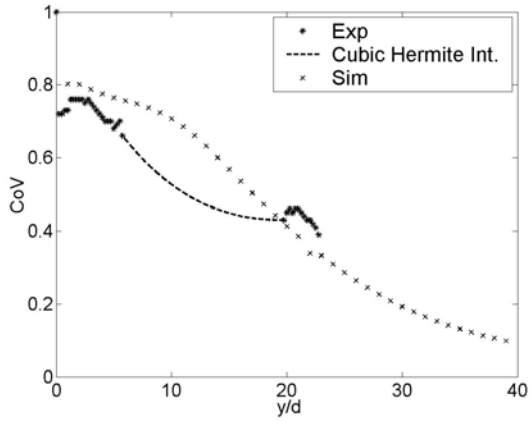

Figure 7.24: Measured and predicted Coefficient of variation for case 2.

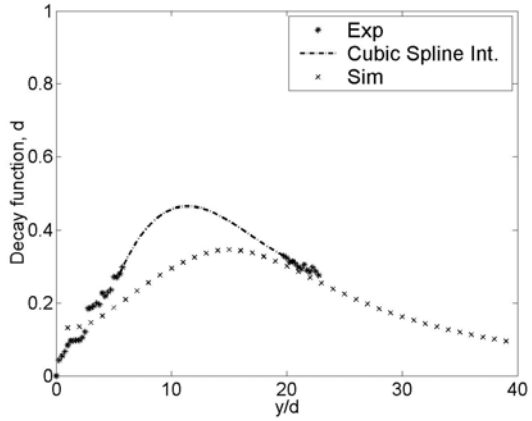

Figure 7.25: Measured and predicted decay function for case 2.

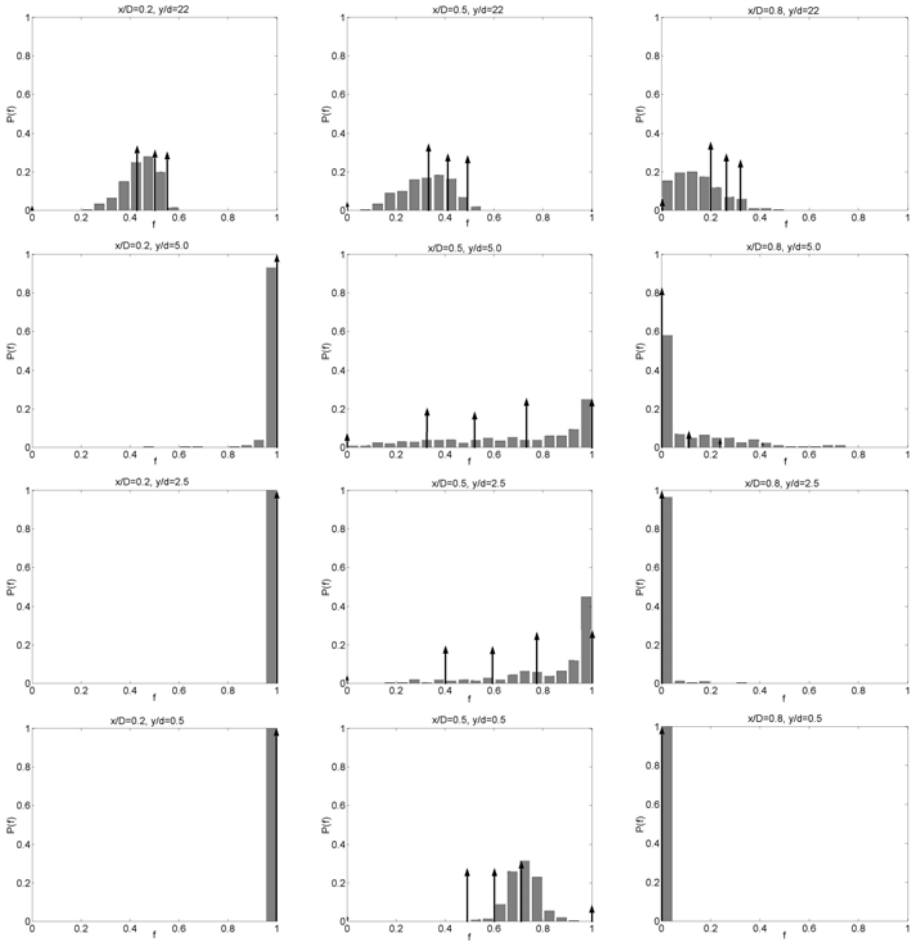

Figure 7.26: PDF's at different axial and transverse positions in the channel. ↑ - Num, 5- peak, MMR1a ▢ - Exp.

7.5 Mixing predictions for case 3, velocity ratio 0.25:1

7.5.1 Mean and fluctuating velocities

In Figures 7.27 and 7.28, axial (V) and transverse (U) velocity profiles at different axial positions for different versions of the k-ε model for case 3 are shown and compared to the experimental data. Again the different k-ε models predict almost similar profiles, except at y/d=22 where the Chen-Kim model prediction deviates a bit from the two other models. The agreement between measured and simulated velocities is reasonably good at all three axial positions. At the left side of the channel at y/d=5, backflow is observed in the experiment which is not captured by the predictions.

As shown in Figure 7.29 the predicted turbulent velocity fits well with the measured turbulent velocity fluctuations, although the levels are somewhat lower at y/d=1 and y/d=5.

7.5.2 Mean and fluctuating concentrations

In Figure 7.30, predicted mean concentration profiles for the three different k-ε-models are shown. Again, they are noted to yield very similar results. The backflow (recirculation zone) that was observed in the experiments along the left side of the mixing channel (as discussed in Chapter 3) is not captured in the predictions. Especially at y/d=1 and y/d=5 the agreement between measured and predicted concentration along the left side of the channel are not so good. At y/d=22 the predictions fits well with the experimental data. In Figure 7.31, predicted mean concentration profiles using different turbulent Schmidt Sc_T numbers are shown. The agreement between predictions and measurements is good when using a turbulent Schmidt number of $Sc_T = 0.70$, reducing it to $Sc_T = 0.50$ has no significant effect on the predicted profiles.

In Figure 7.32, predicted concentration fluctuations for the MTS model using different turbulent Schmidt numbers are shown. The MTS model is able to predict the concentration fluctuations very well. Reducing the turbulent Schmidt number from $Sc_T = 0.70$ to $Sc_T = 0.50$ gave some improvement at y/d=22. In Figures 7.33, 7.34 and 7.35, predicted

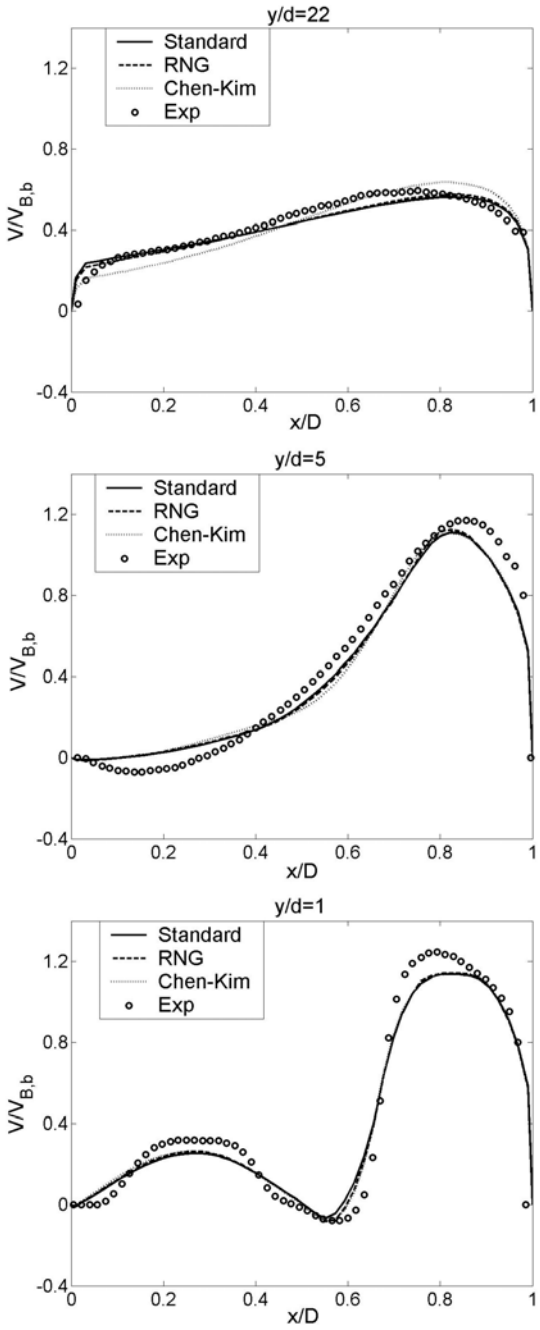

Figure 7.27: Axial (V) velocity profiles at different axial positions for case 3.

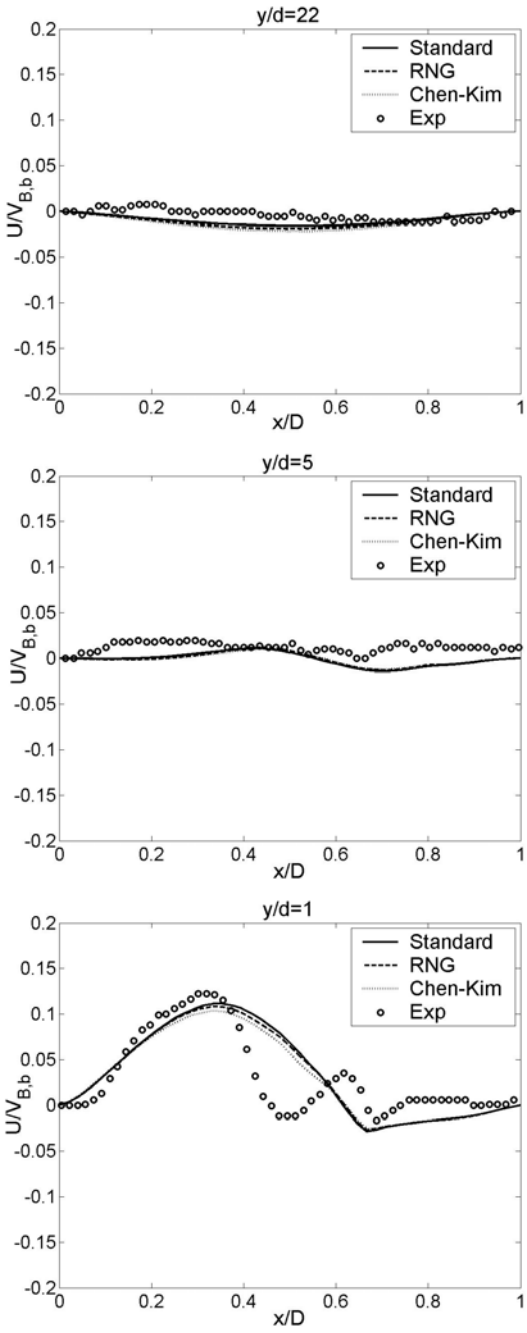

Figure 7.28: Transverse (U) velocity profiles at different axial positions for case 3.

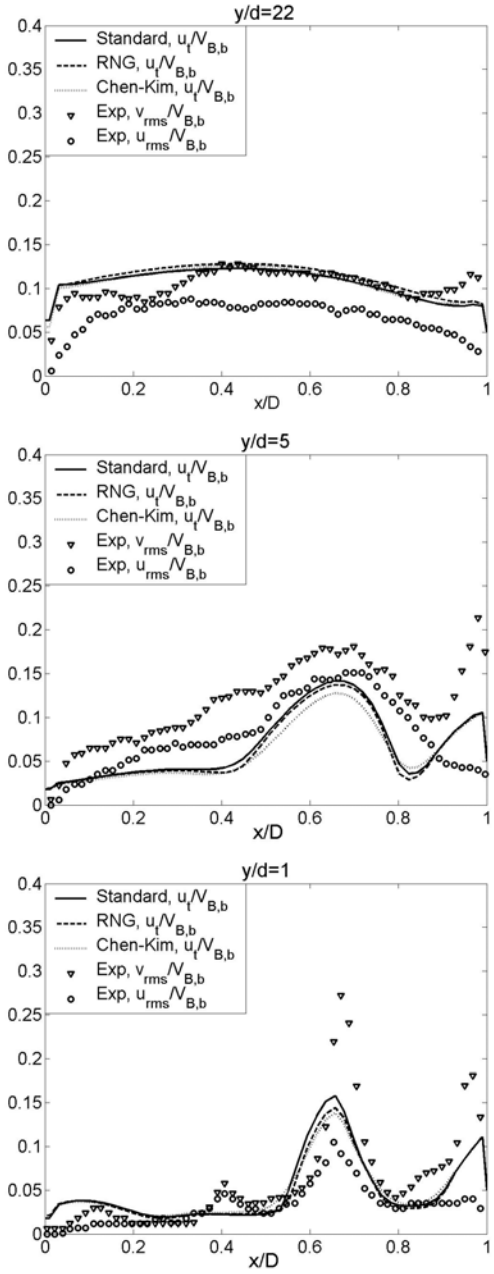

Figure 7.29: Axial(v_{rms}) and transverse (u_{rms}) velocity fluctuations compared to the turbulence velocity (u_t) at different axial positions for case 3.

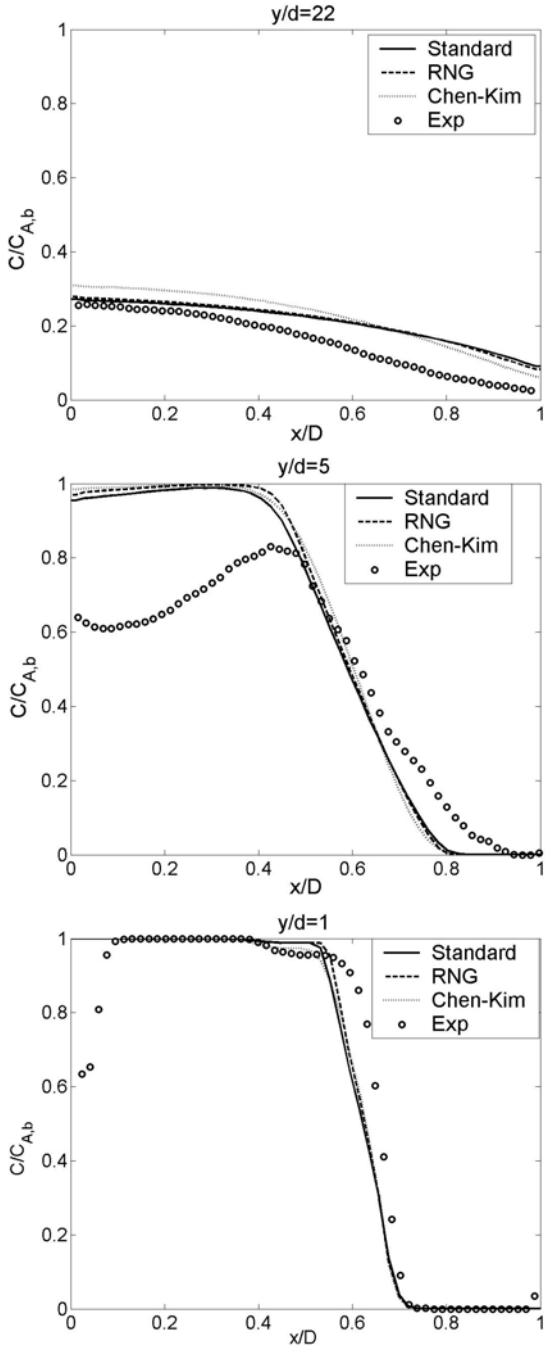

Figure 7.30: Concentration profiles from different turbulence models compared to experimental data for case 3.

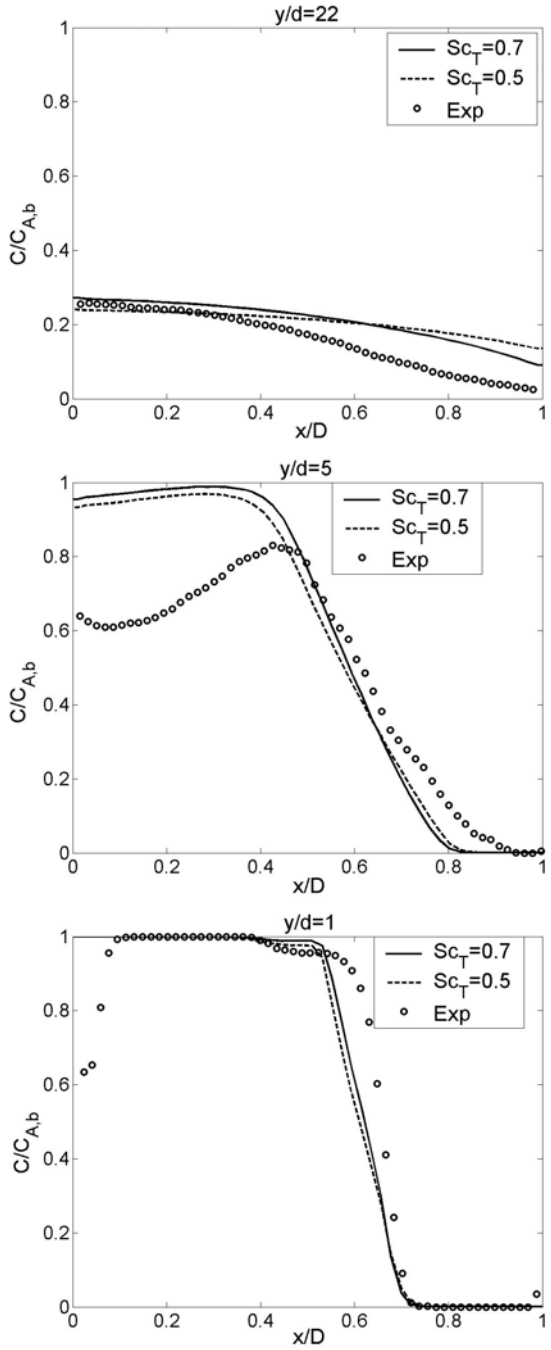

Figure 7.31: Concentration profiles from different turbulent Schmidt numbers compared to experimental data for case 3.

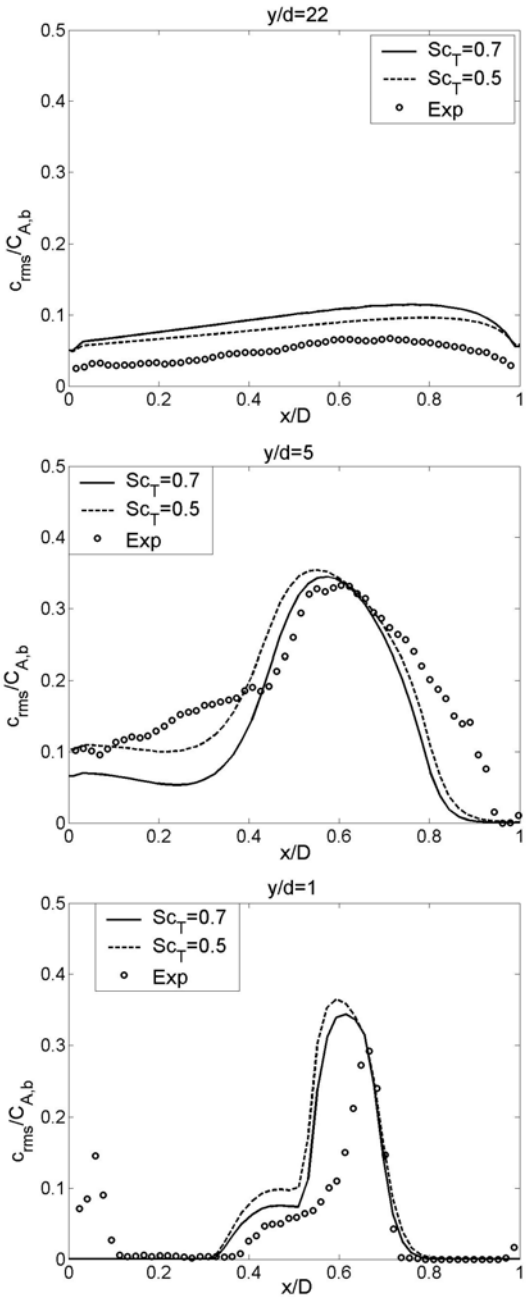

Figure 7.32: Concentration fluctuations from the MTS-model with different turbulent Schmidt numbers compared to experimental data for case 3.

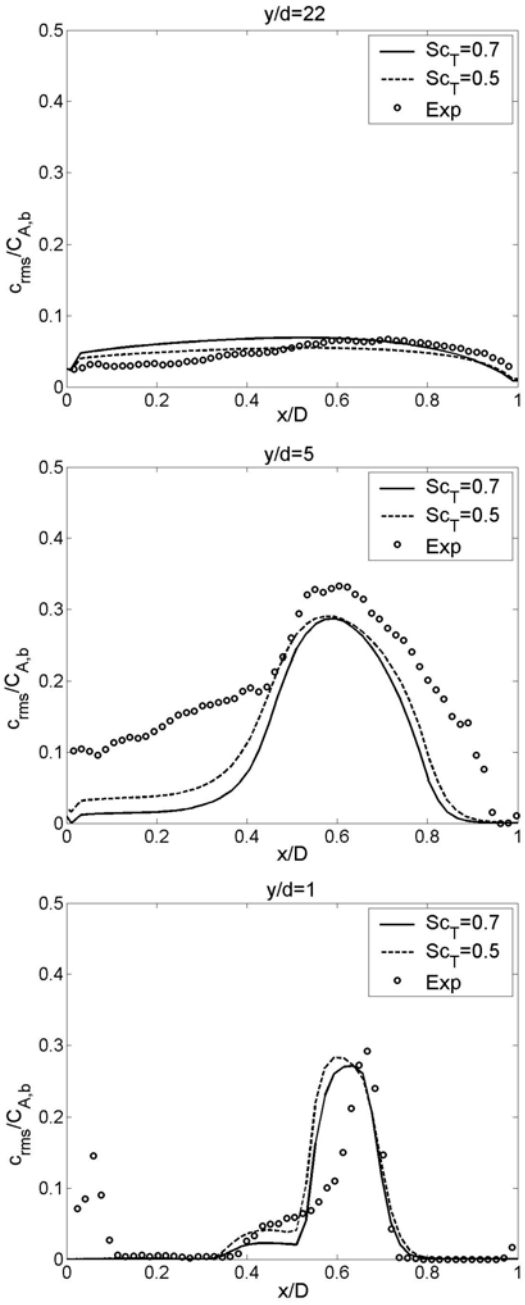

Figure 7.33: Concentration fluctuations from the 5-peak model-MMR1a with different turbulent Schmidt numbers compared to experimental data for case 3.

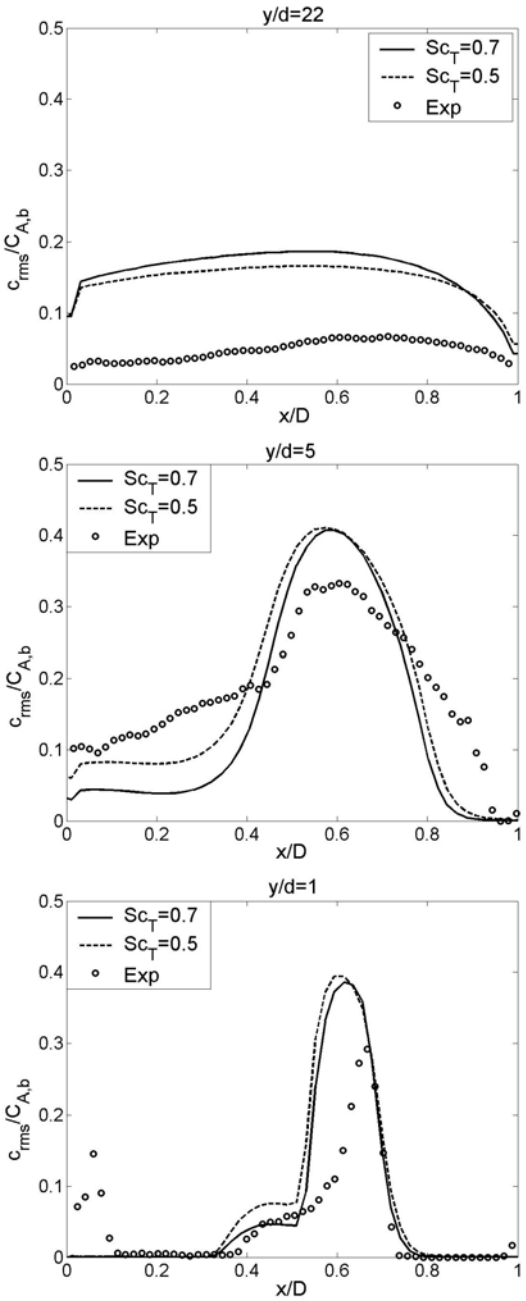

Figure 7.34: Concentration fluctuations from the 5-peak model-MMR1b with different turbulent Schmidt numbers compared to experimental data for case 3.

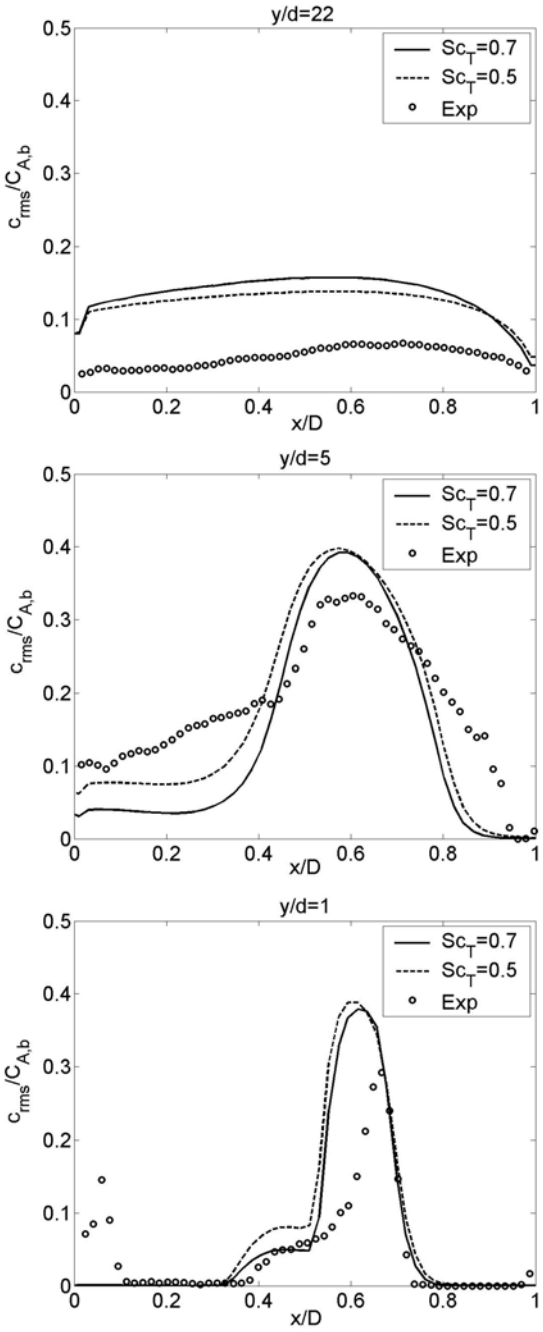

Figure 7.35: Concentration fluctuations from the 5-peak model-MMR2 with different turbulent Schmidt numbers compared to experimental data for case 3.

concentration fluctuations from the 5-peak presumed PDF model using different turbulent Schmidt numbers are shown for the three micromixing timescales considered. The effect of reducing the Schmidt number from 0.7 to 0.5 is seen to be small. The micromixing timescale MMR1a seems to give the best agreement between predictions and measurements.

Again, when comparing the two mixing models, that is the MTS model in Figure 7.32 and the 5-peak model using MMR1a in Figure 7.33, the latter model appears to give predictions in better agreement with the experimental data, even though the MTS model gave a better prediction for case 3 than for case 1 and 2.

7.5.3 Analysis of degree of mixing

Macro- and micro-mixing

The 5-peak model using MMR1a with $Sc_T = 0.50$ seemed to give the best predictions at all three axial positions for case 3. Therefore the coefficient of variation (CoV) and the decay function (d) shown in Figures 7.36 and 7.37 is from the simulations using MMR1a and $Sc_T = 0.50$.

In Figure 7.36 the predicted and measured Coefficient of variation (CoV) are plotted along the channel length. The predicted CoV is close to the experimental data from y/d=0 to y/d=6. At y/d=22 the predicted CoV under-predicts the measured one significantly.

In Figure 7.37 the predicted and measured decay function (d) are plotted along the channel length. The predicted decay function fits the experimental data quite well.

This supports the results seen from the mean and fluctuating concentration.

Probability density functions

The 5-peak model using MMR1a with $Sc_T = 0.5$ seemed to give the best predictions at all three axial positions. The PDF's shown in Figure 7.38 is therefore from the simulations using MMR1a and $Sc_T = 0.5$. At x/D=0.5 and 0.8 the overall agreement between the measured and predicted PDF's

is quite good. At x/D=0.2, which is in the recirculation zone along the wall not captured by the prediction, the agreement with between measured and predicted PDF's is not that good at all axial positions except at y/d=22. This corresponds well with the results found from the mean and fluctuating concentration in the recirculation zone along the wall.

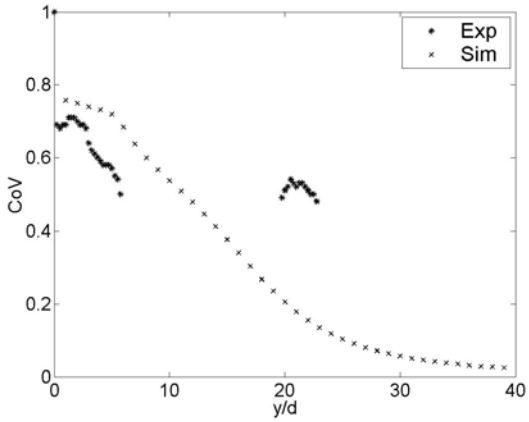

Figure 7.36: Measured and predicted Coefficient of variation for case 3.

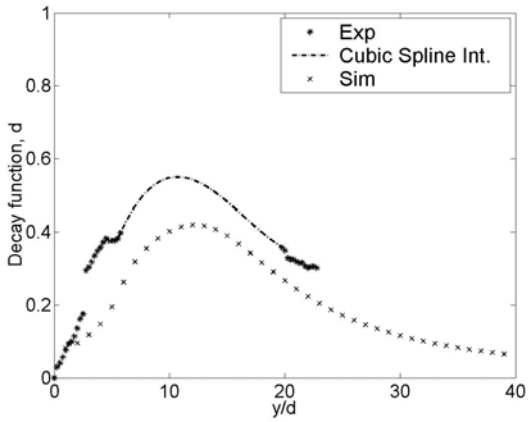

Figure 7.37: Measured and predicted decay function for case 3.

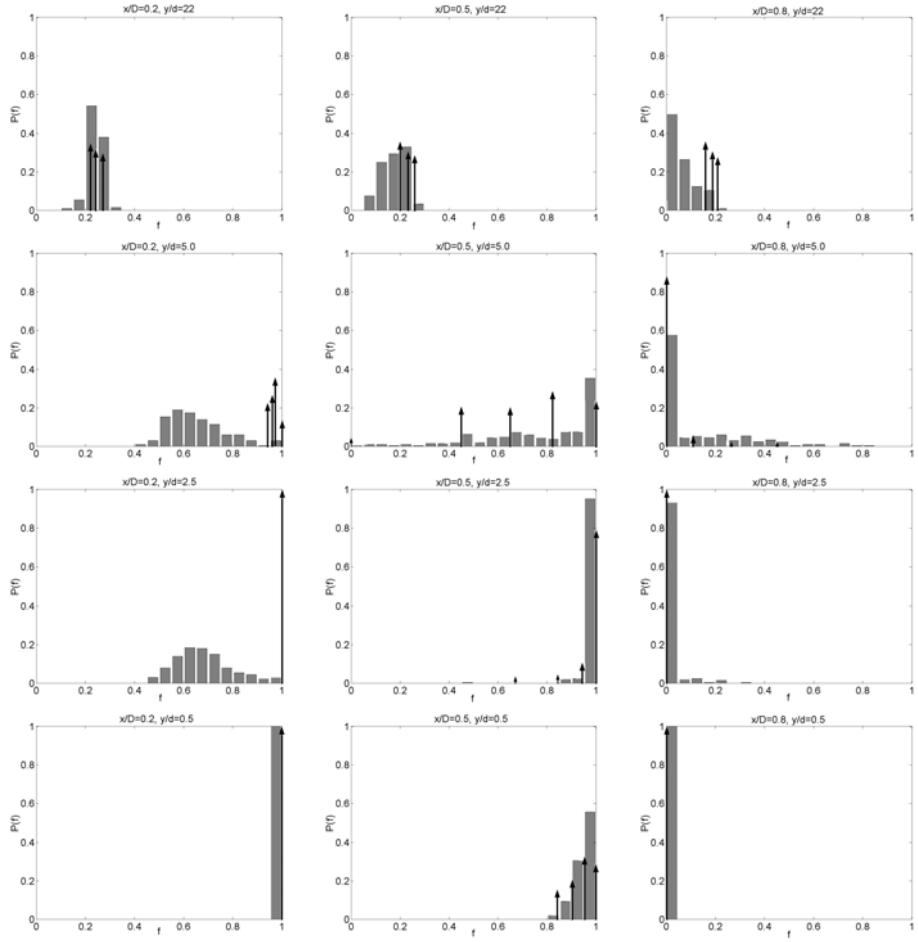

Figure 7.38: PDF's at different axial and transverse positions in the channel. ↑ - Num, 5peak, MMR1a ■ - Exp.

7.6 Concluding remarks

Three two-equation turbulent viscosity models, i.e. the standard k-ε model, the RNG k-ε model and the Chen-Kim k-ε model, and two micro-mixing models, i.e. multiple- time-scale turbulent mixer model (MTS) and the multi-peak presumed PDF model, have been validated against experimental PIV/PLIF data for turbulent mixing in a mixing channel. Three different flow cases varying the velocity ratio in the feed channels has been studied.

The different k-ε models show very little difference in predicting the velocity and concentration fields.

A comparison of predicted and measured mean and fluctuating velocities for case 1 shows that, too small turbulence levels are predicted giving consequently too small turbulent viscosity and thereby a too slow recovery of the velocity defect in the wake. In order to resolve the energetic large scale fluctuating motion in the near wake, a Large Eddy Simulation (LES) would probably be a better choice for a turbulence model than the k-ε turbulence model for case 1. In case 2 the fluctuating motion is not as large as for case 1, therefore the k-ε model give a better prediction of this flow, even though it does not capture the weak backflow along the left channel wall observed from the measurements. The backflow that appeared in the measurement for case 3 is not correctly captured by the predictions either. It seems that LES would be a better choice also for case 2 and 3.

A comparison of predicted and measured mean concentration for case 1 shows that the concentration like the velocity exhibits a too slow recovery in the wake. However, the growth rate of the concentration wake can be improved by reducing the turbulent Schmidt number from the standard value $Sc_T = 0.70$ to $Sc_T = 0.15$. The prediction of the mean concentration for case 2 is good using a turbulent Schmidt number of $Sc_T = 0.70$, however reducing it to $Sc_T = 0.50$ gave some improvement. The mean concentration predicted for case 3 along the left side of the channel does not fit well with experimental data. Reducing the turbulent Schmidt number does not have a significant effect on the results for this case.

The micro-mixing models depend strongly on the mean and turbulent velocities as well as the mean concentration. Accordingly, micro-mixing models show a similar improvement in the prediction of the concentration fluctuations by reducing the Schmidt number as for the predictions of the mean concentration. For the 5-peak model, two different micro-mixing rates are investigated. The predictions with the micro-mixing rate denoted MMR1a, which is a simple large-scale dominated model show the best agreement with measurements for all three flow cases. Comparing the MTS and the 5-peak micro-mixing models, the latter model predicts the concentration fluctuations in better agreement with the experimental data for all three flow cases.

The accuracy of the predicted PDF's is strongly dependent on the accuracy of the predicted mean concentration and its fluctuations. Still, the overall agreement between predicted and the measured PDF's is quite good, except for the backflow along the left channel wall for case 3.

Chapter 8

Simulations of fast chemical reaction

8.1 Introduction

In Chapter 4, measurements of product concentration in a mixing channel for two different flow cases were presented. These measurements will in this chapter be used to evaluate numerical simulations of that flow. The product concentration will be evaluated to test the performance of two different reaction models.

8.2 Numerical configuration

The numerical configuration is the same as described in Chapter 7.2, except that in this case only flow case 1 and 2 are considered. In addition Acid and Base are introduced through the two feed channels, as described in Chapter 4.

The reaction is modelled by the use of the two different reaction models: the multi-peak presumed PDF with 5 environments (referred to here as 5-peak presumed PDF model) and the Eddy Dissipation Concept (EDC). These models were presented in Chapter 5.5.3 and 5.4.1, respectively.

The measured product concentration presented in Chapter 4 is conditioned on $v_b \geq 0.5$, meaning that there is only measured product when the concentration of base is in excess. This has been taken account for in

the predictions where the 5-peak presumed PDF model was used to be able to compare the predictions with the experimental data.

The Standard EDC and the EDC-MTS model have also been tested. In these models it is not possible to take into account that the measured product concentration is conditioned on $v_b \geq 0.5$. Therefore the performance of these models is tested against the performance of the multi-peak presumed PDF model without taking account for $v_b \geq 0.5$.

For both the standard EDC and the EDC-MTS model, the reaction rate constant A=1. This has been found to give the best fit for liquid reactions (from Tsai et al. (2002) and from the results given in Chapter 6).

8.3 Predictions for case 1, velocity ratio 1:1

8.3.1 Multi-peak presumed PDF model

The predictions of passive mixing in Chapter 7 indicated that a turbulent Schmidt number Sc_T = 0.15 and the micro-mixing timescale denoted MMR1a gave the best agreement with measured mean and fluctuating concentration in case 1. These parameters are therefore also used when the reaction models for the corresponding reactive mixing in case 1 is evaluated.

In Figure 8.1, the predicted mean product concentration along the centreline for case 1 is shown. The amount of product predicted in the recirculation zone and at y/d=30 is noted to be smaller than the measured one. From y/d=1.5 to 10 the amount of product predicted is higher than the measured one. From y/d=10 to 22 there is good agreement between experimental and simulated results.

In Figure 8.2, the predicted mean product concentration profiles at three different axial positions for case 1 are shown. The predictions at y/d=1 and 22 are seen to be good. Some discrepancies are, however, noted at y/d=5. This corresponds with what was found for the passive mixing predictions of case 1 in Chapter 7.

From the results given in Figures 8.1 and 8.2 it can be concluded that the 5-peak presumed PDF model gives a good estimate of the reaction.

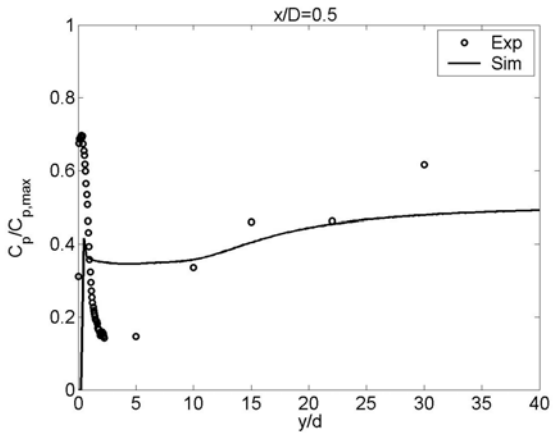

Figure 8.1: Mean product concentration from the 5-peak model along the centreline compared to experimental data for case 1.

8.3.2 Eddy Dissipation Concept

In Figure 8.3, the mean product concentration from the 5-peak presumed PDF model is compared to the results from the standard EDC model and the EDC-MTS model. The standard EDC model predicts a higher amount of product than the 5-peak presumed PDF model, at all three axial positions. The EDC-MTS model predicts results close to the 5-peak presumed PDF model at y/d=1 and 5.

As seen in Figure 8.2 the 5-peak presumed PDF model had a tendency to predict a higher amount of product than the measured one at y/d=1 and 5. Since both the standard EDC and the EDC-MTS model predicts even higher product concentration, as seen in Figure 8.3, it can be concluded that the 5-peak presumed PDF model gives the best prediction of the reaction. The EDC-MTS model gives similar results as the 5-peak presumed PDF model. The discrepancies between the results obtained with the standard EDC model and the 5-peak presumed PDF model indicates that the standard EDC model is not a suitable model for the reactive flow considered here.

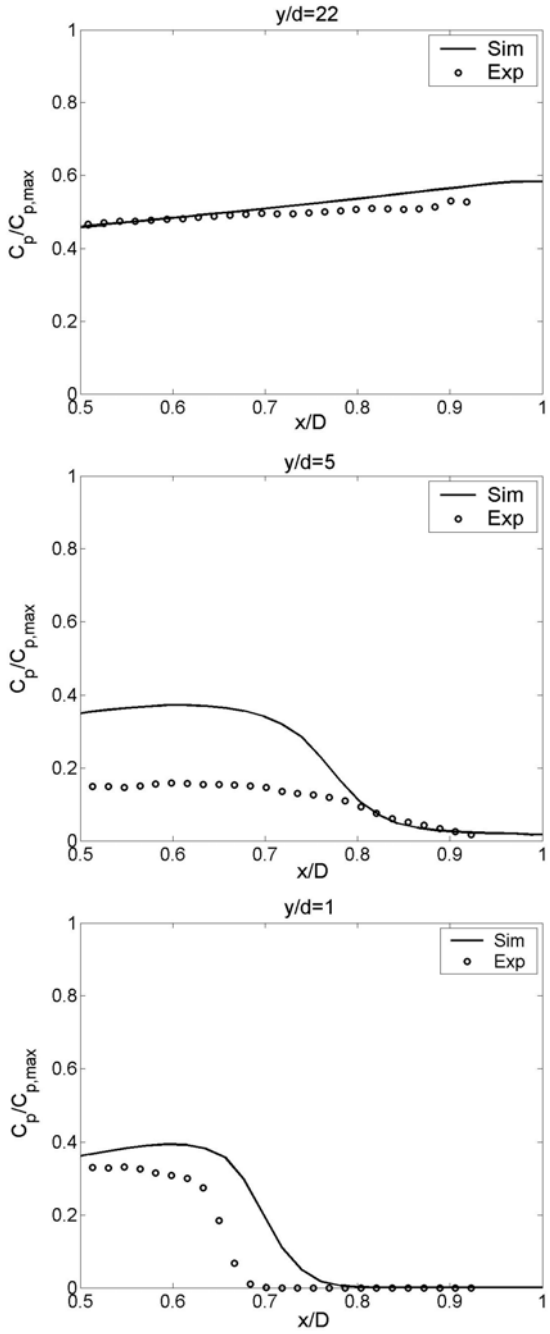

Figure 8.2: Mean product concentration profiles from the 5-peak model compared to experimental data for case 1.

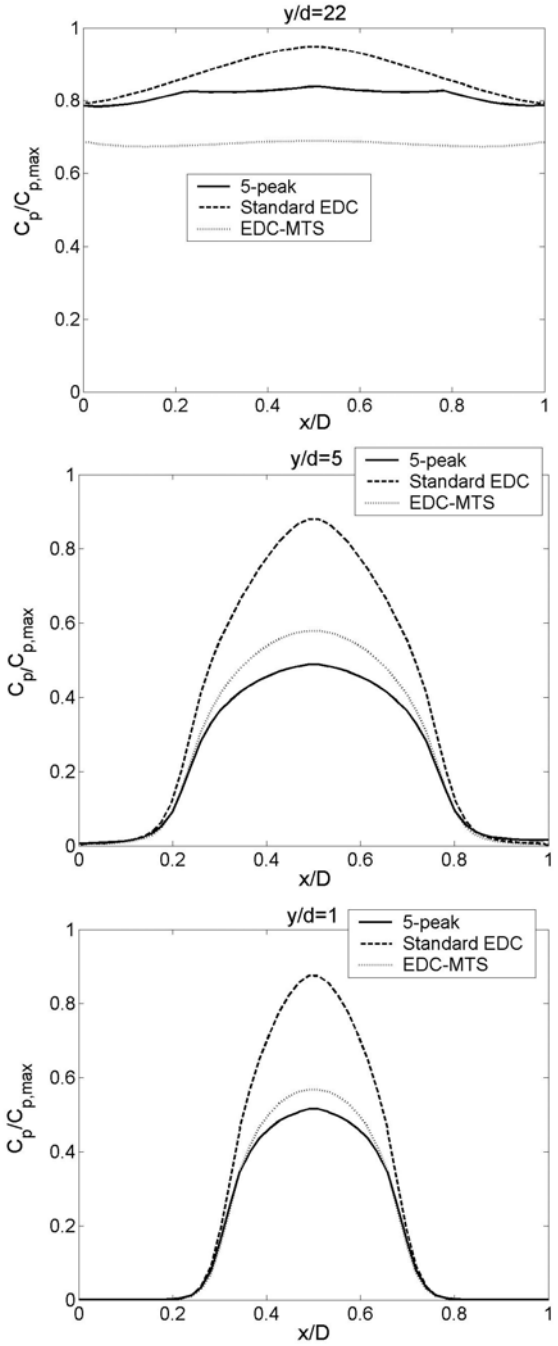

Figure 8.3: Mean product concentration from the 5-peak model compared to the results from the standard EDC model and the EDC-MTS model for case 1.

8.4 Predictions for case 2, velocity ratio 0.5:1

8.4.1 Multi-peak presumed PDF model

The predictions of passive mixing in Chapter 7 indicated that a turbulent Schmidt number Sc_T = 0.5 and the micro-mixing timescale denoted MMR1a gave the best agreement with measured mean and fluctuating concentration in case 2. These parameters are therefore also used when the reaction models for the corresponding reactive mixing in case 2 are evaluated.

In Figure 8.4, the predicted mean product concentration along the centreline for case 2 is shown. It can be seen that the amount of product predicted from y/d=0 to 15 is higher than the measured one. From y/d=15 there is good agreement with experimental data.

In Figure 8.5, the predicted mean product concentration profiles at three different axial positions for case 2 are shown. It can be seen that the prediction at y/d=22 is good, at y/d=1 and 5 there are some discrepancies. This corresponds with what was found for the passive mixing predictions of case 2 in Chapter 7.

From the results given in Figures 8.4 and 8.5, it can again be concluded that the 5-peak presumed PDF model gives a good estimate of the reaction.

8.4.2 Eddy Dissipation Concept

In Figure 8.6, the product concentration from the 5-peak presumed PDF model is compared to the results from the standard EDC model and the EDC-MTS model. The product concentration predicted with the standard EDC model is higher than the results obtained with the 5-peak presumed PDF model and the EDC-MTS model. There is good agreement between the results obtained with the EDC-MTS and the 5-peak presumed PDF model at y/d=1 and 5.

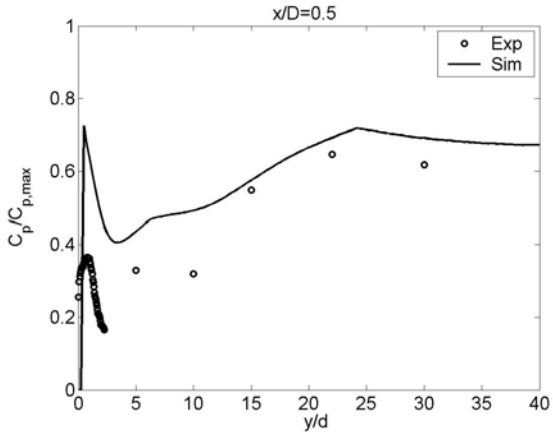

Figure 8.4: Mean product concentration from the 5-peak model along the centreline compared to experimental data for case 2.

As seen from Figure 8.5 the 5-peak presumed PDF model has a tendency to predict higher product concentration at y/d=1 and 5 than the measured one. Since both the standard EDC and the EDC-MTS model predicts even higher product concentration, as seen from Figure 8.6, it can again be concluded that the 5-peak presumed PDF model gives the best prediction of the reaction. The EDC-MTS model gives similar results as the 5-peak presumed PDF model. The discrepancies between the results obtained with the standard EDC model and the 5-peak presumed PDF model again indicates that the standard EDC model is not a suitable model for the reactive flow considered here.

8.5 Concluding remarks

Two reaction models, i.e. the multi-peak presumed PDF model and two versions of the Eddy dissipation Concept, namely the standard EDC model and the EDC-MTS model, have been validated against experimental reactive-PLIF data for turbulent reactive mixing in a mixing channel. Two flow cases have been considered.

A comparison of predicted and measured mean product concentration for flow case 1 and 2 using the 5-peak presumed PDF model showed that the predicted product concentration is somewhat higher in the initial mixing zone. The prediction further out in the channel is quite good.

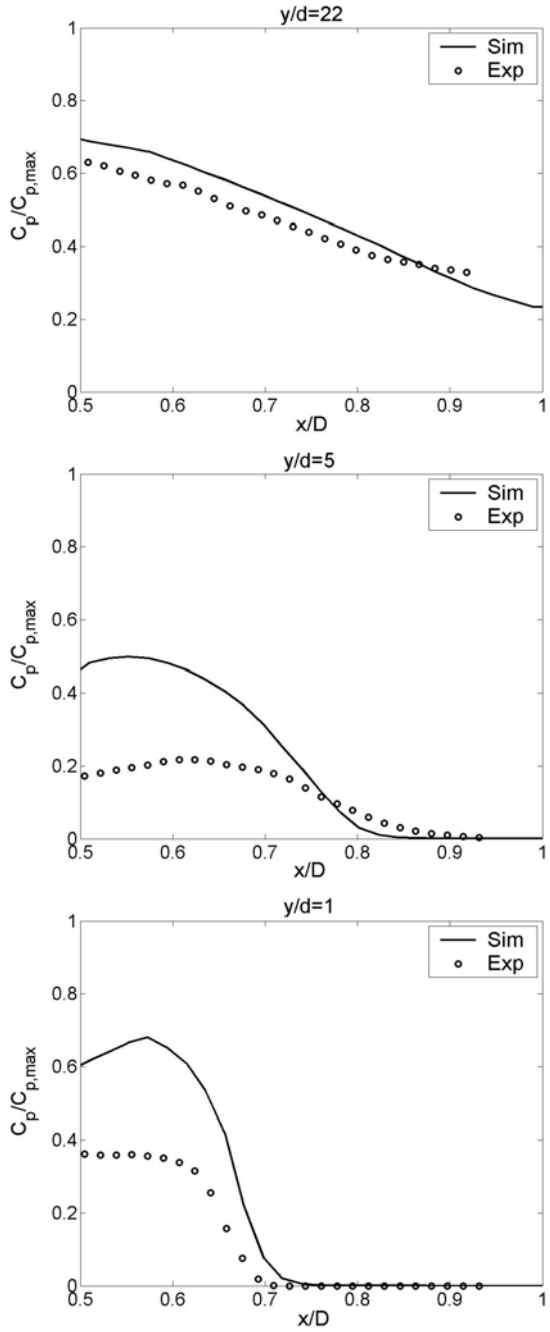

Figure 8.5: Mean product concentration from the 5-peak model compared to experimental data for case 2.

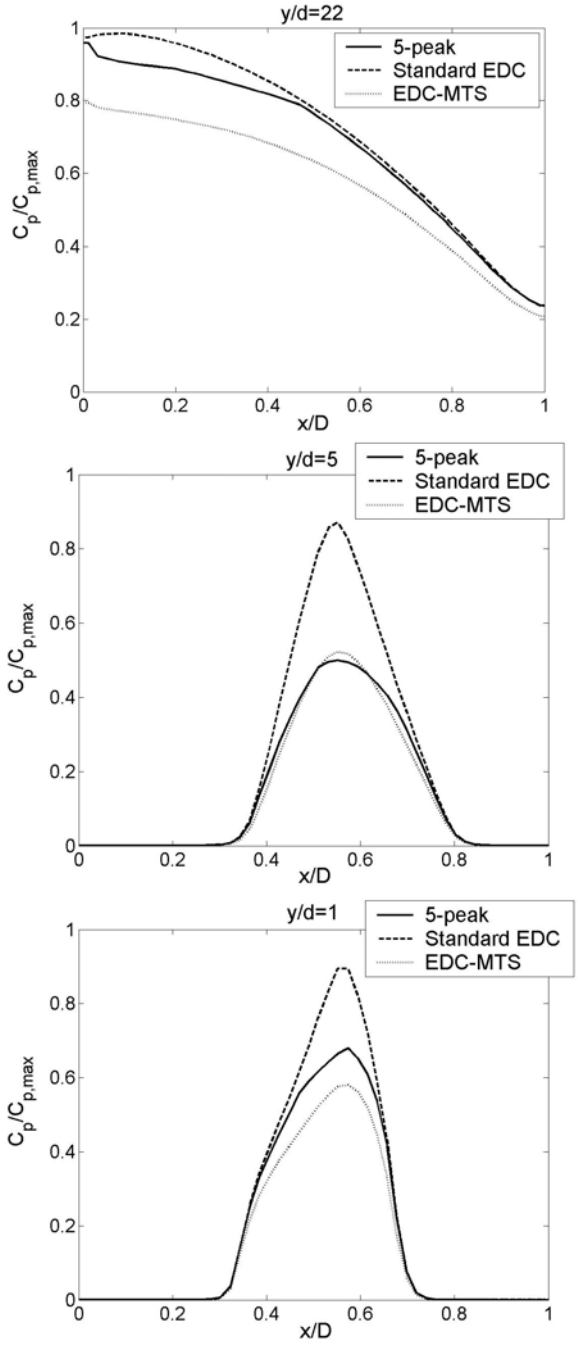

Figure 8.6: Mean product concentration profiles from the 5-peak model compared to the results from the standard EDC model and the EDC-MTS model for case 2.

The 5-peak presumed PDF model and the EDC-MTS model shows similar results. The 5-peak presumed PDF model is considered to be the best model for the reactive flow cases considered here. The standard EDC model is not considered to be applicable for the cases considered here.

This corresponds well with what was found in Chapter 6 when evaluating different versions of the EDC-model.

The reason why the 5-peak model performs better than the EDC-MTS model could be that the 5-peak model uses local concentrations in the reaction rate expression compared to the averaged concentration used in the EDC-MTS model.

Chapter 9

Conclusions and Recommendations

The objective of this thesis is to provide experimental data as well as to validate CFD models for passive and reactive mixing in a mixing channel for different flow cases.

9.1 Conclusions

9.1.1 Experimental part

In Chapter 3 experimental studies are conducted in a mixing channel with different inlet velocity ratios. The combined PIV/PLIF technique is used to measure velocity and concentration.

For the case with an inlet velocity ratio of 1:1 (case 1), the measurements reveals a backflow (recirculation zone) in the area behind the block and the flow acts as a wake. The backflow gives an increased mixing effect which results in a uniform concentration distribution in this area. Large scale transverse velocity fluctuations are also observed. PDF's at different positions in the flow shows that the concentration is more uniform behind the block than further out in the channel.

For the case with an inlet velocity ratio of 0.5:1 (case 2), the mixing in the recirculation zone is found to be less effective than in case 1. The transverse velocity fluctuations are also less which causes less transverse

spreading of species concentration. A weak backflow along the left side of the channel is identified and this indicates that there is a transition from a wake flow to a backward facing step in this case. Compared to case 1, the PDF's indicates that the transverse spreading is smaller and there is more spreading towards the inlet with the higher velocity.

For the case with an inlet velocity ratio of 0.25:1 (case 3), the mixing in the recirculation zone is found to be even less effective than in case 2. The measurements for case 3 also show a backflow along the left channel wall that is much stronger than the one identified in case 2. The flow seems to act almost as a backward facing step. From the PDF's it is found that the flow in case 3 is better mixed along x/D=0.2 than in the other two cases. However, the mixing along x/D=0.5 and 0.8 is worse compared to case 1 and 2.

Chapter 4 is concerned with reactive mixing. The product concentration from an acid-base reaction is measured using a reactive-PLIF technique. The measurements reveal that an increased amount of product is formed in the recirculation zone that is identified from the mixing experiments. The amount of product formed is shown to be dependent on how well the two streams are mixed. This corresponds well with the fact that the reactants have to be mixed on a molecular level before the reaction occurs.

9.1.2 Numerical part

In Chapter 6, numerical predictions of a tubular reactor are evaluated against the predictions of Hannon et al. (1998) and the experimental findings of Baldyga et al. (1983). The standard EDC-model is not able to correctly predict the experimental results. The first modification denoted the EDC-SDT-model, in which the time scale of fluid dynamic dissipation is replaced with the time scale of scalar dissipation, does not improve the results significantly. The second modification denoted the EDC-MTS model, which accounts for multiple time scales, gives results that are comparable to the experimental results. Both the double peak and the beta PDF model predict a too short reaction-zone length.

Both turbulence and mixing models are evaluated in Chapter 7 against the experimental passive mixing data found in a mixing channel with

different inlet velocity ratios. The different k-ε models show very little difference in predicting the velocity and concentration fields.

For the case with an inlet velocity ratio of 1:1 (case 1), comparison of predicted and measured mean and fluctuating velocities shows that the turbulence levels are predicted too low. This consequently gives a too small turbulent viscosity and thereby too slow recovery of the velocity defect in the wake. In order to resolve the energy-containing large scale fluctuating motion in the near wake, a Large Eddy Simulation (LES) will probably be a better choice for a turbulence model than the k-ε turbulence model for case 1. For the case with an inlet velocity ratio of 0.5:1 (case 2), the fluctuating motion is not as large as for case 1. Therefore, the k-ε model appears to give better prediction of this flow, even though the weak backflow along the left channel wall observed in the measurements is not captured. For the case with velocity ratio of 0.25:1 (case 3), the even stronger backflow that appears in the measurement is not correctly captured by the predictions either. LES seems to be a better choice for a turbulence model in all the three cases.

A comparison of predicted and measured mean concentrations for case 1 shows that the concentration, like the velocity, exhibits a too slow recovery in the wake. However, the growth rate of the concentration wake is improved by reducing the turbulent Schmidt number from the standard value $Sc_T = 0.70$ to $Sc_T = 0.15$. The prediction of the mean concentration for case 2 is good using a turbulent Schmidt number of $Sc_T = 0.70$. Reducing it to $Sc_T = 0.50$ gives some improvement. The mean concentration predicted for case 3 along the left side of the channel does not fit well with experimental data. Reducing the turbulent Schmidt number does not have a significant effect on the results for this case.

The micro-mixing models depend strongly on the mean and turbulent velocities as well as the mean concentration. Accordingly, micro-mixing models show a similar improvement in the prediction of the concentration fluctuations by reducing the Schmidt number as for the predictions of the mean concentration. For the 5-peak model, two different micro-mixing rates are investigated. The predictions with the micro-mixing rate denoted MMR1a, which is a simple large-scale dominated model, shows the best agreement with measurements for all three flow cases. Comparing the MTS and the 5-peak micro-mixing models, the latter model predicts the

concentration fluctuations in better agreement with the experimental data for all three flow cases.

The accuracy of the predicted PDF's is strongly dependent on the accuracy of the predicted mean concentration and its fluctuations. Still, the overall agreement between predicted and the measured PDF's is found to be quite good, except for the backflow along the left channel wall for case 3.

In Chapter 8 the reaction models are evaluated against the experimental reactive mixing data. A comparison of predicted and measured mean product concentration for flow case 1 and 2 using the 5-peak presumed PDF model shows that the predicted product concentration is somewhat higher in the initial mixing zone. The prediction further out in the channel is quite good.

The 5-peak presumed PDF model and the EDC-MTS model show similar results. The 5-peak presumed PDF model is considered to be the best model for the reactive flow cases considered here. The standard EDC-model is not considered to be applicable. This corresponds well with what is found when evaluating different versions of the EDC-model for a tubular reactor.

9.2 Recommendations for future work

In order to evaluate the performance of the mixing and reaction models more experimental data is needed for different flow cases, geometries and reactions. Especially, more precise reactive measurements are needed.

In order to resolve the energetic large scale fluctuating motion in the near wake, a Large Eddy Simulation (LES) would probably be a better choice for a turbulence model, than the k-ε turbulence model for the flow cases considered here. Further testing of the beta-PDF model against the multi-peak model and experimental data would also be of interest.

Bibliography

Aanen, L., A. Telesca and J. Westerweel (1999). 'Measurement of turbulent mixing using PIV and LIF'. *Machine Graphics & Vision* **8**, 529-543.

Bakker, A., R. D. LaRoche and E.M. Marshall. (1998). Laminar Flow in Static Mixers with Helical Elements', The online CFM Book, http://www.bakker.org/cfm.

Baldyga, J. (1989). 'Turbulent mixer model with application to homogeneous, instantaneous chemical reactions'. *Chem. Eng. Sci.* **44**, 1175-1182.

Baldyga, J., M. Henczka and W. Orciuch (1997). Closure problem for mixing and precipitation in inhomogeneous turbulent flow. In 'Proceedings of the symposium on Crystallization and Precipitation', Lappeenranta, Finland, pp.41-43.

Baldyga , J. and W. Orciuch (1999). Closure method for precipitation in inhomogeneous turbulence. In 'Proc. 14th Int'l Symp. Industr. Cryst.', Cambridge UK, pp. 1069-1080.

Baldyga, J. and J.R Bourne (1999). *Turbulent mixing and chemical Reactions*. John Wiley & Sons.

Baldyga , J. and W. Orciuch (2001). 'Barium sulphate precipitation in a pipe – an experimental study in CFD modelling'. *Chemical Engineering Science* **56**, 2453-2444.

Bird, R., B., W. E. Stewart and E. N. Lightfoot (2002). *Transport Phenomena*, second edition. John Wiley & Sons, Inc..

Borg, A., J. Bolinder and L. Fuchs (2001). 'Simultaneous velocity and concentration measurements in the near field of a turbulent low-pressure jet by digital particle image velocimetry-planar laser-induced fluorescence'. *Exp Fluids* **3**, 140-152.

Corrsin, S. (1964). 'The Isotropic Turbulent Mixer: Part II. Arbitrary Schmidt number'. *AIChE Journal* **10**, 870-877.

Dantec Measurement Technology (2001). FlowMap PIV Installation and User's guide. Dantec Measurement Technology, Denmark.

Fissore, D., D.L Marchisio and A.A. Barresi (2002). 'On the Comparison between Probability Density Function Models for CFD Applications'. *The Canadian Journal of Chemical Engineering* **80**, 710-720.

Fox, R.O. (1998). 'On the relationship between Lagrangian micromixing models and computational fluid dynamics'., *Chem. Eng. and Processing* **37**, 521-535.

Fox, R.O. (2000). CFD models for turbulent reacting flows, Class notes for Summerschool/PhD Course at Aalborg University Esbjerg, Denmark, August 2000, Iowa State University, USA.

Fukushima C., L. Aanen and J. Westerweel (2000). Investigation of the Mixing Process in an Axisymmetric Turbulent Jet Using PIV and LIF. 10th Int. Symp. on Application of Laser Techniques to Fluid Mech., 10-13 July, Lisbon, Portugal.

Guillard, F. (1999). Mixing patterns in rushton-turbine-agitated reactors, PhD-Thesis, Lund University, Sweden.

Hannon, H., Hearn, S., Marshall, L. & Zhou, W. (1998). Assessment of CFD approaches to predicting fast chemical reactions. Prepared for Presentation at the 1998 Annual Meeting, Miami Beach, FL, USA, Nov. 15-20.

He, G., Y. Guo and T. Hsu (1999). 'The effect of Schmidt number on turbulent scalar mixing in a jet-in-crossflow'. *Int. Jour. of Heat and Mass Transfer* **42**, 3727-3738.

Hjertager, L.K., B.H. Hjertager, N.G. Deen and T. Solberg (2003). 'Measurement of turbulent mixing in a confined wake flow using combined PIV and PLIF'. *Canadian Journal of Chemical Engineering* **81**, 6, 1149-1158.

Hjertager, L.K., B.H Hjertager and T. Solberg (2002). 'CFD Modeling of Fast Chemical Reactions in Turbulent Liquid Flows'. *Computers and Chemical Engineering* **26**, 507-515.

Hjertager, L.K., B.H. Hjertager, and T. Solberg (2003). 'CFD modelling of turbulent mixing in a confined wake flow'. Proceedings AIChE Annual Meeting, San Francisco, CA., USA, Nov. 16-21.

Kolhapure, N. H. and R.O. Fox (1999). 'CFD analysis of micromixing effects on polymerization in tubular low-density polyethylene reactors'. *Chemical Engineering Science* **54**, 3233-3242.

Komori S., T. Kanzaki and Y. Murakami (1991). 'Simultanous measurements of instantaneous concentration of two reacting species in a turbulent flow with a rapid reaction'. *Phys Fluids* **3**, 4, 507-510.

Komori S., K. Nagata, T. Kanzaki and Y. Murakami. (1993). 'Measurement of Mass Flux in a Turbulent Liquid Flow with a chemical reaction'. *AIChE Journal* **39**, 10, 1611-1620.

Koochesfahani, M.M and P.E. Dimotakis (1986). 'Mixing and chemical reactions in a turbulent liquid mixing layer'. *J. Fluid Mech* **70**, 83-112.

Kruis F.E. and L. Falk (1996). 'Mixing and reaction in a tubular jet reactor: A comparison of experiments with a model based on a prescribed PDF'. *Chemical Engineering Science* **51**, 10, 2439-2448.

Lane, D. (2004). HyperStat Online. http://www.davidmlane.com/hyperstat/confidence_intervals.html

Law, A.W.-K.and H.Wang (2000). 'Measurement of mixing processes with combined digital particle image velocimetry and planar laser induced fluorescence'. *Exp. thermal and Fluid Science* **22**, 213-229.

Li, H.K and H.L. Toor (1986). 'Chemical indicators as mixing probes. A possible way to measure micromixing simply', *Ind. Engng. Chem. Fundam.* **25**, 719.

Liu, C.H. & C.H. Barkelew (1986). 'Numerical analysis of Jet-stirred reactors with turbulent flows and homogeneous reactions', *AIChE Journal* **32**, 11.

Lyn, D.A., S. Einav, W. Rodi and J.-H. Park (1995). 'A laser-Doppler velocimetry study of ensemble-averaged characteristics of the turbulent near wake of a square cylinder'. *J. Fluid Mech.* **304**, 285-319.

Magnussen, B.F. & Hjertager, B.H. (1976). On mathematical modelling of turbulent combustion with special emphasis on soot formation and combustion. 16th Int. Symposium on Combustion, 719, The Comb. Inst.

Marchisio, D.L., R.O. Fox, A.A. Barresi and G. Baldi (2000). A CFD approach to the description of turbulent precipitation in a semi-batch Taylor-Couette reactor. . In the 14th International Congress of Chemical and Process Engineering (27-30 August), Praha, Czech Republic.

Marchisio, D.L., R.O. Fox, A.A. Barresi and G. Baldi (2001). 'On the Comparison between Presumed and Full PDF Methods for Turbulent Precipitation'. *Ind. Eng. Chem. Res.* **40**, 5132-5139.

Meyer, K. E., O. Özcan and P.S. Larsen (2000). Point and planar LIF for velocity-concentration correlations in a jet in cross flow. 10th Int. Symp. on Application of Laser Techniques to Fluid Mech., 10-13 July, Lisbon, Portugal.

Neudeck, J.W. (1999). Multi-peak presumed pdf simulation of turbulent reacting Flows. M.Sc. Thesis, Kansas State University, Manhattan, Kansas.

Patankar (1980). *Numerical Heat Transfer and Fluid Flow*. Hemisphere Publishing Corporation.

Piirto, M., P. Saarenrinne, H. Eloranta and R. Karvinen (2003). 'Measuring turbulence energy with PIV in a backward-facing step flow'. *Exp Fluids* **35**, 219-236.

Piton, D., R.O Fox and B. Marcant (2000). 'Simulation of Fine Particle Formation by Precipitation using Computational Fluid Dynamics'. *The Canadian Journal of Chemical Engineering* **78**, 983-993.

Pohorecki, R. and J. Baldyga (1983). ' New Model of Micromixing in Chemical Reactors. 1. General Development and Application to a Tubular Reactor'. *Ind. Eng. Chem. Fund.* **22**, 392.

Pollei A., T. Borowski and M. Kraume (2000). 'Simulation of Turbulent Mixing in Precipitation Reactors'. In the 14th International Congress of Chemical and Process Engineering (27-30 August), Praha, Czech Republic.

Schmalzriedt, S., M. Jenne, K. Mauch and M.Reuss (2003). 'Integration of physiology and fluid dynamics'. *Advances in Biochemical Engineering, Biotechnology* **80**, 19-68.

Serag-El-Din, M.A.S. (1977). The numerical prediction of the flow and combustion processes in a three-dimensional can combustor. PhD-Thesis, University of London.

Tsai, K., R. Larkins, R. Spradling, S. Sen, C. Lipp, P. Gillis and L. Melton (1999). Development of a Simultanous PIV/Reactive PLIF system for Turbulent Liquid Flows. Presented at the annual AIChE meeting, Dallas.

Tsai, K., P.A. Gillis, S. Sen and R.O. Fox (2002). 'A Finite-Mode PDF Model for Turbulent Reacting Flows'. *Journal of Fluids Engineering* **124**, 102-107.

Ullum, U. (1999). Imaging Techniques for Planar Velocity and Concentration Measurements. PhD-thesis, Technical University of Denmark.

Valerio, S., M. Vanni, and A.A. Barresi (1994). 'Contribution of different turbulent scales to mixing and reaction between unpremixed reactants'. *Chemical Engineering Science* **49**, 24B, 5159-5174.

Versteeg, H.K. and W. Malalasekera (1996). An introduction to computational fluid dynamics, The finite volume method. Addison Wesley Longman Limited.

Walker, D.A. (1987). 'A fluorescence technique for measurement of concentration in mixing liquids'. *J. Phys E, Sci. Instrum* **20**, 217-224.

Zipp R.P. and G.K. Patterson (1998). 'Experimental measurements and simulation of mixing and chemical reaction in a stirred tank'. *The Canadian Journal of Ch. Eng.* **76**, 657-669.